TWR-16389A (Rev A)

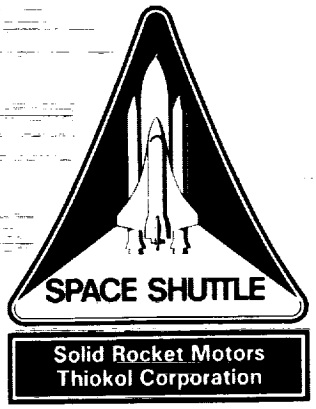

JPS Heater and Sensor Lightning Qualification Final Test Report

4 October 1989

Prepared for

National Aeronautics and Space Administration
George C. Marshall Space Flight Center
Marshall Space Flight Center, Alabama 35812

Contract No. NAS8-30490
DR No. 5-3
WBS No. HQ202-10-10
ECS No. SS1601

Thiokol CORPORATION
SPACE OPERATIONS

P.O. Box 707, Brigham City, UT 84302-0707 (801) 863-3511

Publications No. 90204

JPS Heater and Sensor Lightning Qualification
Final Test Report

Prepared by:

Matt Cook 4OCT89
Test Planning and Reporting

Approved by:

Requirements Manager

Design Engineer

Systems Integration Engineer

Program Manager

Reliability

Systems Safety

PC Sydeck 10-4-89
Data Management
ESC SS 1601

REVISION DESCRIPTION

REV LTR	DATE	DESCRIPTION
Basic	8-22-89	
A	10-4-89	Because the test data had not been fully evaluated by the original release date, the basic version of the final report was incomplete in addressing the requirements of a final test report. Rev A is a complete re-write of the basic version. Rev A includes a full evaluation of the test data, and all sections of the report have been addressed. The subcontractor's report is also included with Rev A, and is the primary source of information for the report.

ABSTRACT

Simulated lightning strike testing of the RSRM field joint protection system heater assembly was performed at Thiokol Corporation, Wendover Lightning Facility, from 27 May through 23 June 1989, with follow-on testing performed on 12 September 1989. Testing consisted of subjecting the lightning evaluation test article to simulated lightning strikes and evaluating the effects of heater cable transients on cables within the systems tunnel.

The maximum short circuit current coupled onto a United Space Boosters, Inc. operational flight cable within the systems tunnel, induced by transients from all cables external to the systems tunnel, was 92 amperes. The maximum open-circuit voltage coupled was 316 volts.

The maximum short circuit current coupled onto a United Space Boosters, Inc. operational flight cable within the systems tunnel, induced by heater power cable transients only, was 2.7 amperes; the maximum open-circuit voltage coupled was 39 volts. The maximum coupled levels onto a United Space Boosters, Inc. operational flight cable within the systems tunnel, with the heater power cable disconnected, were 2.7 amperes and 25.5 volts. All heater power cable induced coupling was due to simulated lightning discharges only, no heater operating power was applied during the test. The results showed that, for a worst-case lightning discharge, the heater power cable is responsible for a 3.9 decibel increase in voltage coupling to operational flight cables within the systems tunnel.

Testing also showed that current and voltage levels coupled onto cables within the systems tunnel are partially dependant on the relative locations of the cables within the systems tunnel.

Further lightning testing is recommended to better characterize redesigned solid rocket motor cable coupling effects as an aid in developing methods to reduce coupling levels, particularly with respect to cable placement within the systems tunnel. It is also recommended that critical operational flight cables within the systems tunnel be placed as far from the heater power cables as possible, to minimize coupling effects.

CONTENTS

FIGURES

ABBREVIATIONS AND ACRONYMS

A	ampere
CEI	contract end item
CW	continuous wave
dB	decibel
DFI	development flight instrumentation
dI/dt	current rise-rate
DWV	dielectric withstanding voltage
EMA	Electro Magnetic Applications, Inc.
EMI	electromagnetic interference
ET	external tank
GEI	ground equipment instrumentation
ICD	interface control document
IR	insulation resistance
JPS	joint protection system
JSC	Johnson Space Center
kA	kiloampere
NASA	National Aeronautics and Space Administration
nF	nanofarad
NSTS	National Space and Transportation System
OF	operational flight
RSRM	redesigned solid rocket motor
SRB	solid rocket booster
SRM	solid rocket motor
USBI	United Space Boosters, Inc.
V	volt

1

INTRODUCTION

This report documents the procedures, performance, and results obtained from the Joint Protection System (JPS) Heater and Sensor Lightning Qualification Test. Testing consisted of subjecting the solid rocket motor (SRM) lightning test article case, on which a complete JPS heater assembly was installed, to simulated lightning discharges and measuring the current and voltage levels coupled onto United Space Boosters, Inc. (USBI) operational flight (OF) cables within the systems tunnel. Testing complied with Johnson Space Center (JSC) 20007, National Aeronautic and Space Administration (NASA) Lightning Protection Verification Document, and National Space and Transportation System (NSTS) 07636 Revision D, NASA Lightning Protection Criteria Document.

The purpose of this test was to:

- Evaluate the lightning strike induced coupling effects that shielded heater power cables have on the USBI OF cables within the systems tunnel
- Collect data to verify present computer modeling so the test results can be extrapolated for application on flight configuration redesigned solid rocket motors (RSRM)

Electro Magnetic Applications, Inc. (EMA) was subcontracted by Thiokol Corporation to provide analytical support and assist in test site operation. The EMA test report, Lightning Testing and Modeling of Cable Coupling for the Space Shuttle Solid Rocket Booster's Systems Tunnel (Draft version), is the primary source of information for this report, and is included in the appendix. The EMA document is referenced throughout this report, and its review is recommended for a thorough description of the test. This test report highlights the primary results listed in the EMA document.

The lightning evaluation test article was located in the center of a nine meter high, 50 meter square 2.5 nF parallel plate peaking capacitor, and was subjected to discharges from four different current generators, each simulating a component of the worst-case, in-flight lightning strike waveform of NSTS 07636 (Figure 1). These current generators were: 1) Marx generator, which duplicates the rapid current rise of a lightning strike (high dI/dt); 2) high current generator, which duplicates the peak current of a lightning strike (high current levels); 3 and 4) intermediate and long duration continuing current generators, which duplicate the charge that exists in a lightning strike.

The test was performed from 27 May to 23 June 1989, with follow-on testing performed on 12 September 1989, at the Thiokol Lightning Strike Test Facility, Wendover, Utah. Testing was performed under CTP-0078, Qualification Test Plan for the JPS Heater and Sensor Lightning Test.

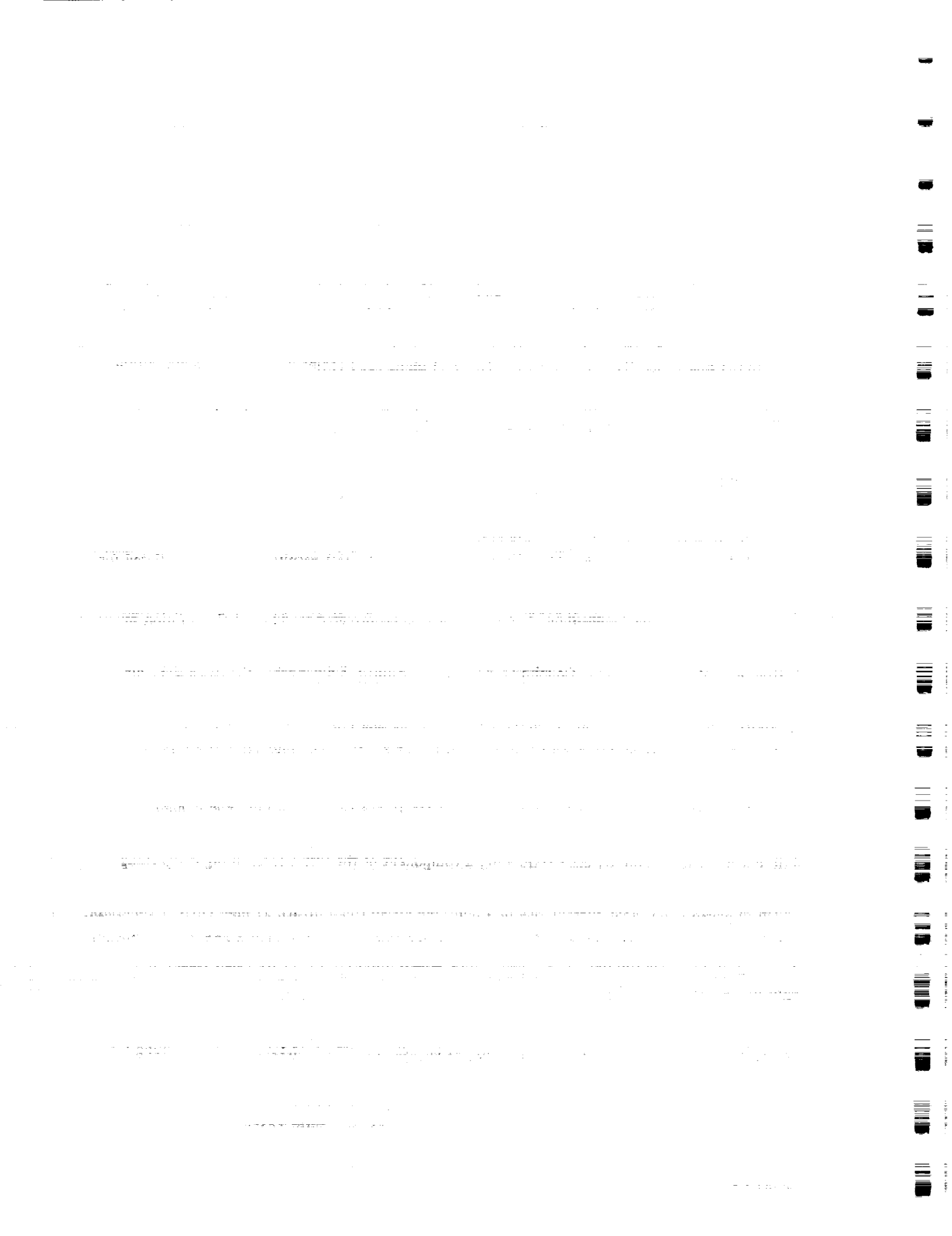

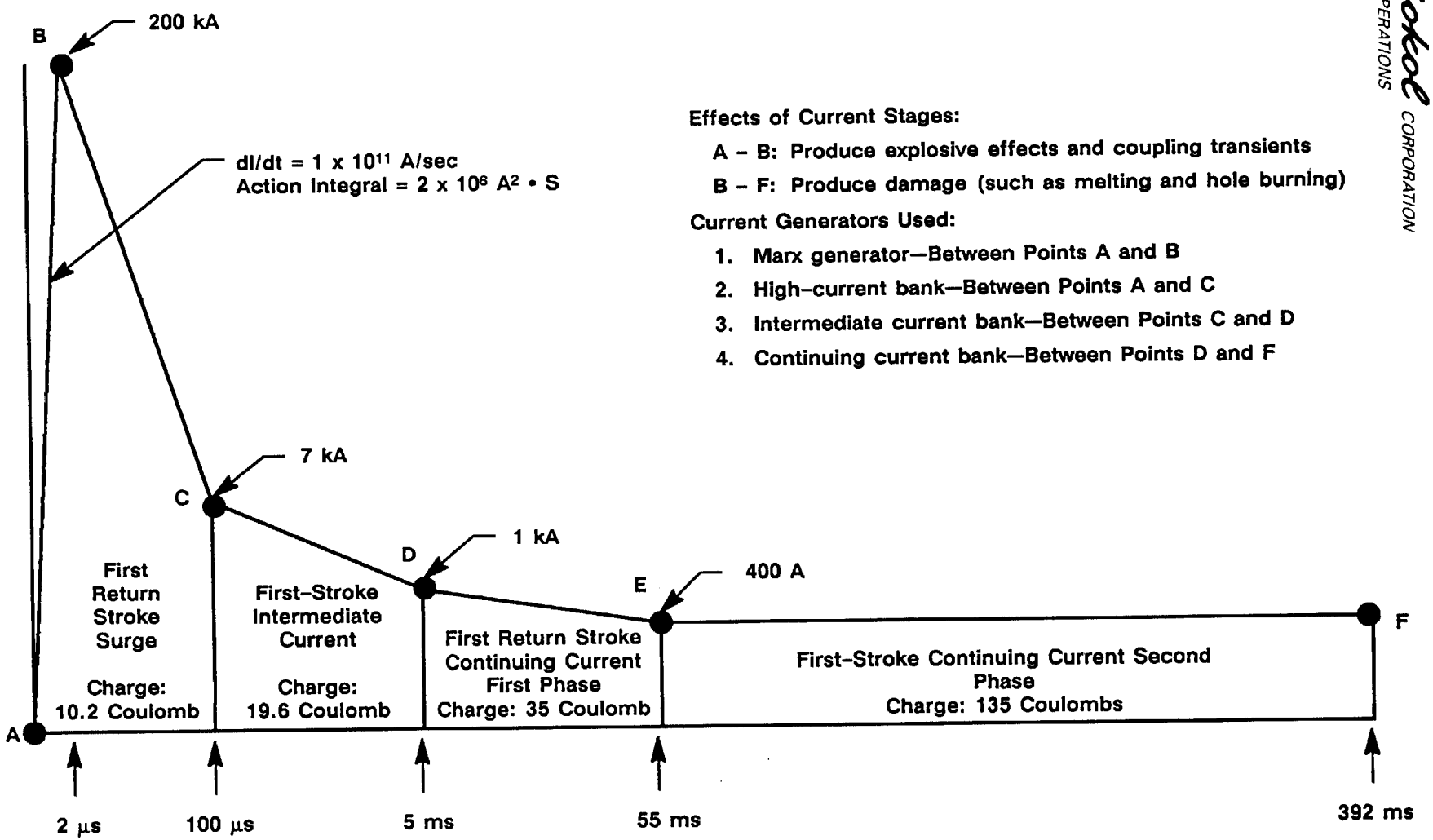

Figure 1. Worst-Case In-Flight Lightning Strike Waveform of NSTS 07636

A023334a

This test was part of an ongoing lightning strike test program to evaluate the complete RSRM and Space Transportation System under the affects of lightning strikes.

1.1 TEST ARTICLE DESCRIPTION

The lightning evaluation test article, already assembled at Wendover, consisted of a shortened SRM set on nonconducting chocks (Figures 2 and 3). Components of the test article included: a forward dome; SRM forward and aft segments; External Tank (ET) attach ring; aft dome; nozzle; nozzle jumper straps; instrumentation cables; and systems tunnel floor plates, covers and bond straps.

A complete field joint protection system (FJPS) (Figures 4 through 6), including a heater and sensor assembly, was assembled onto the lightning evaluation test article for this test in accordance with the specifications of Drawing 7U76546. The JPS heaters consist of primary and redundant chemically etched metal foil heater circuits that are encapsulated in a Kapton sheath. Each heater circuit is enclosed within a wire mesh shield for electromagnetic interference (EMI) protection. Heater operating power was provided through shielded lead wires which were welded to the termination pads of the etched foil heater elements (no operating power was applied during the test). Shielding for the heater power cables consisted of braided metallic "socks."

Systems tunnel cable switching boxes were assembled onto the test article at the ET attach ring and at each end of the systems tunnel. The switching boxes provided EMI shielding at the terminated ends of the cables to protect the instrumentation sensors and provide more accurate coupling measurements. With the switching boxes it was possible to measure, during a simulated lightning discharge, the coupling levels on any one of the 15 OF cables within the systems tunnel.

N108651-9

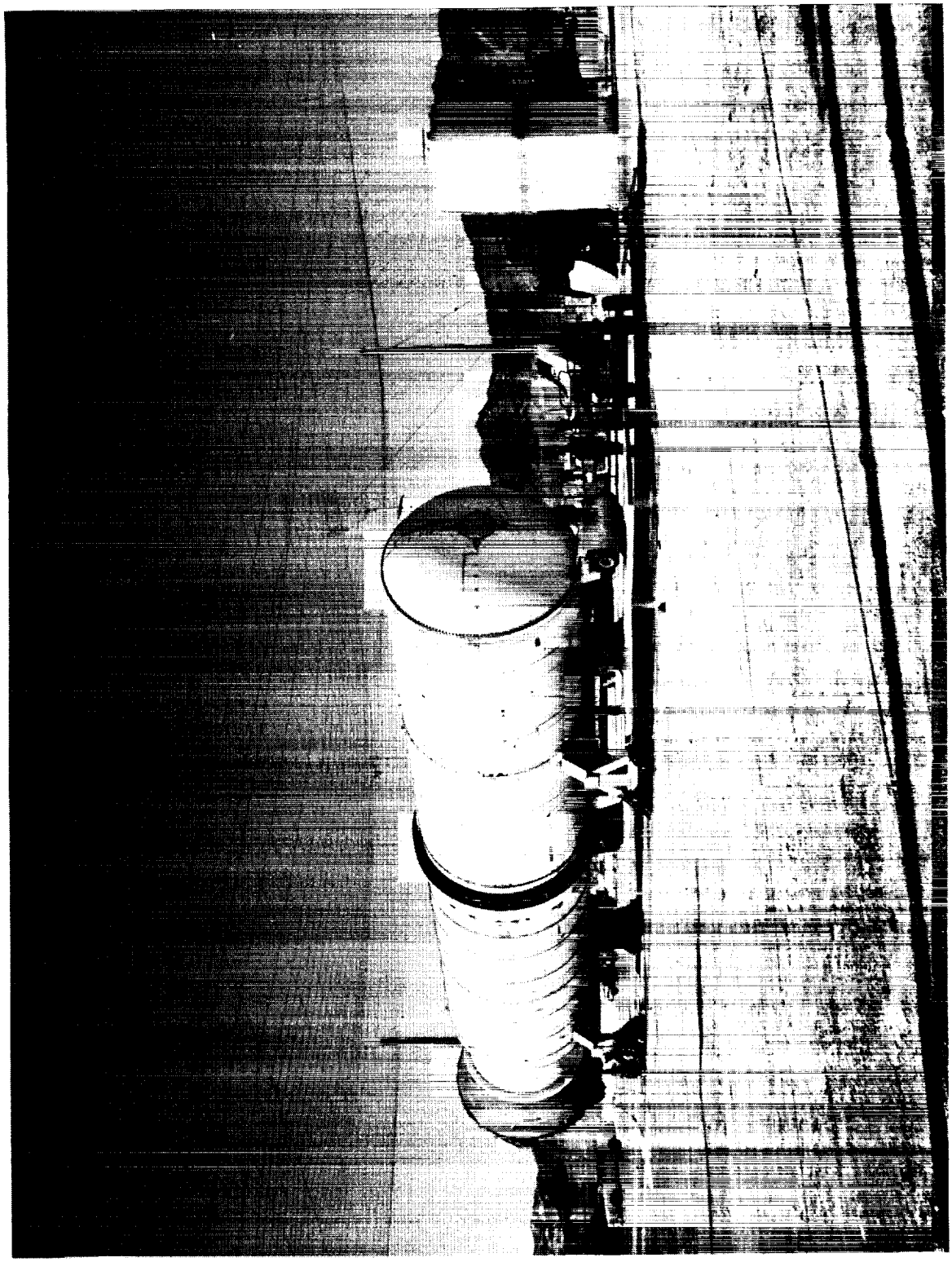

Figure 2. Assembled Test Article

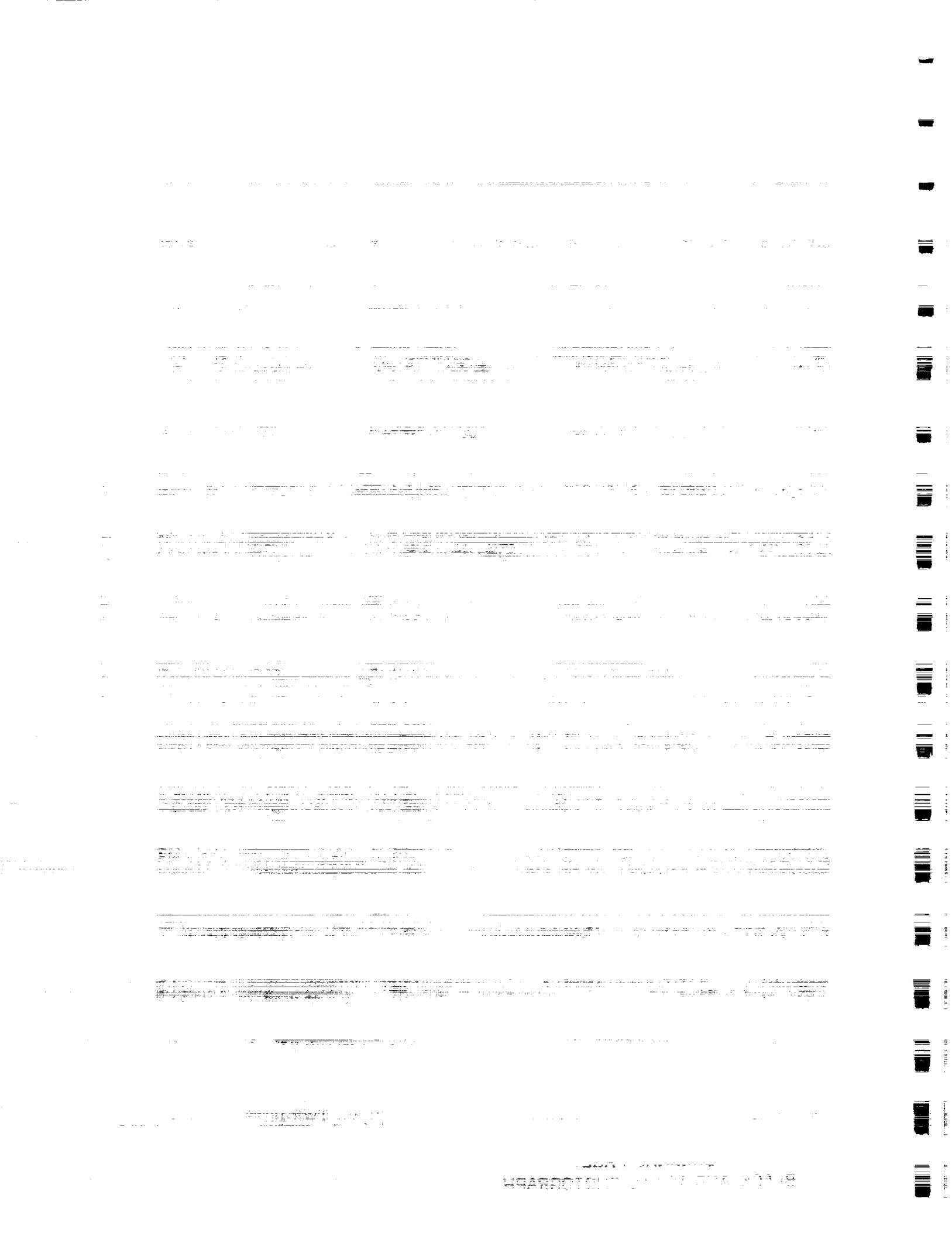

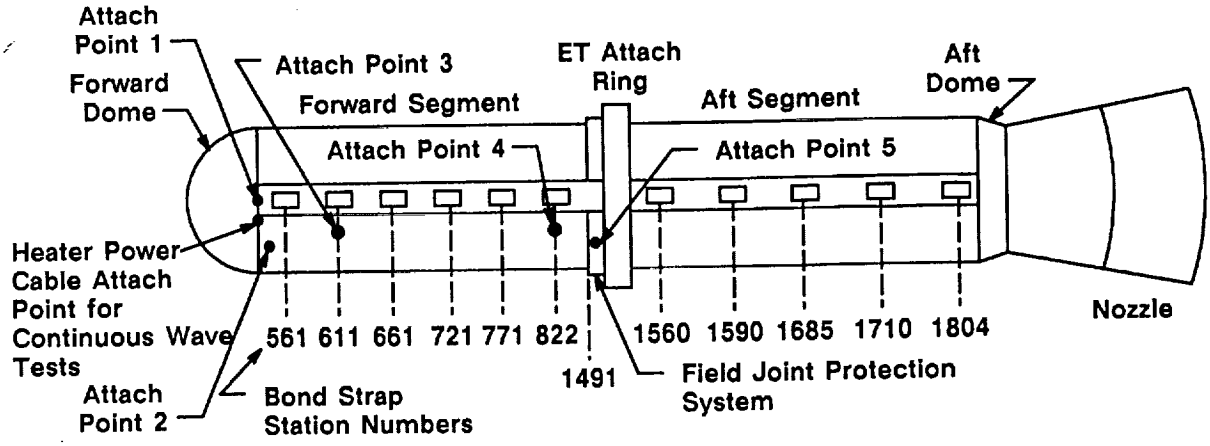

a) Top View

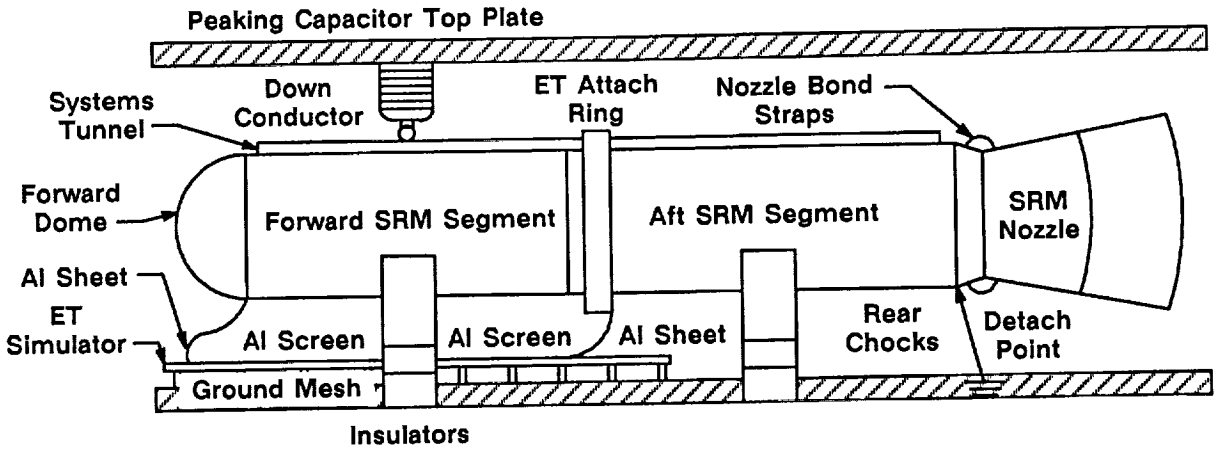

b) Side View

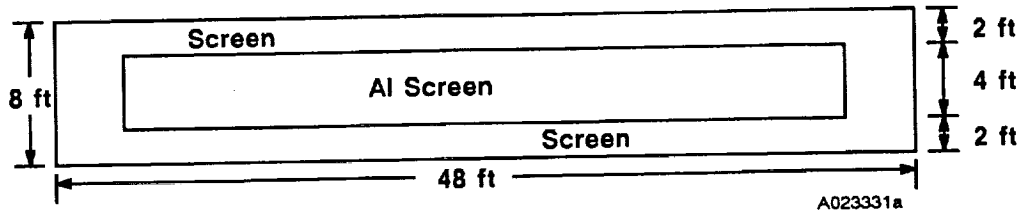

c) Top View of ET Simulator

Figure 3. Lightning Test Article Configuration

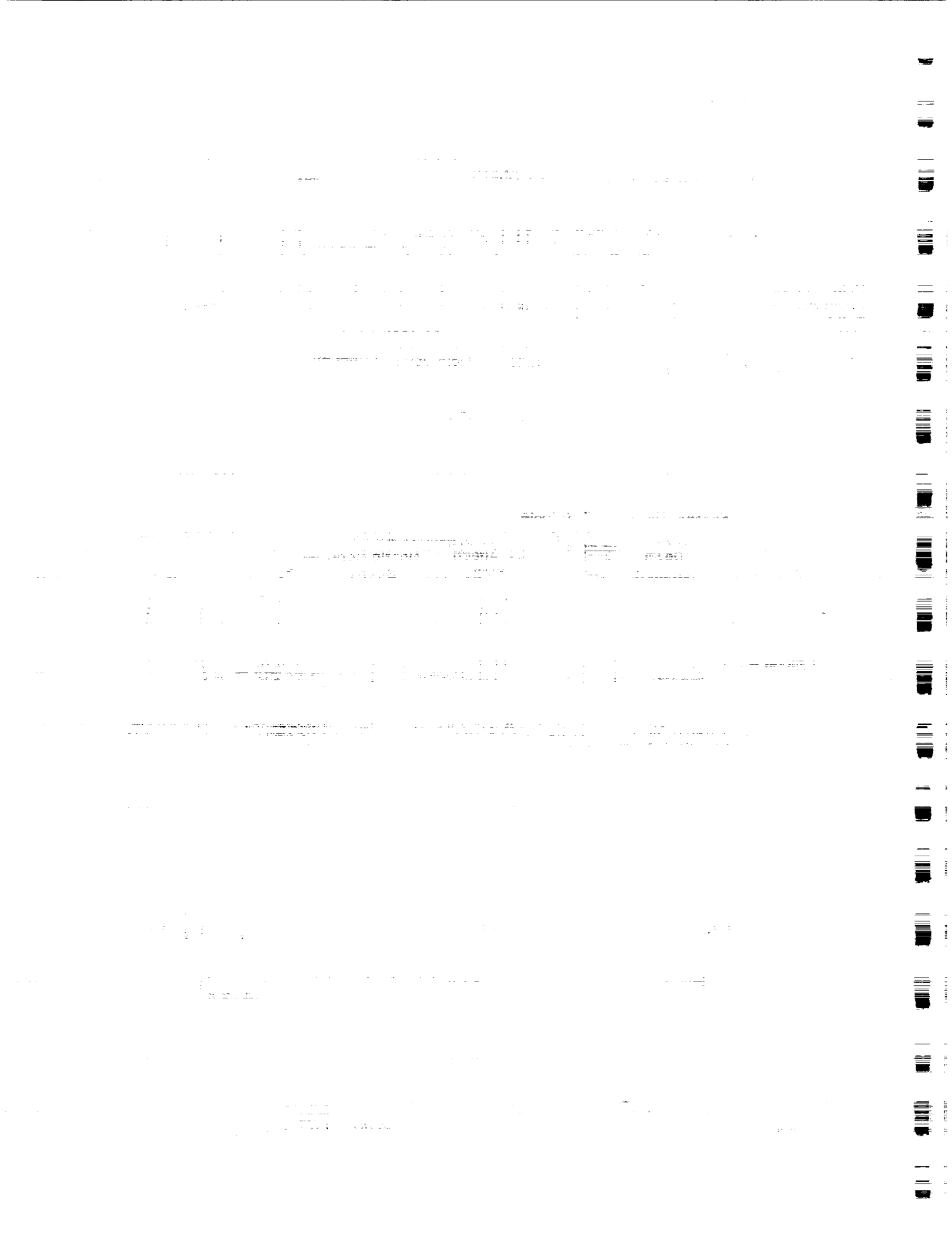

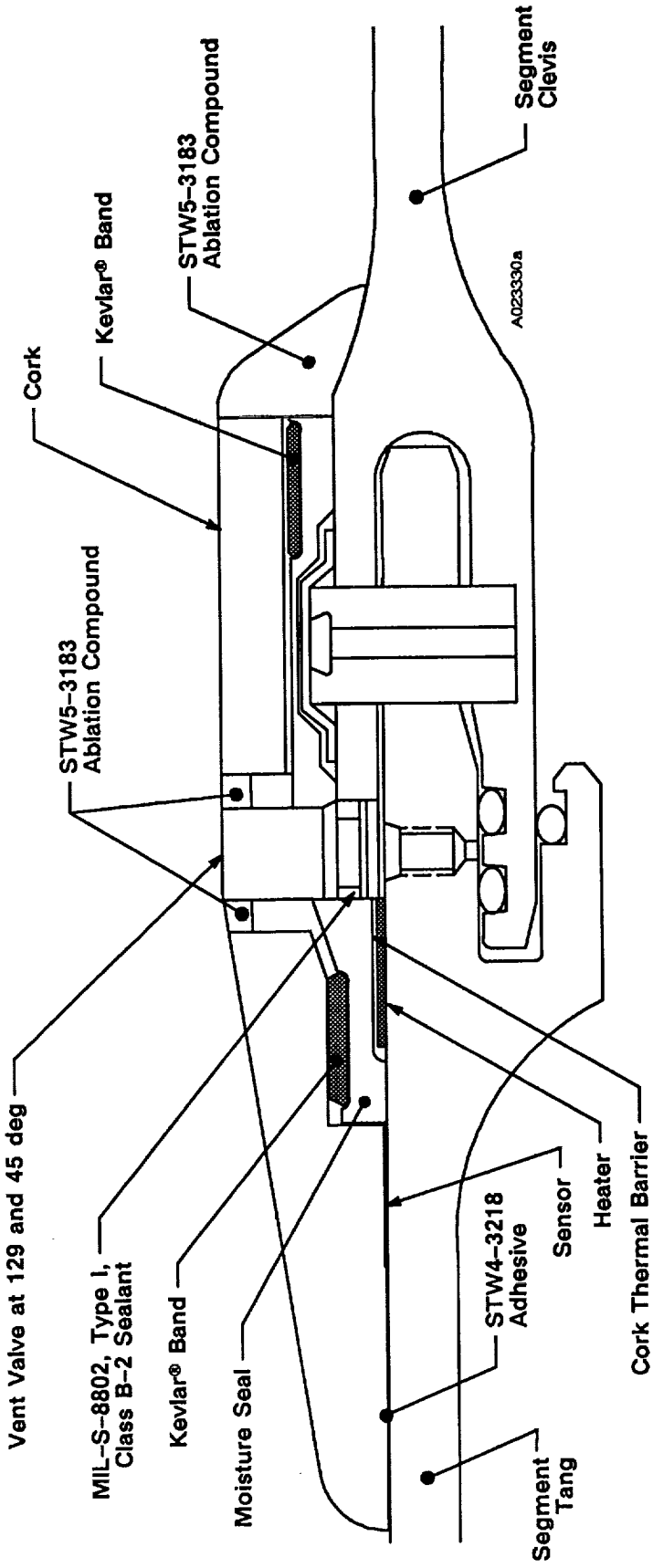

Figure 4. Field Joint Protection System

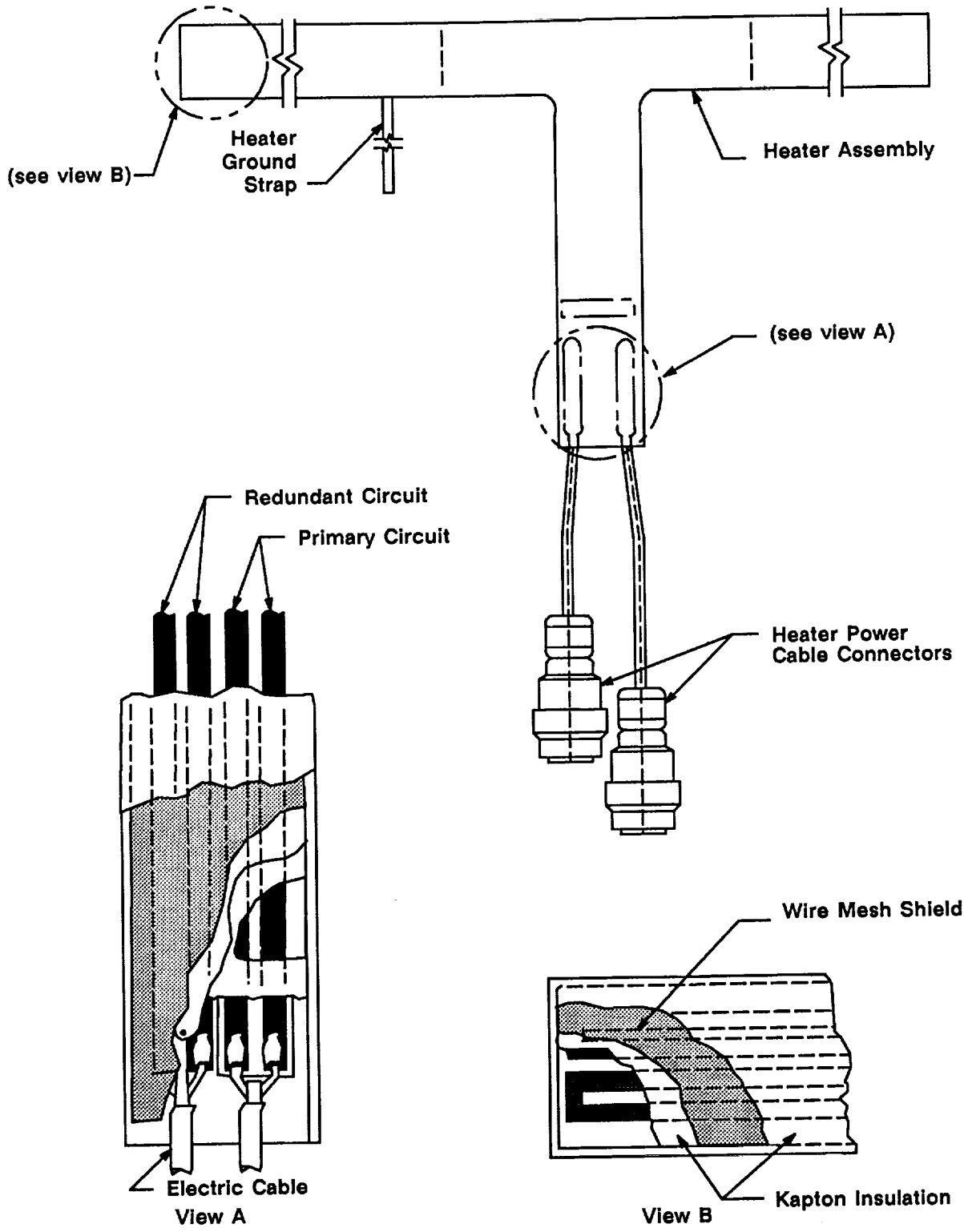

Figure 5. Heater Assembly

A023332a

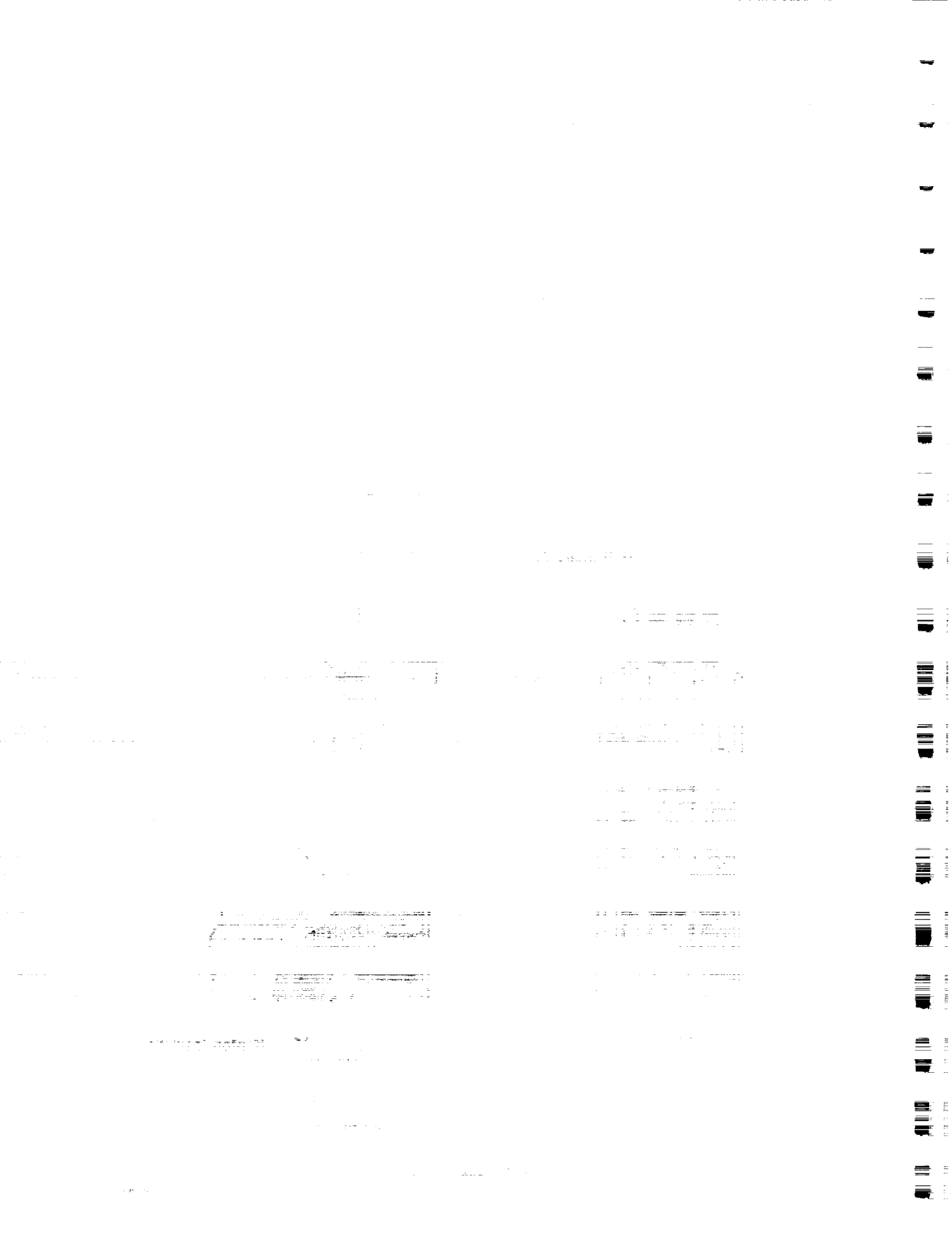

A023333a

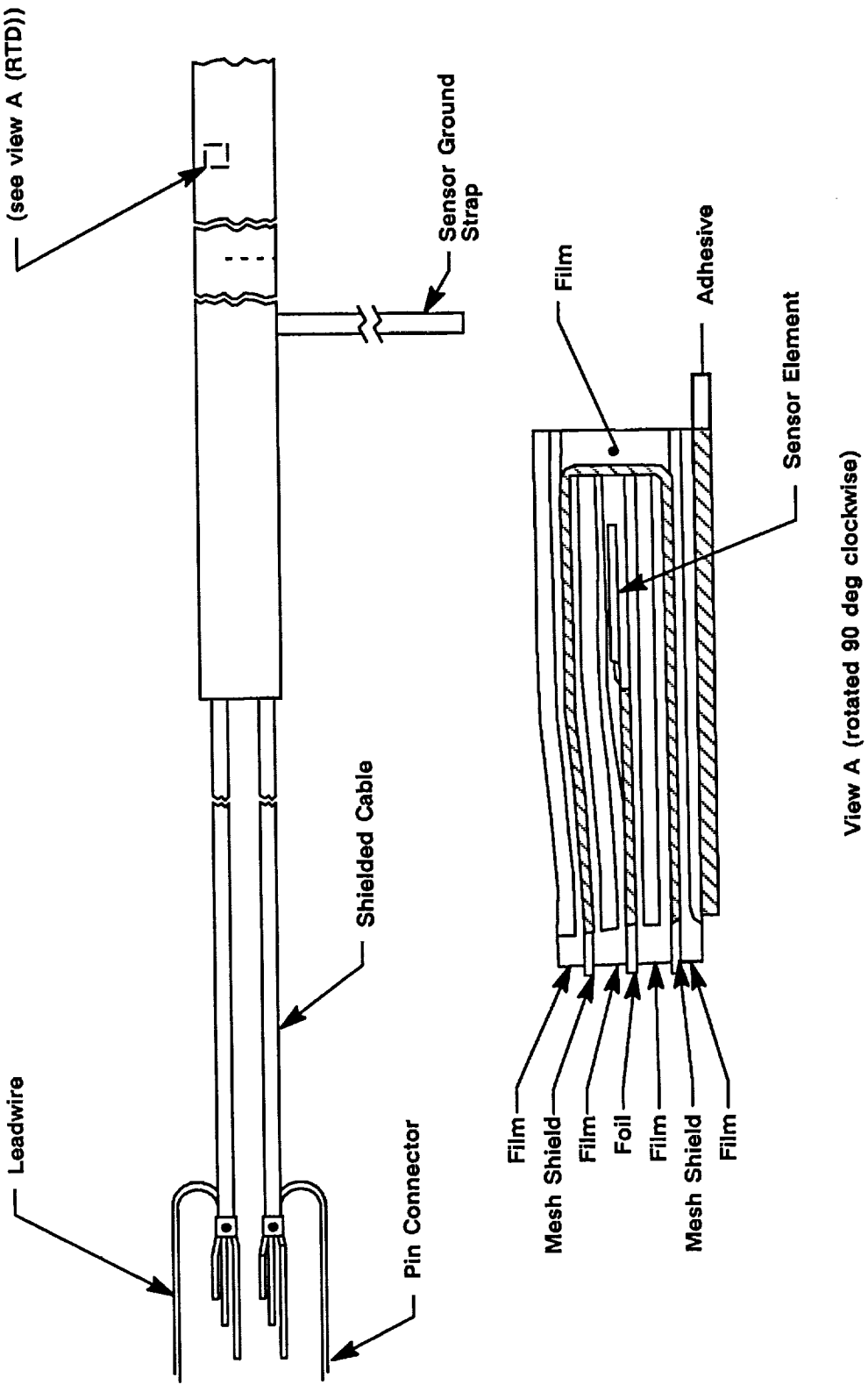

Figure 6. Heater Sensor Assembly

2

OBJECTIVE

The objective of Test Plan CTP-0078 was derived from the objectives in TWR-15723, Rev C, Redesign D&V Plan, to satisfy the requirement of contract end item (CEI) specification CPW1-3600 and design requirements document TWR-15583, Para 3.3.2.1:

A. Certify that the JPS heater and sensor with shielding meet the static electricity and lightning protection requirements of NSTS 07636, interface control document (ICD) 3-44005 and JSC 20007 after exposure to the indirect effects of lightning strikes.

3

EXECUTIVE SUMMARY

3.1 SUMMARY

This section contains an executive summary of the key results from test data evaluation and post-test inspection. Additional information and details can be found in Section 6, Results and Discussion.

3.1.1 Testing to Determine Coupling From All Cables External to the Systems Tunnel

Initial testing was performed to determine the coupling levels to cables within the systems tunnel, induced by all cables external to the systems tunnel. Simulated lightning discharges were injected to the systems tunnel cover, SRM case, an instrumentation cable, an instrumentation sensor, and the JPS heater.

The maximum short circuit current coupled onto a USBI OF cable within the systems tunnel was 92 amperes (A), and the maximum open-circuit voltage coupled was 316 volts (V). These levels were extrapolated to the worst-case (200 kA) condition of a lightning strike for unprotected flight hardware on the ground, according to NSTS-07636. The levels were also scaled to full-scale RSRM dimensions.

This testing also showed that current and voltage levels coupled onto cables within the systems tunnel are partially dependant on the relative locations of the cables within the systems tunnel.

3.1.2 Testing to Determine Coupling From the Heater Power Cable Only

Testing was then performed to determine the maximum coupling on cables within the systems tunnel, induced by heater power cable transients only. Simulated lightning discharges were injected to the case with the heater power cable connected per flight configuration, and with the heater power cable disconnected at its entrance to the systems tunnel. For the disconnected heater power cable configuration, a metallic shield was clamped over the cable entrance at the ET attach ring.

For the flight configuration discharges, the maximum short circuit current coupled onto a USBI OF cable was 2.7 A; the maximum open-circuit voltage coupled was 39 V. For discharges with the heater power cable disconnected, the maximum coupled levels onto a USBI OF cable were 2.7 A and 25.5 V. All heater power cable induced coupling was due to simulated lightning discharges only, no heater operating power was applied during the test. The coupled levels were scaled to the maximum current rise-rate (dI/dt) for a lightning discharge of $1x10^{11}$ A/sec, according to NSTS 07636. These results showed that, for a worst-case lightning discharge, the external

heater power cable is responsible for a 3.9 decibel (dB) increase in voltage coupling to OF cables within the systems tunnel.

3.2 CONCLUSION

The following listing is the conclusion as it relates specifically to the objective and corresponding CEI paragraphs. Additional information about the conclusion can be found in Section 6, Results and Discussion.

Objective	CEI Paragraph	Conclusions
A. Certify that the JPS heater and sensor with shielding meet the static electricity and lightning protection requirements of NSTS 07636, ICD 3-44005 and JSC 20007 after exposure to the indirect effects of lightning strikes. (ICD-3-44005 defines and controls the requirements for the electrical/instrumentation interfaces between the SRM and the solid rocket booster (SRB).)	3.3.5.5 Static Electricity and Lightning Protection. Static electricity and lightning protection shall comply with the requirements of NSTS 07636, ICD-3-44005, and shall be verified in accordance with JSC 20007.	The maximum current coupled onto a USBI OF cable within the systems tunnel was 2.7 A, and the maximum voltage coupled was 39 V. All heater power cable induced coupling was due to simulated lightning discharges only, no heater operating power was applied during the test. The coupled levels were scaled to the maximum current rise-rate (dI/dt) for a lightning discharge of $1x10^{11}$ A/sec, according to NSTS 07636. Test results showed that, for a worst-case lightning discharge, the external heater power cable is responsible for a 3.9 dB increase in voltage coupling to OF cables within the systems tunnel. These levels need to be compared with the threat levels of the terminal equipment that is attached to OF cables within the systems tunnel.

3.3 RECOMMENDATIONS

Recommendations, based on the results of this test, are as follows:

1. Perform further testing to better characterize RSRM cable coupling effects as an aid in developing methods to reduce coupling levels, particularly with respect to cable placement within the systems tunnel.
2. To minimize coupling effects, critical OF cables within the systems tunnel should be placed as far from the heater power cables as possible.

4

INSTRUMENTATION

Instrumentation used during this test is listed in TWR-18364, Lightning Tests Instrumentation Report. The instrumentation was installed under 7U76546. All test instruments were electrically zeroed and calibrated under MIL-STD-45662.

5

PHOTOGRAPHY

Still color photographs were taken of the test article, test setup, and post-test inspection. Copies of the photographs (Series 111300) are available from the Thiokol Photographic Services Department.

Color motion pictures of the test were taken with two documentary cameras to cover the overall test article and lightning transient injections.

6

RESULTS AND DISCUSSION

EMA was subcontracted by Thiokol Corporation to provide analytical support and assist in test site operation. The EMA test report, Lightning Testing and Modeling of Cable Coupling for the Space Shuttle Solid Rocket Booster's Systems Tunnel (Draft version), is the primary source of information for this report, and is included in the appendix. The EMA document is referenced throughout this section, and its review is recommended for a thorough description of the test. This section highlights the primary results listed in the EMA document.

This test was performed in conjunction with the developmental flight instrumentation (DFI) and ground equipment instrumentation (GEI) cable couple test, in an attempt to determine lightning coupling effects on the OF cables from all external RSRM cables. Results of the DFI and GEI lightning test are available in TWR-17796, Cable Coupling Lightning Transient Final Test Report.

6.1 ASSEMBLY

The lightning evaluation test article, already assembled at Wendover, consisted of a shortened SRM set on nonconducting chocks. A complete FJPS, including a heater and sensor assembly, was assembled onto the lightning evaluation test article in accordance with Drawing 7U76546. Assembly also consisted of systems tunnel components, including 15 OF cables, and cable switching boxes at the ET attach ring and at each end of the systems tunnel. (Sections 2.3, 2.4, and 4.2.2 of the appendix contain further information about cable type, location, and shielding.)

6.2 INITIAL TESTING

6.2.1 Dielectric Withstanding Voltage and Insulation Resistance Testing

Dielectric withstanding voltage (DWV) and insulation resistance (IR) tests were performed on all instrumentation/heater cables following installation and again following the first simulated lightning discharge. Measurements taken after the first discharge showed that injected voltage levels did not change any of the results of the previous DWV and IR tests.

DWV and IR measurements were then suspended until the conclusion of all testing because of the large amount of time involved in making these measurements, the lack of cable failures from the initial DWV and IR measurements, and the probability of damaging connectors during the measurement process.

At the conclusion of testing, DWV and IR measurements were repeated on the heater power cable. Results showed that no noticeable change occurred in the leads within the cable, except the

leads that were connected to the heater that was subjected to a direct arc attachment. The two leads that failed the electrical tests shorted to their grounds.

The DWV and IR tests showed that voltages induced in the cables within the systems tunnel by a lightning discharge did not exceed the dielectric strength of the insulation of the individual wires within the cables.

6.2.2 Low Level, Swept Continuous Wave Current Testing

Prior to specific testing to address the objectives of this test, low level, swept continuous wave (CW) currents were injected onto the test article to determine: 1) the location on the test article which, when subject to a lightning discharge, caused the highest coupling levels onto the OF cables, and 2) the OF cables that received the highest coupling levels. CW currents were injected (one at a time) onto the case by directly attached cables at five locations: Attach Point 1, the forward end of the systems tunnel cover; Attach Point 2, the forward end of the forward case segment; Attach Point 3, on an instrumentation cable at Station 611; Attach Point 4, on an instrumentation sensor at Station 822; and on the heater power cable at the forward end of the systems tunnel. The CW attachment locations are shown in Figure 3.

The CW tests measured the coupling levels on each of 15 OF cables within the systems tunnel. From these tests, it was determined that Attach Point 3 induced the highest level of coupling of the five locations tested. It was also determined that Cables 10 (USBI 10400-0017) and 14 (Thiokol 7U76857) received the highest overall levels of coupling (from discharges to all five attach points) of all 15 cables within the systems tunnel. (Sections 2.4 and 3.2 of the appendix contain additional information about CW testing.)

6.3 HIGH LEVEL TESTING AND RESULTS

6.3.1 Testing to Determine Coupling From All Cables External to the Systems Tunnel

Initially, testing was performed to determine the coupling levels to cables within the systems tunnel, induced by all cables external to the systems tunnel. Two discharges (one for open circuit voltage, one for closed circuit current) from each lightning current generator were applied at Attach Points 1 through 5 (Figure 3), and coupled levels were measured on the two worst-case OF cables (Cables 10 and 14, from the CW tests) within the systems tunnel.

Two discharges (one for short circuit current, one for open circuit voltage) from the Marx and the high current generators were then injected at Attach Point 3, and coupled levels were measured on each of the 15 OF cables within the systems tunnel. (Sections 2.4 and 3.2 of the appendix contain further information about the high level testing.)

The maximum short circuit current coupled onto an OF cable (Cable 8, USBI 10400-0017) within the systems tunnel was 92 A. The maximum open circuit voltage coupled onto an OF cable

(Cable 6, USBI 10400-0025) within the systems tunnel was 316 V. These levels were extrapolated to the worst-case (200 kA) condition of a lightning strike for unprotected flight hardware on the ground, according to NSTS-07636. The levels were also scaled to full-scale RSRM dimensions. (Section 3.2 of the appendix contains further information about high level test results.)

This testing also showed that current and voltage levels coupled onto cables within the systems tunnel are partially dependant on the relative locations of the cables within the systems tunnel. This is expected because geometrical configuration affects electric and magnetic fields within the systems tunnel.

6.3.2 Testing to Determine Coupling From the Heater Power Cable Only

Testing was then performed to determine the maximum coupling on cables within the systems tunnel, induced by heater power cable transients only. All heater power cable induced coupling was due to simulated lightning discharges only, no heater operating power was applied during the test. The heater power cable was positioned per flight configuration: external and parallel to the systems tunnel on the forward case, and inside the systems tunnel on the aft case. The heater power cable entered the systems tunnel at the ET attach ring. For this test, discharges were injected near the forward end of the forward segment (Attach Point 3, Figure 3). This attach point was chosen as a worst-case location because all current from a discharge would flow down the forward segment and induce the largest possible current pulse on the heater power cable. OF cable coupling effects were measured on Cable 10, because this cable was the closest to the heater power cable within the aft segment systems tunnel, and expected to be subjected to the most coupling.

Two discharges (one for short circuit current, one for open circuit voltage) from the Marx current generator were injected at Attach Point 3, with the heater power cable connected per flight configuration. Two similar discharges were also injected at Attach Point 3, with the heater power cable disconnected at the ET attach ring. For the disconnected heater power cable configuration, a metallic shield was clamped over the heater power cable entrance at the ET attach ring.

For the flight configuration discharges, the maximum short circuit current coupled onto Cable 10 was 2.7 A; the maximum open circuit voltage coupled onto Cable 10 was 39 V. For discharges with the heater power cable disconnected, the maximum coupled levels onto Cable 10 were 2.7 A and 25.5 V. The coupled levels were scaled to the maximum current rise-rate (dI/dt) for a lightning discharge of $1x10^{11}$ A/sec, according to NSTS 07636. The primary mode of coupling from heater power cable transients was inductive coupling. The results showed that, for a worst-case lightning discharge, the external heater power cable is responsible for a 3.9 dB increase in voltage coupling to OF cables within the systems tunnel.

7

APPLICABLE DOCUMENTS

Document No.	Title
CPW1-3600	Prime Equipment Contract End Item (CEI) Detail Specifications
CTP-0078	Qualification Test Plan for the JPS Heater and Sensor Lightning Test
EMA-89-R-62	EMA Lightning Testing and Modeling of Cable Coupling for the Space Shuttle Solid Rocket Booster's Systems Tunnel
ICD 3-44005	Solid Rocket Motor to Solid Rocket Booster Electrical and Instrumentation Subsystem
JSC 20007	Space Shuttle Lightning Protection Verification Document
NSTS 07636	Lightning Protection Criteria Document
TWR-15723	Redesign D&V Plan
TWR-17796	Cable Coupling Lightning Transient Qualification Final Test Report
TWR-18364	Lightning Test Instrumentation List

Military Standards	Title
MIL-STD-45662	Calibration System Requirements

Drawing No.	Title
7U76546	Lightning Test Article Assembly

APPENDIX A

LIGHTNING TESTING AND MODELING OF CABLE COUPLING FOR THE SPACE SHUTTLE SOLID ROCKET BOOSTER'S SYSTEMS TUNNEL (EMA report)

EMA-89-R-62
DRAFT

EMA ELECTRO MAGNETIC APPLICATIONS, INC.
P.O. Box 260263
Denver, CO 80226-2091
(303) 980-0070

LIGHTNING TESTING AND MODELING OF CABLE COUPLING FOR THE SPACE SHUTTLE SOLID ROCKET BOOSTER'S SYSTEMS TUNNEL

Prepared by:

J.C. Curry
M.A. Frisoni
R.A. Perala
G.J. Rigden
D.A. Steffen

Prepared for:

Thiokol Corporation
Wasatch Operations
Highway 93 West
Brigham City, Utah 84302
Contract # 8MD011A1

August 1989

LIST OF FIGURES

LIST OF FIGURES (Cont'd.)

LIST OF FIGURES (Cont'd.)

LIST OF FIGURES (Cont'd.)

LIST OF TABLES

LIST OF TABLES (Cont'd.)

CHAPTER 2
TEST DESCRIPTION

2.1 Wendover Site

Between May 8 through May 14, and May 26 through June 21, 1989, EMA helped perform tests on the Space Shuttle Solid Rocket Booster (SRB) at the Thiokol Lightning Test Facility at Wendover, Utah, as the different SRB test configurations became available. The test site, located at the end of an old aircraft runway on the salt flats, as viewed from above is shown in Figure 2.1. The principal components of the test site are the four capacitor banks and the 9 meter high, 50 meter square 2.5 nF parallel plate peaking capacitor. Details of the four capacitor banks are as follows:

1. Marx Generator - 16 stage, 1.6 megavolt Marx generator.

2. High Current Bank. - 2 stage, 120 kilovolt Marx generator.

3. Intermediate Current Bank - 9 kilovolt, 3.2 mF capacitor bank.

4. Continuing Current Bank - 900 volt, 0.3 F capacitor bank.

Also shown is the doubly-shielded screen room on the back of a trailer which shields electromagnetically the computer and fiber optic receivers and digitizers for data acquisition, and the control shed housing the high-voltage controls for the capacitor banks.

2.2 Test Current Waveforms

Figure 2.2 shows the NASA ground lightning specification (JSC-07636, Revision D), with the various parts of the waveform specification satisfied by the different capacitor banks as follows:

1. Marx Generator - Between points A and B. Provides high dI/dt at the leading edge of the lightning threat waveform.

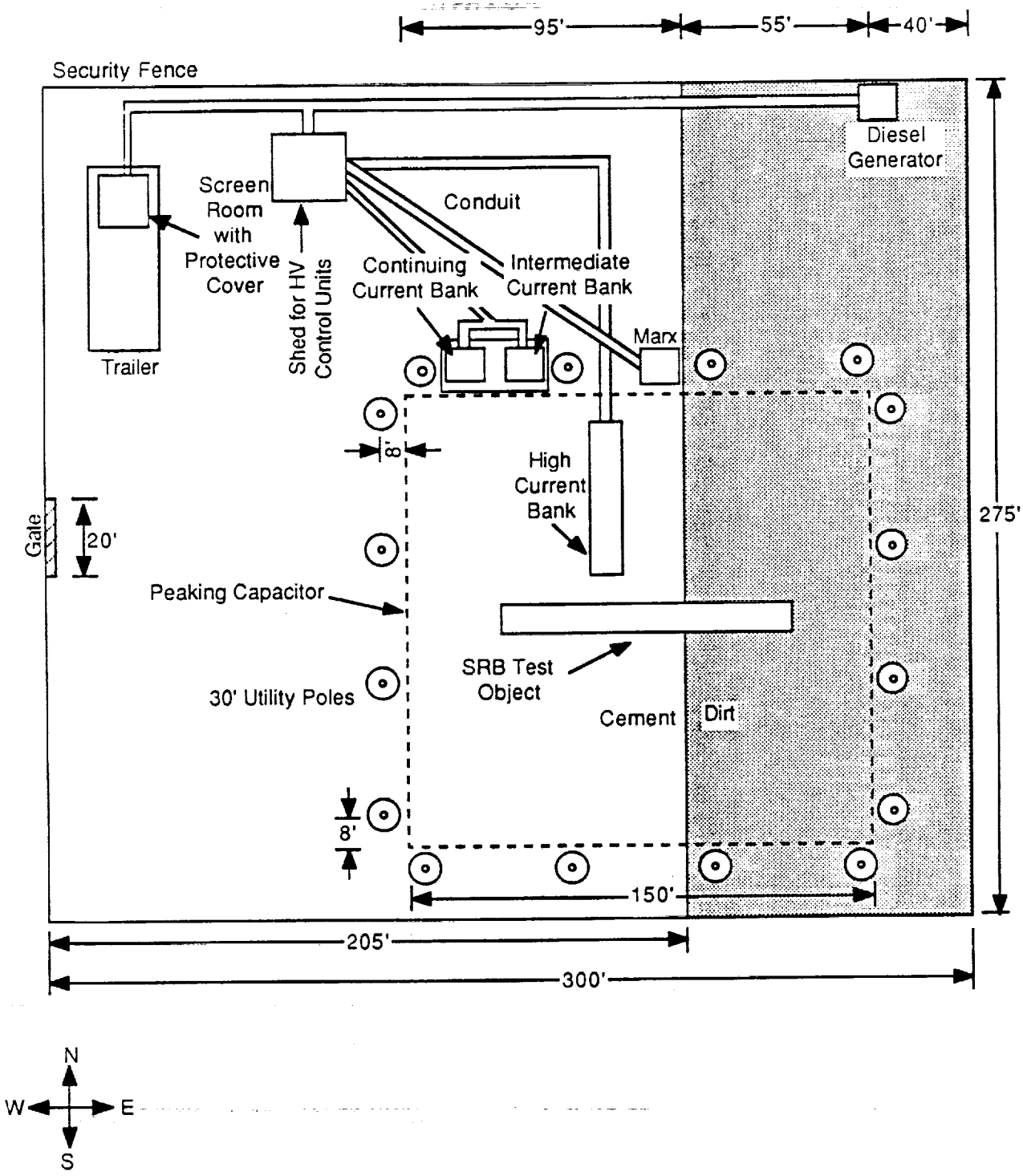

Figure 2.1 SRM Test Site - Wendover, Utah

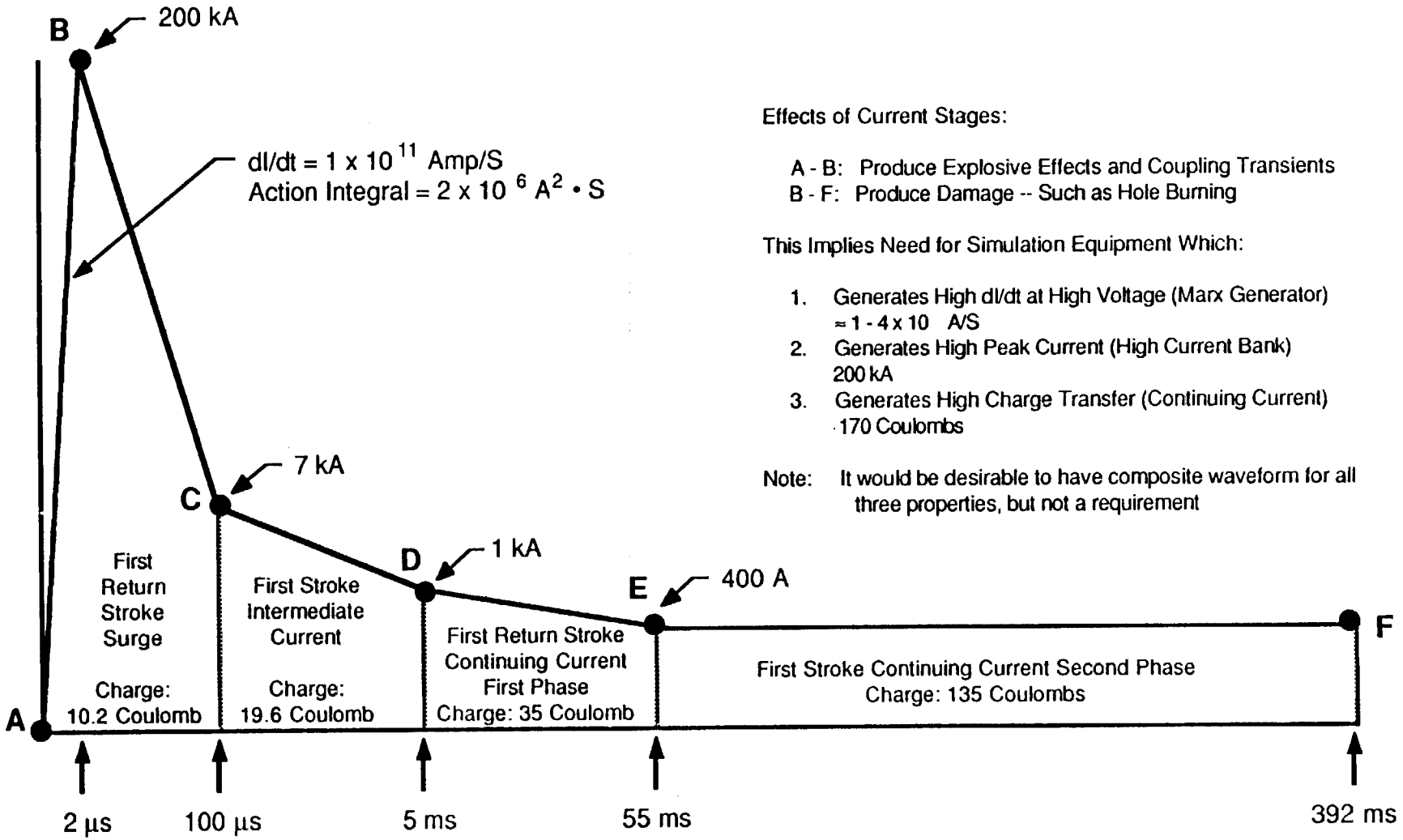

Effects of Current Stages:

A - B: Produce Explosive Effects and Coupling Transients
B - F: Produce Damage -- Such as Hole Burning

This Implies Need for Simulation Equipment Which:

1. Generates High dI/dt at High Voltage (Marx Generator) ≈ 1 - 4 x 10 A/S
2. Generates High Peak Current (High Current Bank) 200 kA
3. Generates High Charge Transfer (Continuing Current) 170 Coulombs

Note: It would be desirable to have composite waveform for all three properties, but not a requirement

Figure 2.2 Ground Lightning Specification - Full Threat Parameters (JSC-07636 Revision D) (Not to Scale)

2. High Current Bank - Between points A and C. Provides peak current and action integral early in the lightning threat waveform.

3. Intermediate Current Bank - Between points C and D.

4. Continuing Current Bank - Between points D and F. Provides most of the total electrical charge requirements.

The Intermediate and Continuing Current Banks simulate different phases of the trailing end of the natural lightning waveform, which is low current but long-lasting and causes melting and burning.

2.3 Test Article

The test article consisted of a shortened version of the SRB. Figure 2.3 shows the test article, consisting of a forward dome, forward SRM (Solid Rocket Motor) section, aft SRM section, SRM nozzle, nozzle bond straps, system tunnel with system tunnel bond straps and ET (External Tank) attach ring. This shortened (and empty, no propellant) SRB was placed horizontally on non-conductive chocks centered within the peaking capacitor. A conducting loop connected between the ET attach ring and forward sections and situated on the bottom of the SRB was utilized to simulate the in-flight attachment to the ET. Figure 2.3 also shows the station numbers which serve as longitudinal coordinates along the booster, and Figure 2.4 shows the angular coordinates as seen looking forward up the nozzle.

Located both inside and outside the systems tunnel are various OFI (Operational Flight Instrumentation), DFI (Developmental Flight Instrumentation) and heater cables. Figure 2.5 gives a cable diagram showing the 15 cables on which measurements were taken, their entry and exit points, and the appropriate USBI or Thiokol numbers and the cable numbering 1-15 that was used during the testing. Table 2.1 provides much the same numbering information as Figure 2.5, but also gives details on the shielding. Thiokol cables had no overall shields inside the system tunnel, but did have EMI shields inside the tunnel and were shielded outside the system tunnel. As some of the Thiokol cables entered the system tunnel (see Table 2.1), the outside shield was terminated at a 360 degree "sock" shield that was

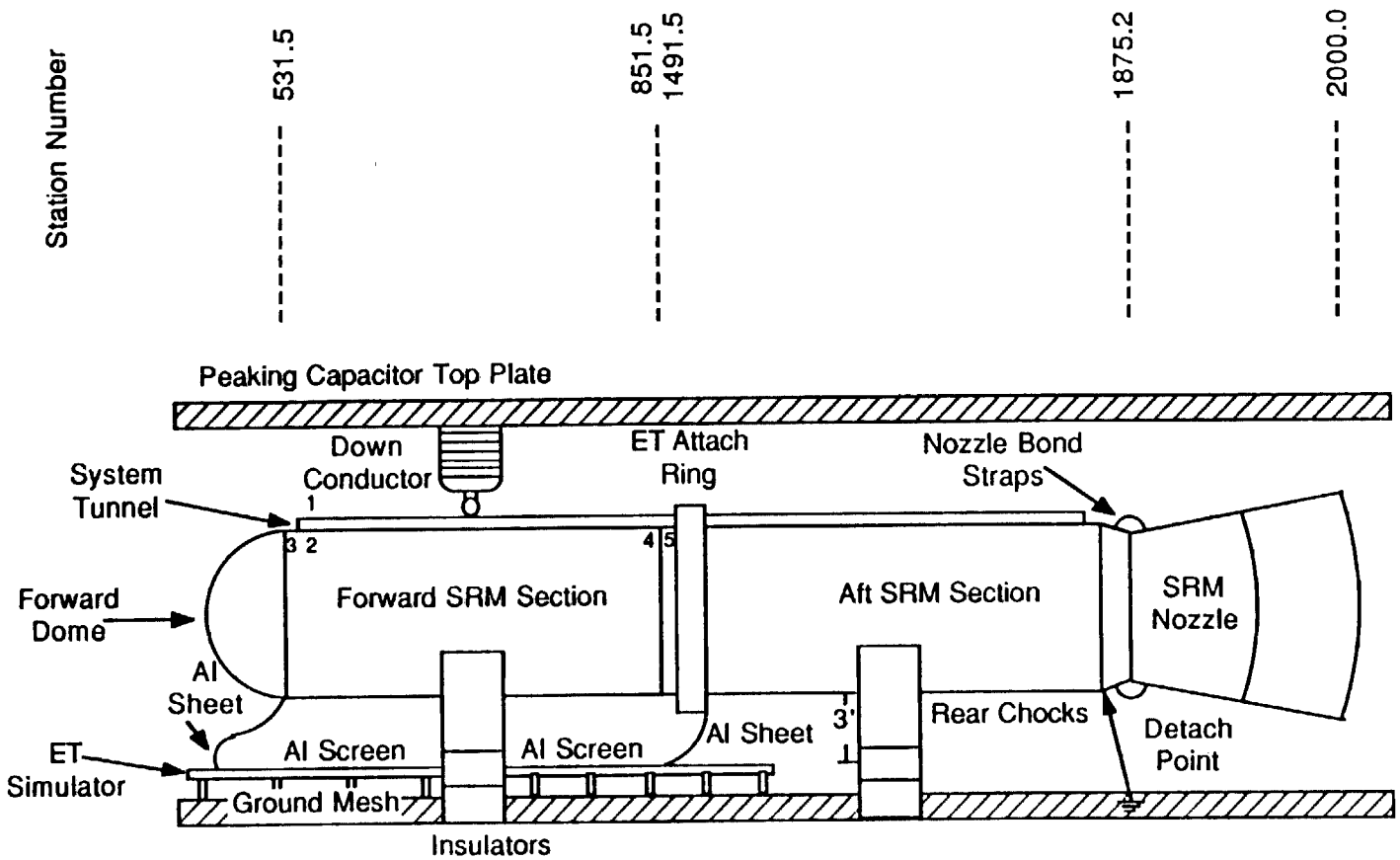

Figure 2.3 SRB Test Object and Peaking Capacitor

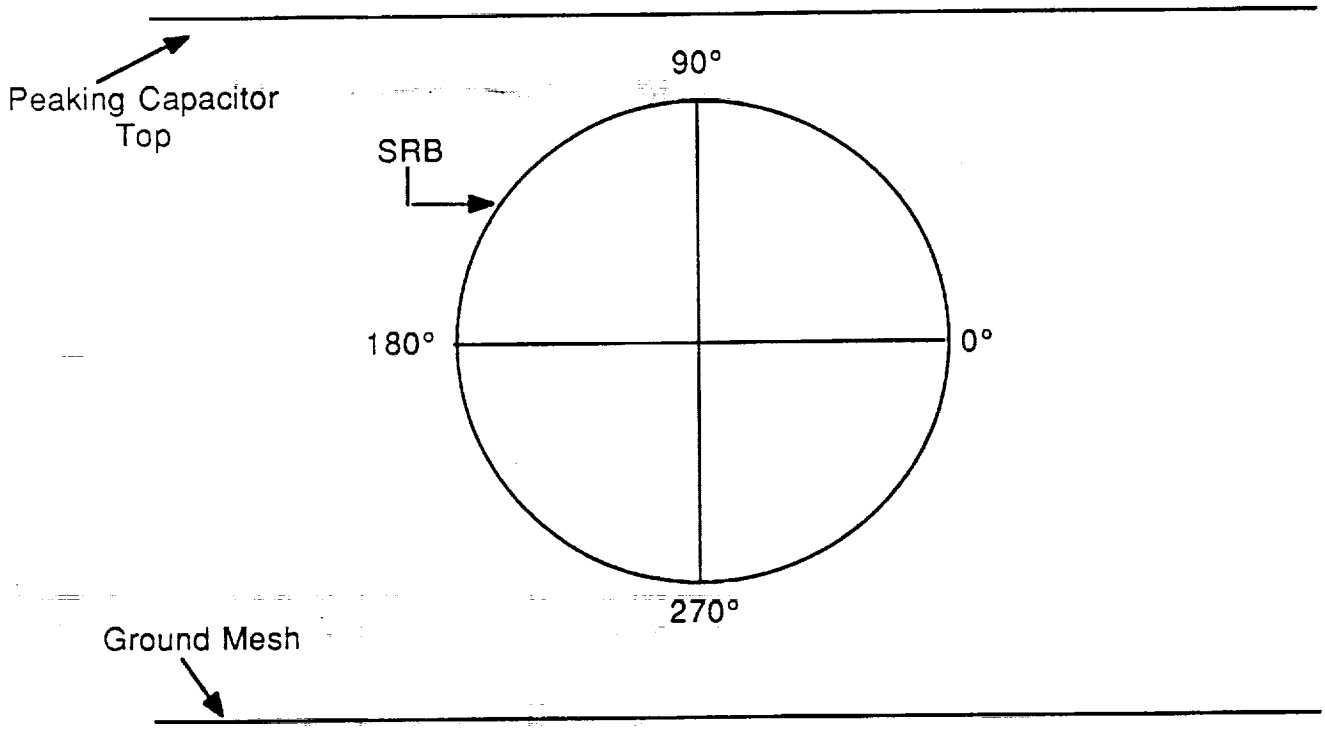

Figure 2.4 Angular Coordinates as Seen Looking Forward up the Nozzle

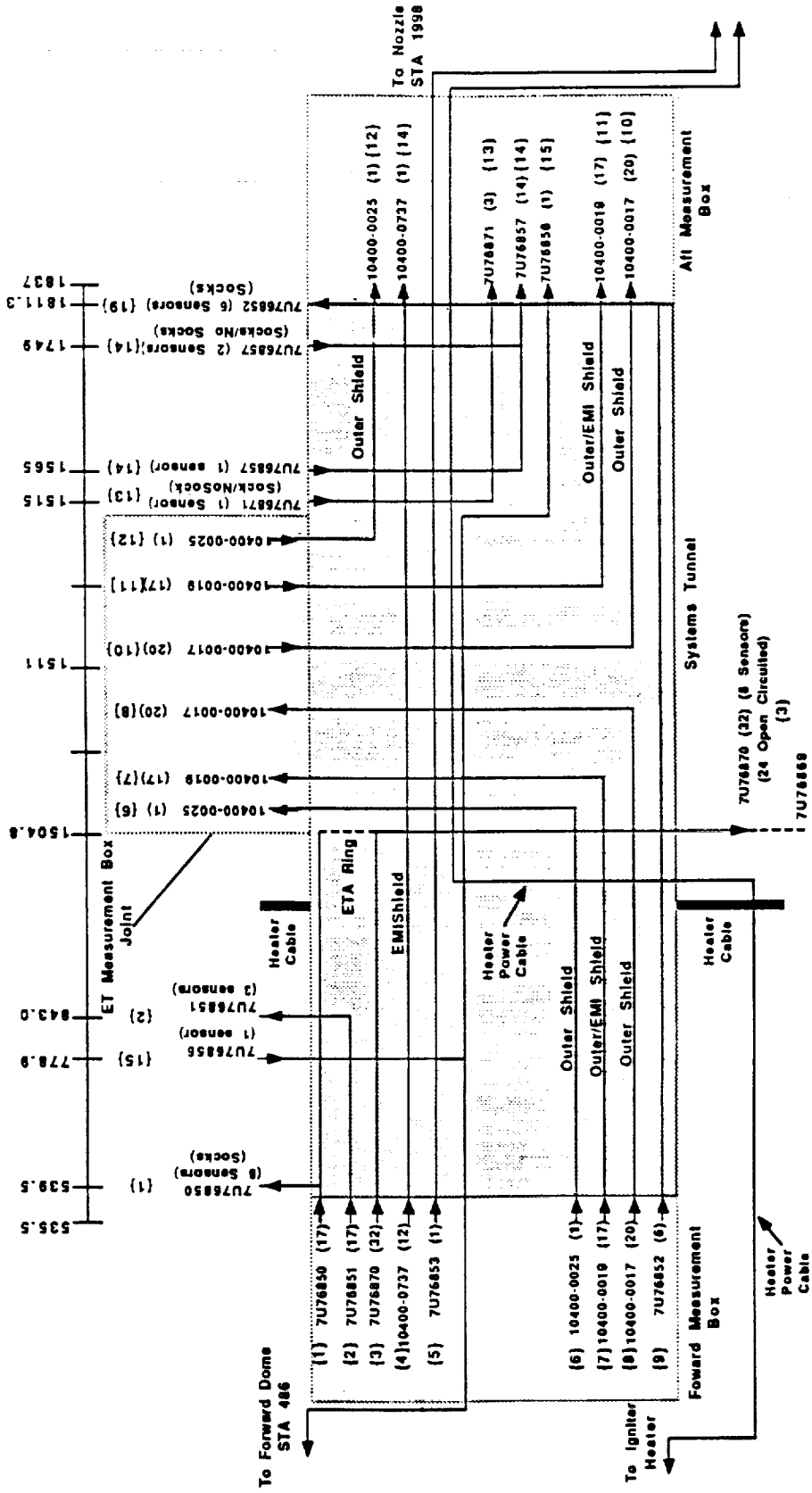

Figure 2.5 Cable Diagram Sketch/Systems Tunnel. Numbers Inside Curly Style Brackets {} are Test Cable Numbers (1-15). Numbers Inside Ordinary Style Parenthesis () are the Number of Twisted Wire Groupings for that Cable

intended to ground the outside shield at the system tunnel. However, during installation it was found that it was not possible to connect the bonding straps inside the systems tunnel to ground the sock shields, so the sock shields were all floating. All of the USBI cables have overall shields (except cable 4), but some have EMI shields for the individual wires or bundles as indicated in Table 2.1.

Incorrect, all 'socks' were bonded to the case and systems tunnel entrance with STW4-2874 electrically conductive adhesive (Eccobond Solder 56C).

Table 2.1

Cable Numbering and Shielding Information

Thiokol Cables:

Test Number	Thiokol Number	"Sock" Shield
1	7U76850	Yes
2	7U76851	No
3	7U76870	No
5	7U76853	No
9	7U76852	Yes
13	7U76871	No
14	7U76857	Yes
15	7U76856	No

USBI Cables

Test Number	USBI Number	EMI Shield
4	10400-0737	Yes
6	10400-0025	No
7	10400-0019	Yes
8	10400-0017	No
10	10400-0017	No
11	10400-0019	Yes
12	10400-0025	No

2.4 Measurement Details

The bulk of the measurements made were short circuit currents (I_{sc}) and open circuit voltages (V_{oc}) induced on the 15 cables when the current from one of the four capacitor banks was injected at one of the five attachment points shown in Table 2.2, and indicated by its number in Figure 2.3. Note that attach points 1, 2 and 3 are closely clustered at the top forward part of the booster, while 4 and 5 are down by the ET attach ring near the middle of the shortened SRB. Also, attach point 2 is DFI Thiokol cable 7U76850 with test numbering 1. There was one detachment point at the bottom rear of the aft SRM section before the nozzle bond straps, as is indicated in Figure 2.3.

Table 2.2
Attachment Point List

Attach Point	Station Number	Angular Position	Type
1	545	90	System Tunnel
2	545	100	DFI Cable (Test Cable 1)
3	539	100	SRM Case
4	1491	100	Heater Cable
5	1502	100	DFI Sensor

To facilitate these cable measurements, three special aluminum boxes were constructed to sit at the aft and forward ends of the systems tunnel, and at the ET attach ring at the middle of the booster. Figure 2.6 shows in generic form the configuration inside the boxes. Entering into the box from the system tunnel or the ET attach ring is a cable (one of several), which has a backshell shield on entry to the box and is connected to any overall shields that the cable may have. Any EMI shields that the USBI cables may have is left open on the measurement end with the overall and EMI shields grounded on the far, non-measurement end. Thiokol cable shields were not grounded on the far, sensor end. All of the signal wires for each cable are then tied together at a ring, with one wire then going to a pole of a multipole rotary switch.

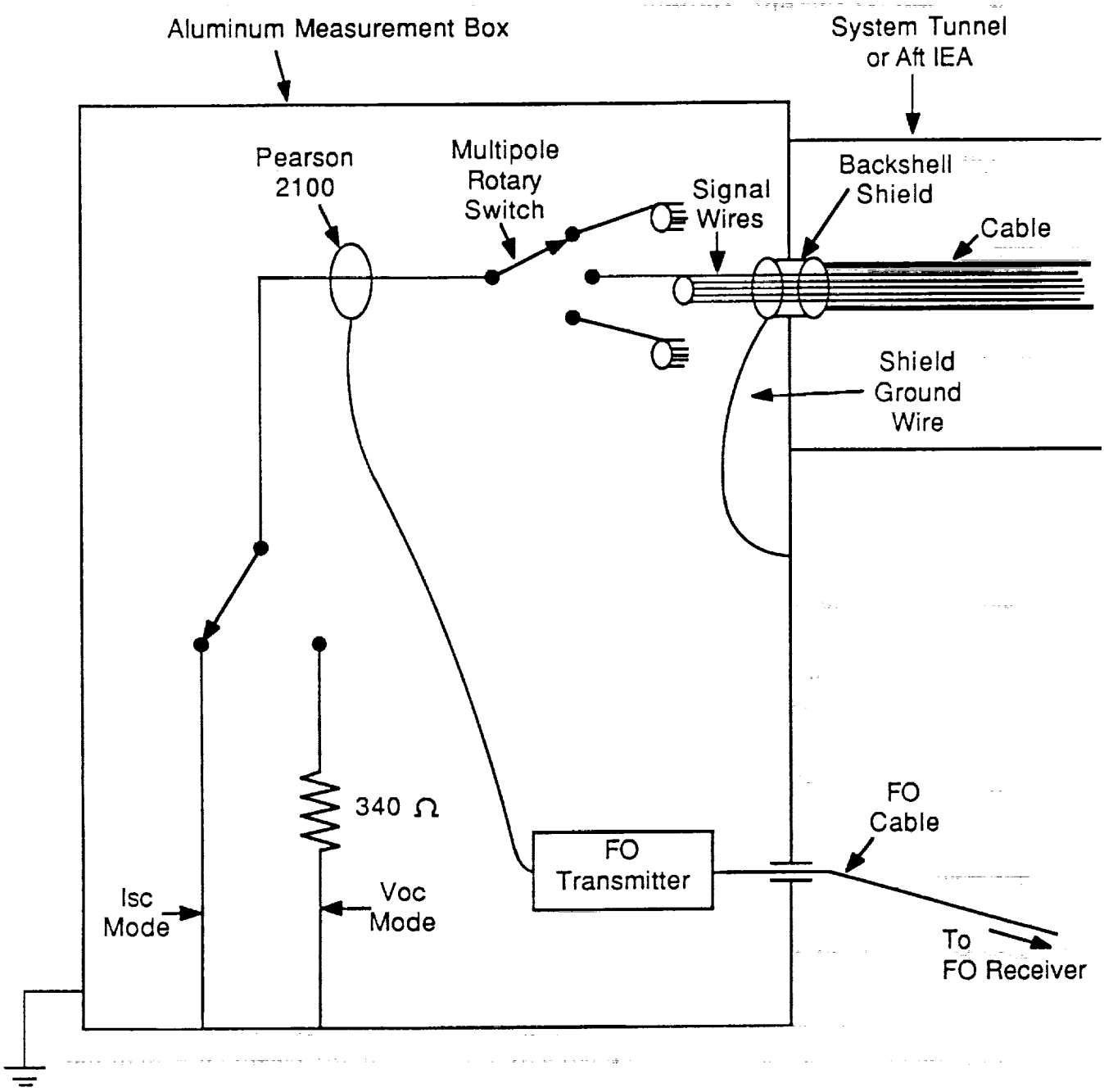

Figure 2.6 Generic Circuit Schematic Inside Measurement Boxes

Thus a cable could be selected by turning this switch. On the other side of the multipole switch is a Pearson 2100 current probe which outputs a voltage proportional (0.5 volts/amp) to the current on the wire through its loop. This voltage is conducted by cable to the Nanofast fiber optic transmitter inside the box and then outside the box by fiber optic cable. There is then one last switch past the Pearson probe that allows one to select between a direct connection to ground for a short circuit current measurement, or to ground through a 340 ohm resistor for a measurement of the open circuit voltage (once the current that the Pearson probe senses has been multiplied by 340 ohms). All USBI cables terminated at both ends at boxes, so that it was possible to switch the non-measurement end's rotary switch to the same cable and then direct short to ground for the second switch. However, the non-measurement ends of the Thiokol cables terminated outside the system tunnel with the signal wires attached to resistors which simulated the sensors to which the signal wires are usually attached. Appendix A gives the Thiokol circuit schematics for the three boxes.

Before performing high level tests on the SRB it was judged appropriate to perform swept CW (continuous wave) measurements on all of the cables. This technique allows one to sweep through a band of frequencies with a known injection current, against which the response is compared. A Hewlett-Packard 3577A network analyzer was used for this along with an RF amplifier to boost the analyzer's output current, as is shown in Figure 2.7. The network analyzer's output current was run via RG214 cable from the shield room out to the RF power amplifier, and then to one of the five attachment points. The injection current was monitored at the attachment point by a Pearson probe and relayed to the network analyzer by the fiber optic system.

During a test, the rotary switch was set for the desired cable and the second switch for short circuit current or open circuit voltage. The response was then monitored by a separate Pearson probe and fed back into the network analyzer by another fiber optic system, where the injection and response signals were compared and plotted. This procedure was followed for all fifteen cables and five attachment points for both open circuit voltage and short circuit current. The injection current was swept from 1 KHz through 10 MHz, although a strong injection current signal below 20 KHz was not possible because of the low end response of the RF power amplifier.

Figure 2.8 shows an instrumentation block diagram for the cable coupling tests done using the Marx Generator and High Current Bank shots. The capacitor

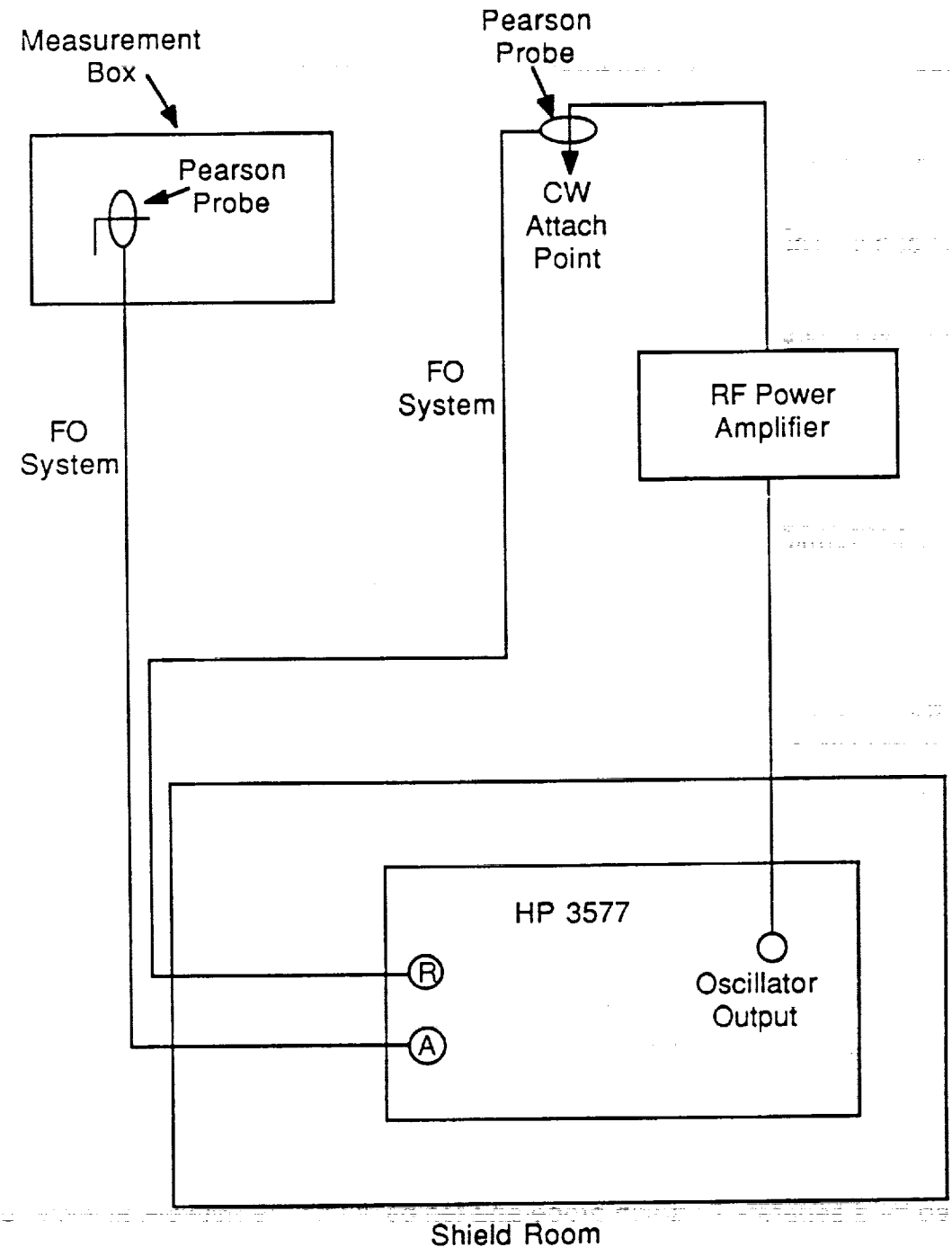

Figure 2.7 Instrumentation Block Diagram for Swept CW Tests

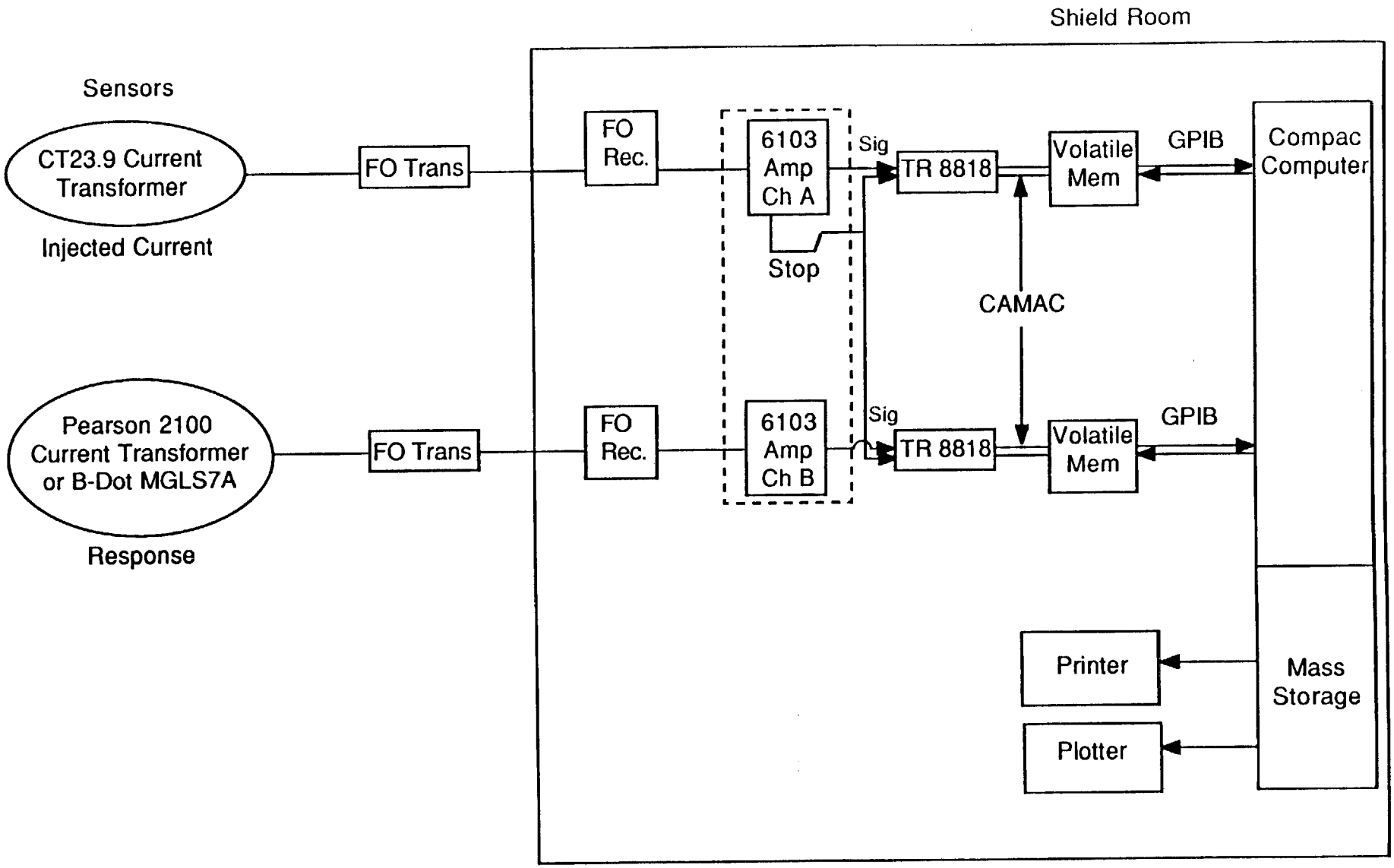

Figure 2.8 Instrumentation Block Diagram for Marx Generator and High Current Bank Test Shots

bank is connected to the top half of the peaking capacitor grid and a down conductor is connected to the grid just over the desired attachment point. A T&M Research CT23.9 current transformer probe around the down conductor is utilized to measure the injected current. The injected current probe is connected to a Nanofast fiber optic transmitter and then to the fiber optic receiver by way of the fiber optic cable. A LeCroy TR8818 digitizer is utilized to acquire and store the data with signal preconditioning done in the LeCroy 6103 amplifier. The digitizer stores the transient signal in its volatile memory and then transmits the signal to the Compaq computer by means of the GPIB interface, where the signal is displayed on the computer's screen and then stored on hard disk. Later, the signal is analyzed and plotted out. The cable response, as measured by the Pearson 2100 probe (as described earlier), is transmitted to the computer by the same means as the injected current, except through a separate fiber optic system, amplifier channel and digitizer. Also, the surface current density response on the SRB case can be measured by connecting the fiber optic transmitter to a B-dot MGLS7A probe instead of the Pearson 2100. The trigger is always off of the injected current.

Figure 2.9 shows an instrumentation block diagram much the same as Figure 2.8 except for the Intermediate and Continuing current banks. The differences are that the injected current is measured by means of a CVR (current viewing resistor) at the bank itself, and a Meret fiber optic system good down to zero Hertz (the Nanofast is only good above 160 Hertz). The response signal, however, uses the Nanofast fiber optic system. Also, LeCroy TR8837 digitizers are used with a LeCroy 8501 clock to reduce the digitizer's sample rate for the slower signals that the Intermediate and continuing current banks put out.

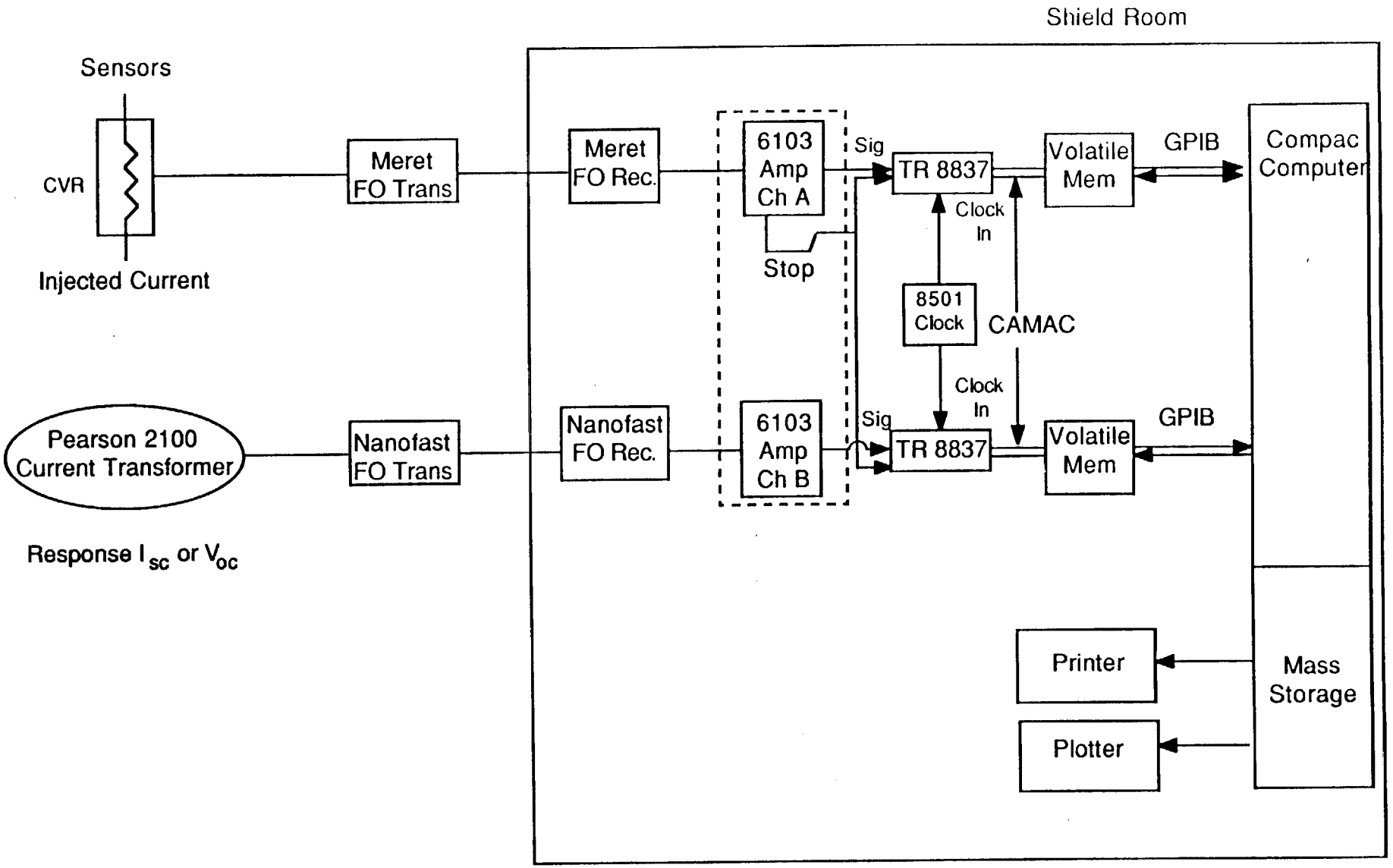

Figure 2.9 Instrumentation Block Diagram for Intermediate and Continuing Current Bank Test Shots

CHAPTER 3
TEST RESULTS

3.1 Introduction

The threat level tests performed with the Marx and the High current bank are presented in the next section (3.2), along with a rationale of why those particular tests were chosen as worse case and how those tests were scaled to the NASA 200 kA, 10^{11} dI/dT threat specification. Then a section (3.3) is presented discussing the linearity (extrapolation) of scaling a cable response due to a linear scaling of the injection current. The effect of the system tunnel cover to SRM case external bond strap on cable coupling versus that of the standard internal bond strap is presented in Section 3.4. Finally, Section 3.5 discusses the accuracy of the measurements taken inside the measurement boxes described in the previous chapter.

3.2 Swept CW and Cable Coupling From Marx Generator and High Current Bank Test Shots

As discussed in Chapter 2, a total of fifteen cables and five injection current attachment points were used during the SRB system tunnel cable coupling testing at Wendover. It was judged impractical due to time constraints to perform all possible combinations (300 = 15 cables x 5 attachment points X 2 (V_{oc} & I_{sc}) x 2 (Marx & High Current Bank) in a search for the worse case, and due to concerns of overstressing the test article. The accepted strategy was to perform swept CW measurements for the entire matrix, determine the attachment point for worse case coupling from these CW measurements, and then test all of the cables at this attachment point.

Figure 3.2.1 shows two short circuit current swept CW curves for USBI cable 4 with attach point 3 (forward case, solid curve) and 5 (DFI sensor, dashed curve). Visually, one can tell that the area under the attach point 3 curve is greater than for attach point 5, indicating that there is greater coupling at attach point 3 than for 5. This type of visual comparison was made for each of the cables at all of the attach points, yielding the table superimposed on Figure 3.2.1. The table shows which attach point gave the greatest coupling for a given cable, where coupling on several cables experienced about the same coupling levels on two or more attachment points such as

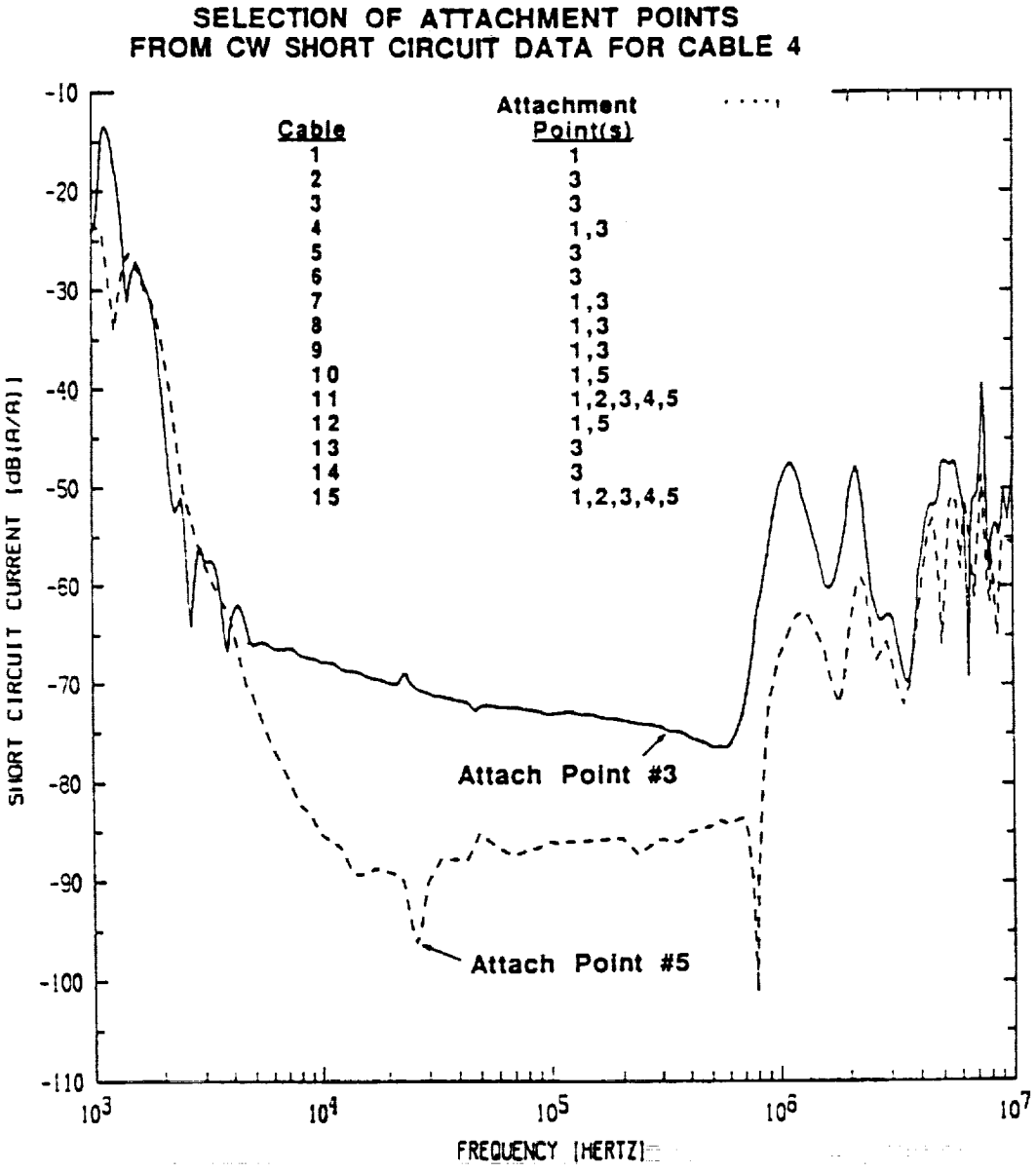

Figure 3.2.1 Comparison of Area Under Short Circuit Current CW Curves to Determine Attachment Points With Greatest Coupling. Example Shown For Cable 4. Table Indicates Attachment Point 3 is Worse Case

cable 15 for all five attach points. Attachment point 3 predominates the list, and it is at attach point 3 that all of the cables were tested with the Marx and High current bank.

The threat level tests performed at the Wendover test site have different injection current waveshapes and characteristics from the NASA ground threat specification (see Figure 2.2), which is the specification against which the SRB's lightning protection status is to be gauged. Time did not permit a rigorous Fourier analysis scaling of the threat level test results to the NASA specification, so an alternative approach was utilized. Figure 3.2.2 gives the injection current and short circuit current for cable 6 at attach point 3, with Figure 3.2.3 giving the same but for open circuit voltage. It was judged that the lower frequency ringing shown in Figure 3.2.2B (and barely perceptible in Figure 3.2.3B) was due to resistive coupling because of how the cable response appears proportional to the main ringing of the Marx injection current. The higher frequency ringing, also shown in Figures 3.2.2B and 3.2.3B, is attributed to inductive coupling due to how it appears proportional to the derivative of the Marx injection current. For Figure 3.2.2B, the resistive part of the short circuit current was judged to have a peak current of 2.0 amps, with the inductive part being the difference between the true peak current (4.7 amps) and the resistive, giving 2.7 amps.

These values for the inductive and resistive parts of the short circuit cable response are shown in the cable 6 entry of Table 3.2.1, as is the peak injection current level and dI/dT. Table 3.2.1 also shows the High current bank injection currents and cable short circuit current responses which are purely resistively coupled. Table 3.2.2 then shows how the Marx I_{SC}'s inductive part is scaled by the ratio of the NASA specification's threat dI/dT (10^{11}) to the Marx's injection current dI/dT (1.06×10^{11} for cable 6). The Marx I_{SC}'s resistive part is scaled by the ratio of the NASA specification's threat peak current (200,000 amps) to the Marx's injection current peak (29,700 amps for cable 6). The High current bank's I_{SC} is scaled the same as for the Marx's resistive part, to the 200,000 amp NASA specification. The Marx's inductive and resistive parts are added to provide the Marx scaled test threat level, and as a worse case consideration the High current bank's scaled I_{SC} (which is resistive) is added to the Marx's inductive part, and the maximum of the two values taken. This is shown in Table 3.2.2 as the "Test Peak Scaled Cable I_{SC}" column. The test configuration was a shortened version of the SRB, so there exists a need to scale these results to the full flight configuration. These results are shown in the last column of Table 3.2.2 titled

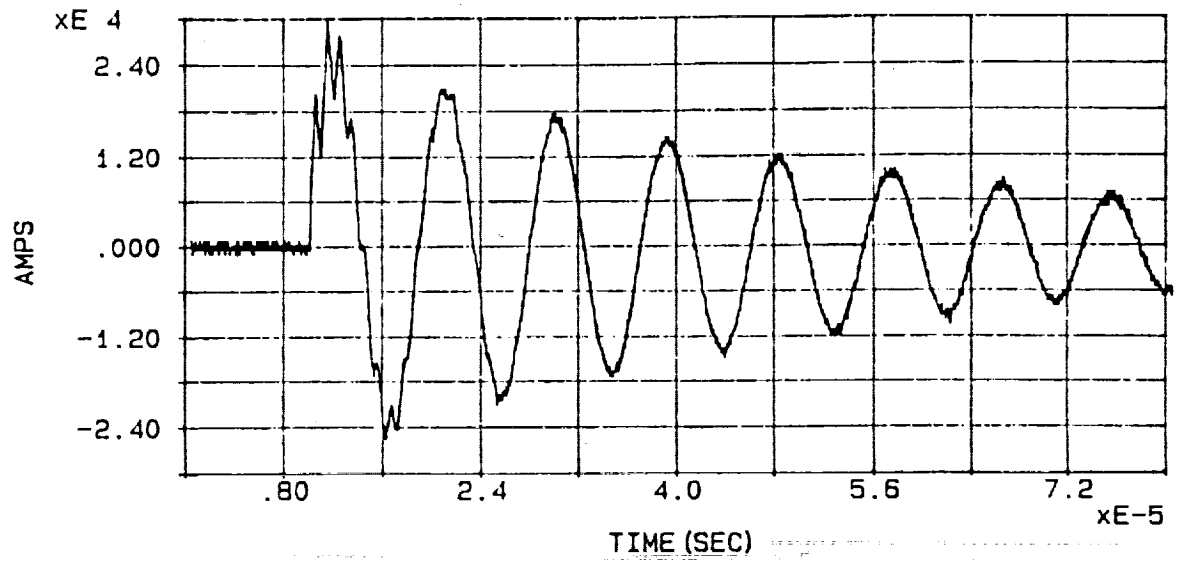

Figure 3.2.2A Peak Current = 29,710 amps
Action Integral = 8,362 amp^2-sec
Peak DI/DT = 1.063 X 10^{11} amps/sec

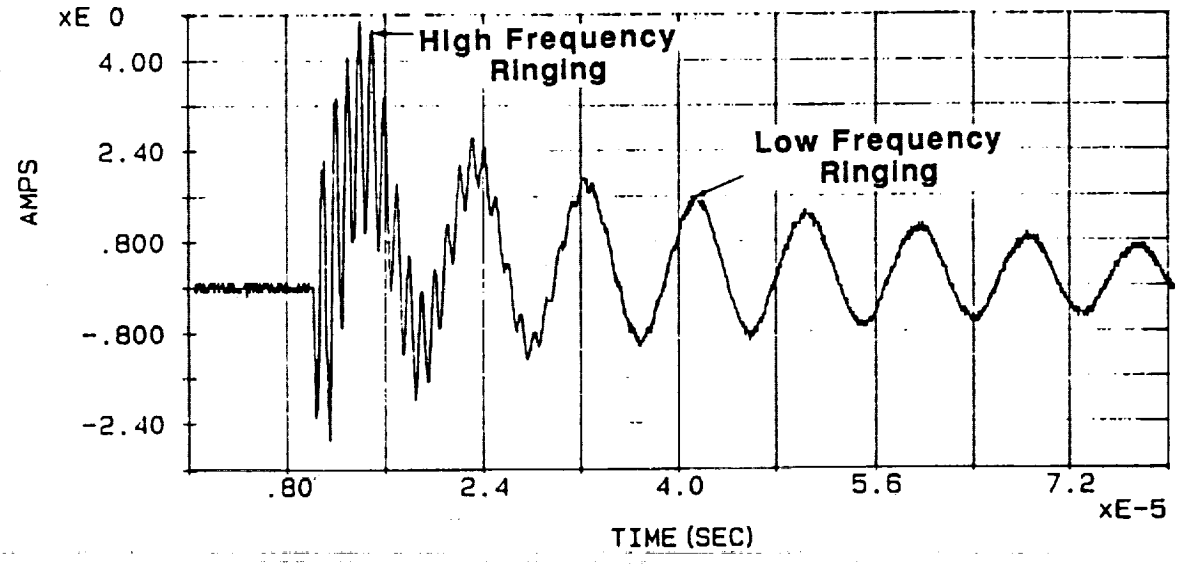

Figure 3.2.2B Peak Short Circuit Current = 4.702 amps

Figure 3.2.2 Marx Injection Current (A) And Cable 6 Short Circuit Current (B) at Attachment Point 3 (Case)

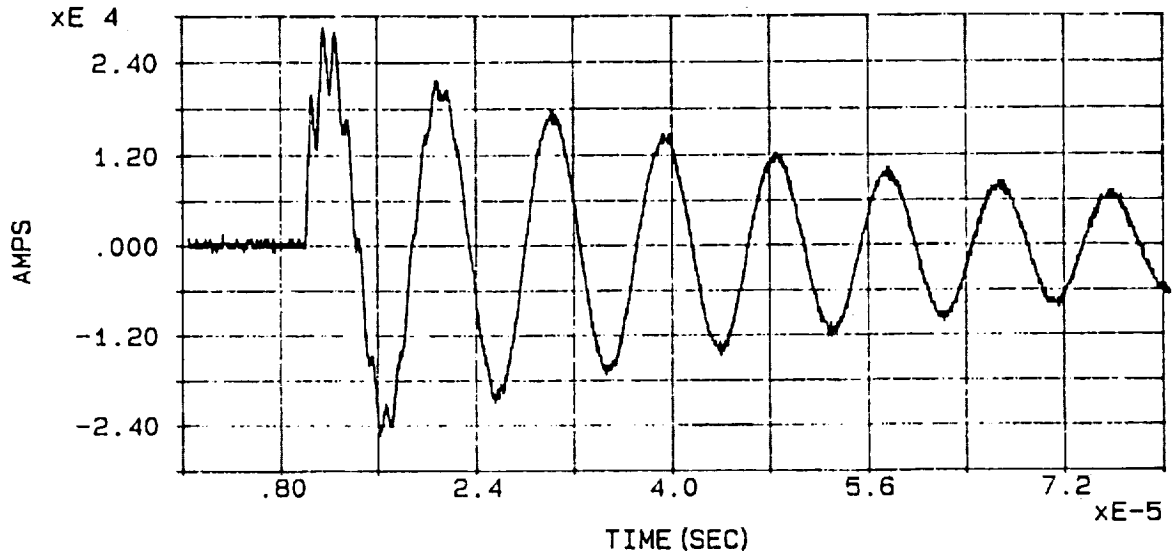

Figure 3.2.3A Peak Current = 29,230 amps
Action Integral = 8,330 amp^2-sec
Peak DI/DT = 9.818 X 10^{10} amps/sec

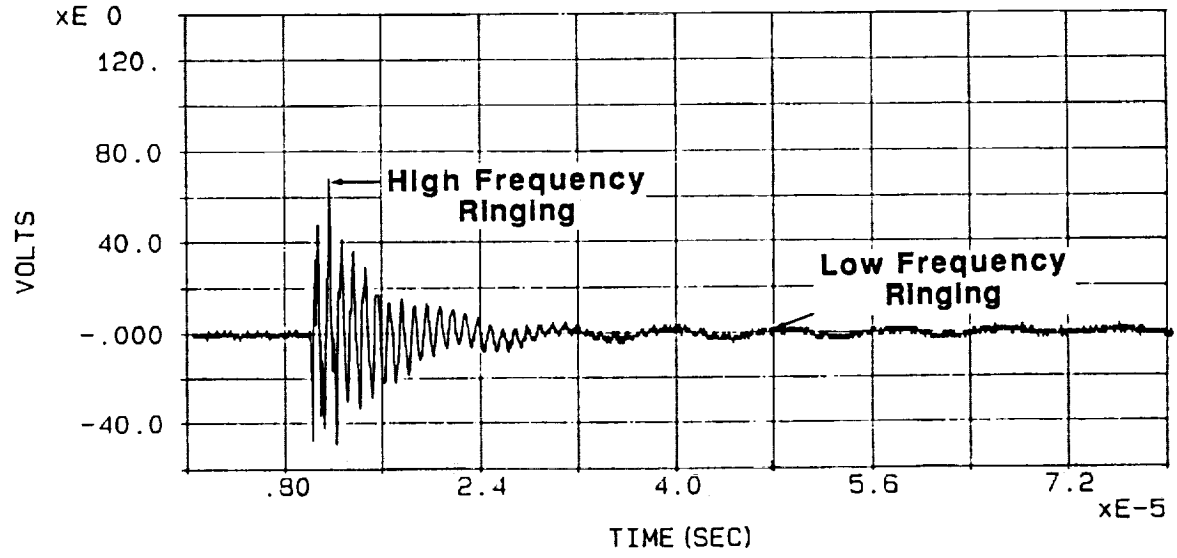

Figure 3.2.3B Peak Open Circuit Voltage = 72.08 volts

Figure 3.2.3 Marx Injection Current (A) And Cable 6 Open Circuit Voltage (B) at Attachment Point 3 (Case)

TABLE 3.2.1

MARX & HIGH CURRENT BANK DATA, WITH INDUCTIVE AND RESISTIVE I_{sc} SEPARATED. ALL CABLES AT ATTACHMENT POINT 3 (CASE)

CABLE	MARX PEAK DI/DT (X 1.0E+10) (AMPS/SEC)	MARX PEAK INJ. CUR. (KILO-AMPS)	MARX IND. I_{sc} (AMPS)	MARX RESIS. I_{sc} (AMPS)	HCB INJ. CUR. (KILO-AMPS)	HCB I_{sc} (AMPS)	OWNER
1	5.90	20.1	1.2	9.8	94.9	40.5	THIOKOL
2	7.09	19.4	7.2	-	93.8	6.5	THIOKOL
3	5.40	19.1	6.6	-	95.5	0.8	THIOKOL
4	8.9	23.3	10	3	92.7	1.1	USBI
5	6.56	19.5	10.8	-	94.3	2.0	THIOKOL
6	10.6	29.7	2.7	2	101	40.9	USBI
7	9.8*	29.2*	0.28	0.4	96.2	14.5	USBI
8	11	22.5	1.1	1.5	93.6	42.4	USBI
9	6.05	19.5	3.0	0.4	93.3	8.7	THIOKOL
10	16	31.2	0.2	1	93.5	10.7	USBI
11	8.9	29.0	0.6	0.4	94.7	3.7	USBI
12	8.9	29.7	0.1	0.35	94.0	6.4	USBI
13	7.87	29.0	11	-	93.6	0.01	THIOKOL
14	8.00	28.9	2.3	-	93.6	0.01	THIOKOL
15	12.6	28.5	4.8	0.5	91.9	0.03	THIOKOL

TABLE 3.2.2
MARX & HIGH CURRENT BANK DATA, WITH INDUCTIVE I_{SC} SCALED TO 1.0E+11 AMPS/SECOND INJECTED CURRENT, AND RESISTIVE I_{SC} SCALED TO 200 KILOAMPS INJECTED CURRENT. ALL CABLES AT ATTACHMENT POINT 3 (CASE)

CABLE/ OWNER	THREAT DI/DT MARX DI/DT	THREAT INJ. CUR./ MARX INJ. CUR.	SCALED MARX IND. I_{SC} (AMPS)	SCALED MARX RESIS. I_{SC} (AMPS)	THREAT INJ. CUR./ HCB INJ. CUR.	SCALED HCB I_{SC} (AMPS)	SCALED MARX IND. I_{SC} + SCALED MARX RESIS. I_{SC} (AMPS)	SCALED MARX IND. I_{SC} + SCALED HCB I_{SC} (AMPS)	TEST PEAK SCALED CABLE I_{SC} (AMPS)	FLIGHT I_{SC} (AMPS)
1 T	1.69	9.95	2.03	97.5	2.11	85.4	100	87	100	
2 T	1.41	10.3	10.2	?	2.13	13.9	10	24	24	
3 T	1.85	10.5	12.2	?	2.09	1.68	12	14	14	
4 U	1.12	8.6	11.2	25.8	2.16	2.4	37	14	37	
5 T	1.52	10.3	16.5	?	2.12	4.24	17	21	21	
6 U	0.943	6.7	2.5	13.5	2.0	81	16	83	83	83
7 U	1.02	6.85	0.29	2.7	2.08	30.1	3.0	30	30	30
8 U	0.91	8.9	1.0	13.0	2.14	90.6	14	92	92	92
9 T	1.65	10.3	4.96	4.10	2.14	18.6	9.1	24	24	
10 U	0.625	6.4	0.125	6.4	2.14	22.9	6.5	23	23	46
11 U	1.12	6.9	0.67	2.8	2.10	7.8	3.5	8.5	8.5	18
12 U	1.12	6.7	0.1	2.4	2.13	13.6	2.5	14	14	28
13 T	1.27	6.90	14.0	-	2.14	0.0214	14	14	14	
14 T	1.25	6.92	2.88	-	2.14	0.0214	2.9	2.9	2.9	
15 T	0.794	7.02	3.81	3.51	2.18	0.0653	7.3	3.8	7.3	

"Flight I_{sc}". These are only listed for the USBI cables, and a full description of the process involved in scaling from the test configuration to the flight configuration is given in Appendix C. Tables 3.2.3 and 3.2.4 illustrate the same corrections made to V_{oc} measurements as Table 3.2.1 and 3.2.2 illustrate for I_{sc}.

Figure 3.2.4 shows in bar graph format the test configuration (not flight) results. The peak cable V_{oc} and I_{sc} occurred for cable 1, a Thiokol cable. Cable 1, as shown in Figure 2.5, exits the system tunnel close to the location of injection current attach point 3, so it is understandable that it has the greatest coupling.

Of the USBI cables, those that ran between the forward and ET measurement boxes had greater coupling than those running between the aft and ET boxes. This is due to the fact that those cables running along the forward system tunnel are closer to the injection current at attach point 3. Cable 4 had the largest open circuit voltage (120 volts), but cable 4 was the only USBI cable without an overall shield which was not flight configuration. Of the three USBI cables having overall shields and terminated at the forward measurement box, cable 7 was the only one with EMI shields and had the lowest coupling.

3.3 Extrapolation for the Marx and High Current Bank

Inherent in the scaling process of the previous section is linearity of cable response per injected current. Swept CW is done at such low power levels that it is linear, but threat level testing by the Marx and High current bank could produce nonlinear effects (air breakdown, etc.) that are difficult to predict and account for. This section presents tests performed to determine linearity of Marx and High current bank shots.

Figure 3.3.1 shows the injected Marx current and open circuit voltage for a test to cable 8 at attach point 1. The peak injected current was 29.4 kA with a 1.01 x 10^{11} amps/sec dI/dT, with inductive and resistive V_{oc} estimated as 44 and 10 volts respectively. Immediately after this test, the Marx generator was charged to 20 kV instead of 30 kV as before, with Figure 3.3.2 giving the resultant waveforms. The peak injected current was 14.6 kA with 7.88 x 10^{10} amps/sec dI/dT, and inductive and resistive V_{oc} estimated at 43 and 55 volts respectively. Using the technique of the previous section of scaling separately the inductive and resistive parts and then

TABLE 3.2.3

MARX & HIGH CURRENT BANK DATA, WITH INDUCTIVE AND RESISTIVE V_{oc} SEPARATED. ALL CABLES AT ATTACHMENT POINT 3 (CASE)

CABLE	MARX PEAK DI/DT (X 1.0E+10) (AMPS/SEC)	MARX PEAK INJ. CUR. (KILO-AMPS)	MARX IND. V_{oc} (VOLTS)	MARX RESIS. V_{oc} (VOLTS)	HCB INJ. CUR. (KILO-AMPS)	HCB V_{oc} (VOLTS)	OWNER
1	7.37	19.2	36	9.0	95.5	9.9	THIOKOL
2	7.62	19.6	26.8	-	94.6	12.0	THIOKOL
3	7.34	19.8	51.3	-	95.0	9.0	THIOKOL
4	5.8	20.0	46	4	92.6	0.9	USBI
5	6.56	19.5	37.9	-	94.1	7.6	THIOKOL
6	9.8	29.2	67	5	98.1	13.1	USBI
7	8.9	29.3	13	-	95.3	6.3	USBI
8	8.9	22.2	25	2	95.3	8.0	USBI
9	6.43	19.5	37.0	1.0	92.9	13.5	THIOKOL
10	16	30.0	2.1	0.5	93.8	4.4	USBI
11	8.8	28.6	16	2	93.1	4.4	USBI
12	9.4	28.8	3.5	0.7	93.8	3.0	USBI
13	9.28	28.8	38.0	3.0	92.8	0.2	THIOKOL
14	9.82	28.4	38.0	2.0	93.7	0.3	THIOKOL
15	9.69	28.5	42.0	3.5	92.2	0.3	THIOKOL

TABLE 3.2.4

MARX & HIGH CURRENT BANK DATA, WITH INDUCTIVE V_{oc} SCALED TO 1.0E+11 AMPS/SECOND INJECTED CURRENT, AND RESISTIVE V_{oc} SCALED TO 200 KILOAMPS INJECTED CURRENT. ALL CABLES AT ATTACHMENT POINT 3 (CASE)

CABLE/ OWNER	THREAT DI/DT MARX DI/DT	THREAT INJ. CUR./ MARX INJ. CUR.	SCALED MARX IND. I_{sc} (AMPS)	SCALED MARX RESIS. I_{sc} (AMPS)	THREAT INJ. CUR./ HCB INJ. CUR.	SCALED HCB I_{sc} (AMPS)	SCALED MARX IND. I_{sc} + SCALED MARX RESIS. I_{sc} (AMPS)	SCALED MARX IND. I_{sc} + SCALED HCB I_{sc} (AMPS)	TEST PEAK SCALED CABLE I_{sc} (AMPS)	FLIGHT V_{oc} (VOLTS)
1 T	1.36	10.4	48.8	93.8	2.09	20.7	143	70	143	
2 T	1.31	10.2	35.2	-	2.11	25.4	35	61	61	
3 T	1.36	10.1	69.9	-	2.11	18.9	70	89	89	
4 U	1.73	10	80	40	2.16	1.9	120	82	120	
5 T	1.52	10.3	57.8	-	2.13	16.2	59	74	74	
6 U	1.02	6.85	68	34	2.04	26.7	102	95	102	316
7 U	1.12	6.83	14.6	-	2.10	13.2	15	28	28	87
8 U	1.12	9.0	28	18	2.10	16.8	46	45	46	143
9 T	1.56	10.3	57.5	10.3	2.15	29.1	68	87	87	
10 U	0.625	6.67	1.3	3.3	2.13	9.4	4.6	11	11	23
11 U	1.14	7.0	18.2	14	2.15	9.5	32	28	32	66
12 U	1.6	6.9	3.7	4.9	2.13	6.4	8.6	10	10	10
13 T	1.08	6.94	40.9	20.8	2.16	0.43	62	41	62	
14 T	1.02	7.04	38.7	14.1	2.13	0.64	53	39	53	
15 T	1.03	7.02	43.3	24.6	2.17	0.65	68	44	68	

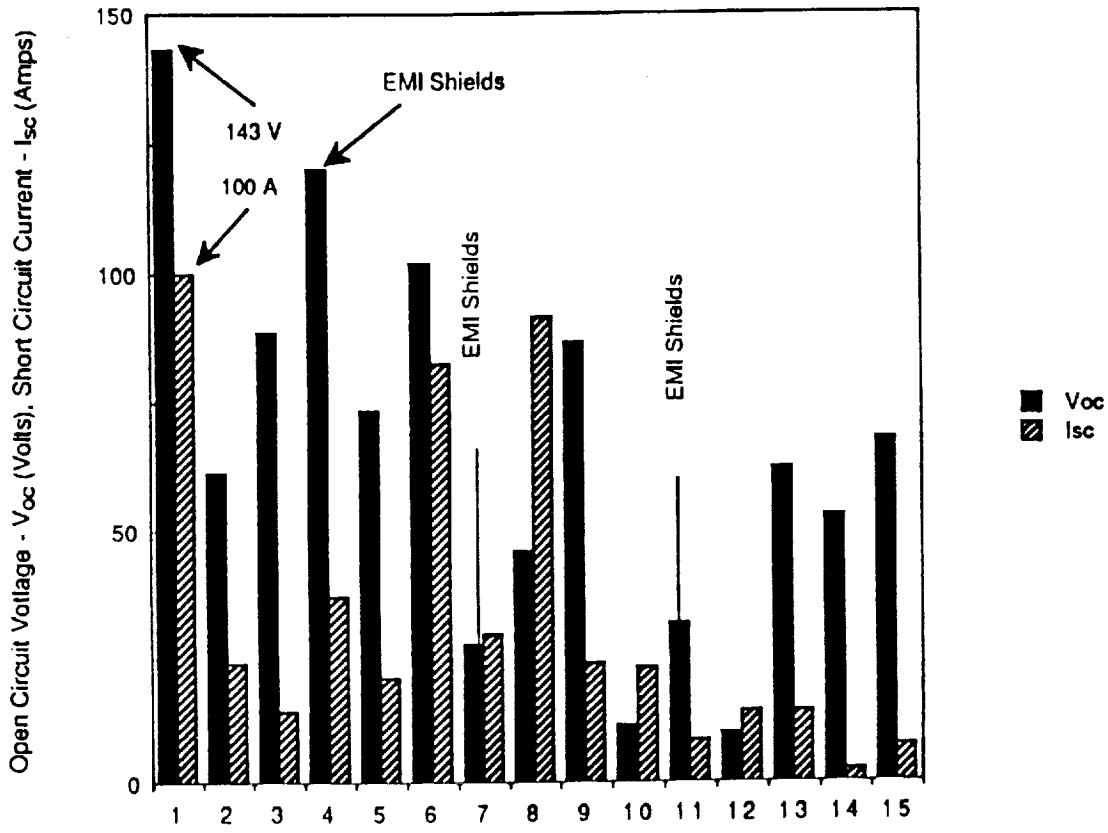

Figure 3.2.4 Marx/High Current Bank Test Results For All Cables, Attachment Point 3 (Station 539; 100°). Extrapolated To 200 kA For Resistive Part, 10^{11} amps/sec For Inductive Part

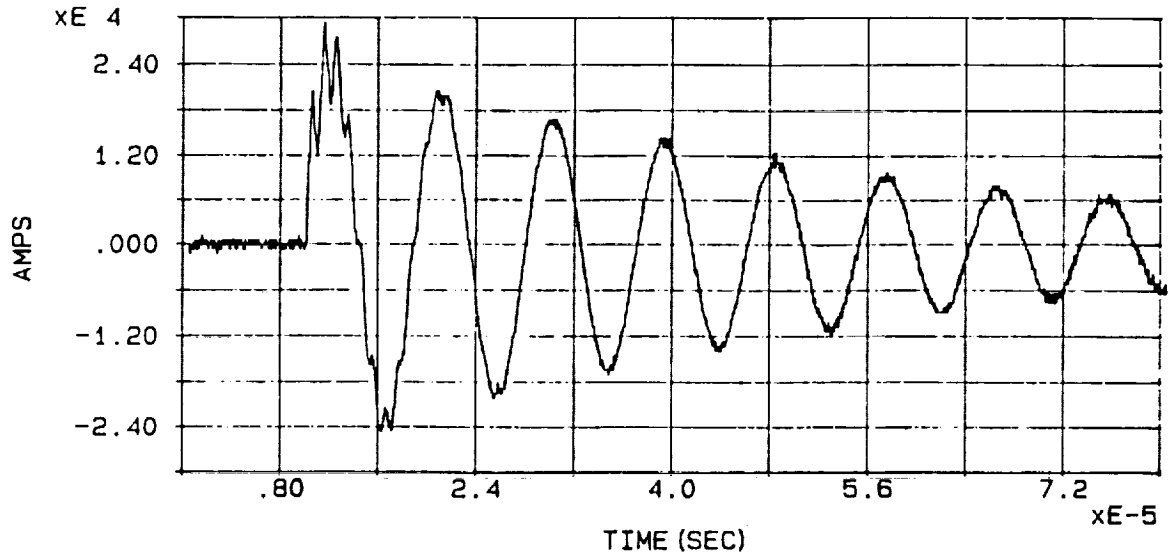

Figure 3.3.1A Peak Current = 29,420 amps
Action Integral = 8,005 amp^2-sec
Peak DI/DT = 1.007 X 10^{11} amps/sec

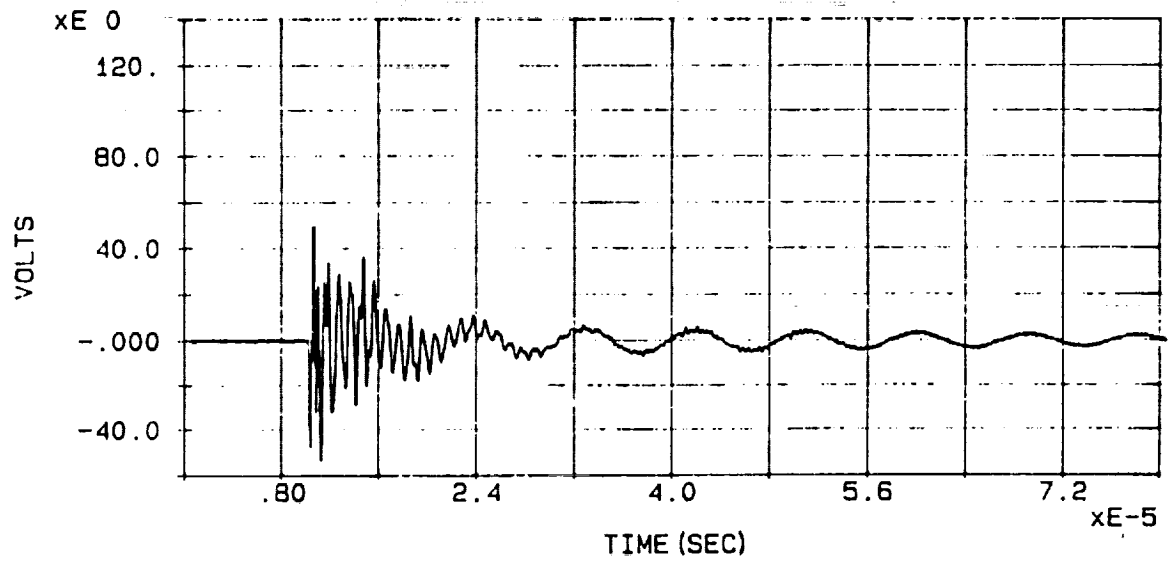

Figure 3.3.1B Peak Open Circuit Voltage = -53.55 volts

Figure 3.3.1 Marx Injection Current (A) And Cable 8 Open Circuit Voltage (B) at Attachment Point 1 (Forward System Tunnel). First Test

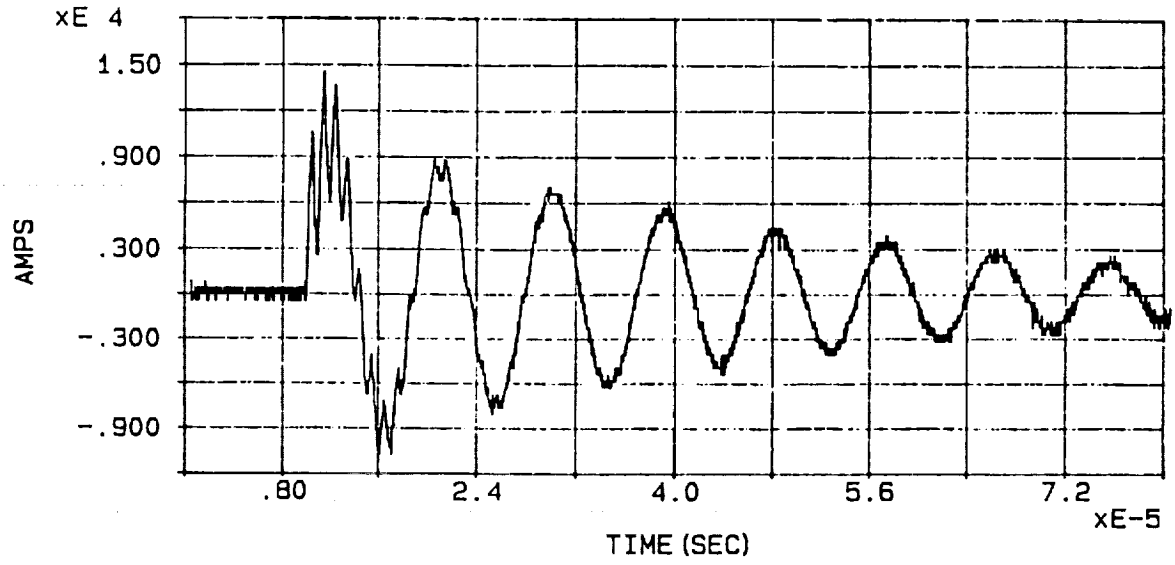

Figure 3.3.2A Peak Current = 14,620 amps
Action Integral = 1,243 amp^2-sec
Peak DI/DT = 7.883 X 10^{10} amps/sec

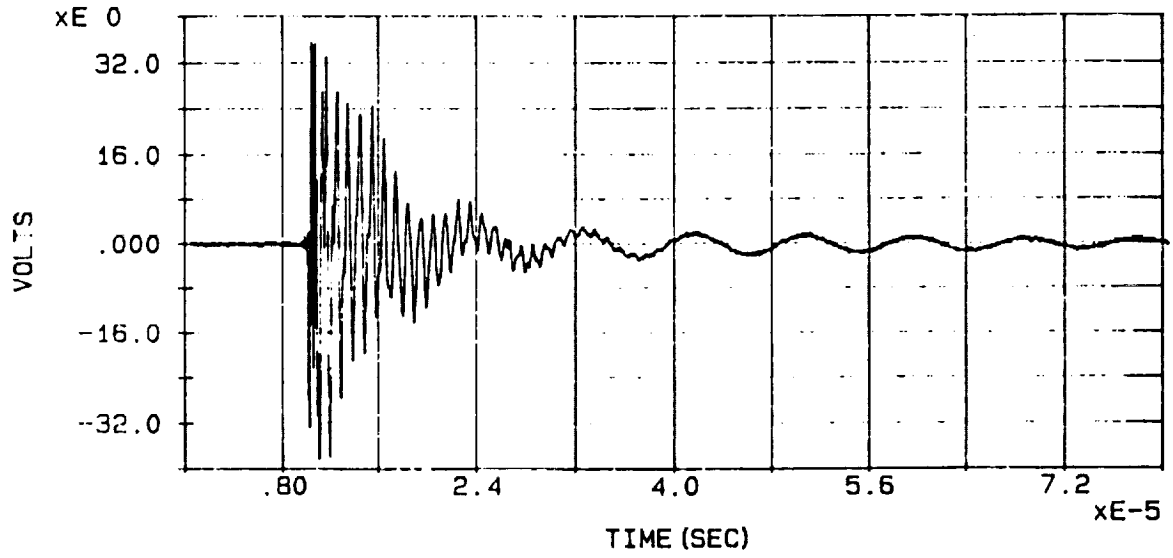

Figure 3.3.2B Peak Open Circuit Voltage = -38.22 volts

Figure 3.3.2 Marx Injection Current (A) And Cable 8 Open Circuit Voltage (B) at Attachment Point 1 (Forward System Tunnel). Second Test

adding, produces a peak current (scaled to the NASA specification) of 112 volts for Figure 3.3.1B and 98 volts for Figure 3.3.2B. Given the errors inherent in the process of picking out the inductive and resistive parts of the response, 112 versus 98 volts indicates good linearity for different level Marx test shots.

Figures 3.3.3 and 3.3.4 show the High current bank injected currents and short circuit current responses for cable 8 with attach point 3. For High current bank tests the cable coupling mode appears resistive, so scaling the response of Figure 3.3.3 to a 200 kA injected current yields 189 amp I_{sc} and 90.6 amp I_{sc} for Figure 3.3.4 9. This indicates a definite nonlinearity. Table 3.3.1 gives these results from Figures 3.3.3 and 3.3.4 as its first and last entries (A and D) respectively. The first three entries (A, B and C) consists of six consecutive shots done at the very beginning of the test sequence (after the swept CW was done). The greatest difference is between the scaled I_{sc} of shot A and C, giving 189/128 = 1.48 or 48% difference from linearity. The I_{sc} and V_{oc} shots labeled D (of Figure 3.3.4) were performed later in the test sequence, after the Marx, Intermediate and Continuing current bank shots but during the testing of all cables at attach point 3 (case) for the High current bank. Its scaled values are the smallest of these tests, with the largest original injected current levels. It is at these injection current levels (90 - 100 kA) that all of the cables were tested with attach point 3.

Table 3.3.1

High Current Bank Test Shots for Cable 8 at Attach Point 3. Scaling Done to 200 kA NASA Specification Injected Current. Nonlinear Effects Exhibited

Iden. Shot	Inject. Current (Amps)	I_{sc} (Amps)	Inject. Current (Amps)	V_{oc} (Volts)	Scaled I_{sc} (Amps)	Scaled V_{oc} (Volts)
A	26.6	25.2	27.0	4.89	189	36.2
B	55.3	48.2	55.2	9.21	174	33.4
C	88.3	56.5	87.9	16.3	128	37.1
D	93.6	42.4	95.3	8.03	90.6	16.9

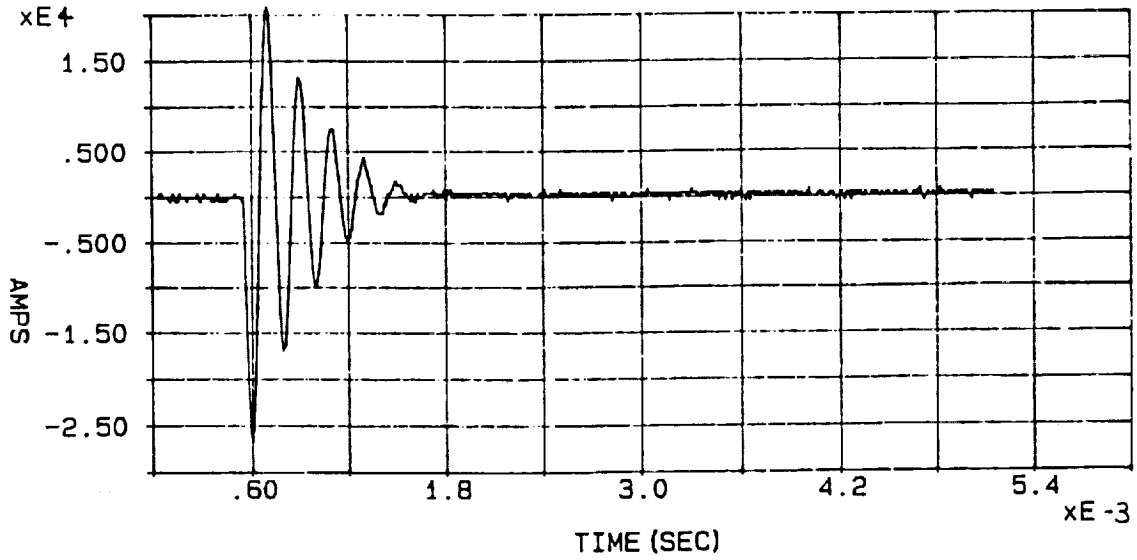

Figure 3.3.3A Peak Current = -26,600 amps
Action Integral = 89,520 amp^2-sec

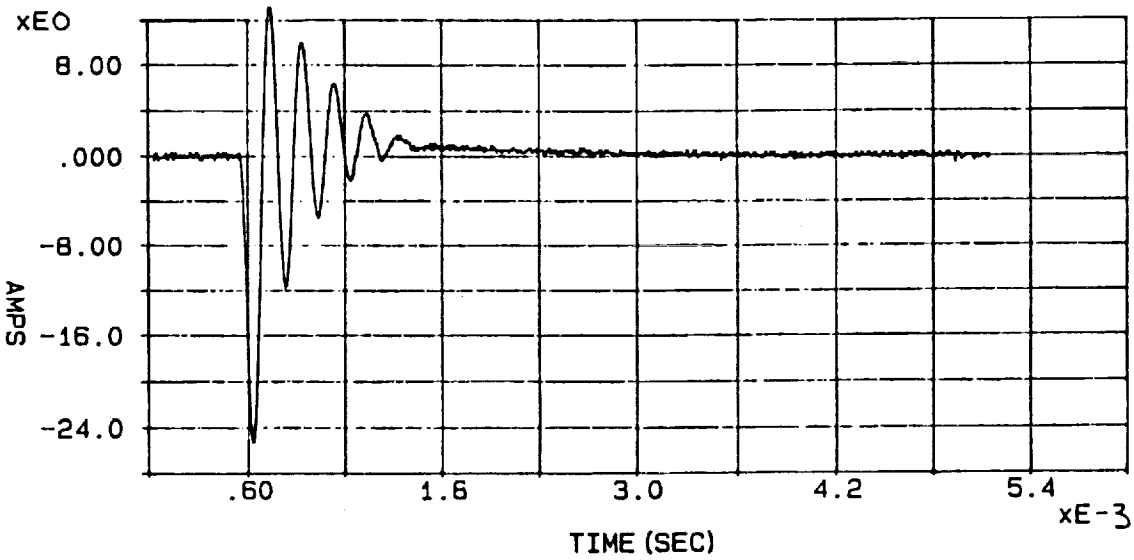

Figure 3.3.3B Peak Short Circuit Current = -25.2 amps

Figure 3.3.3 High Current Bank Injection Current (A) And Cable 8 Short Circuit Current (B) at Attachment Point 3 (Case). First Test

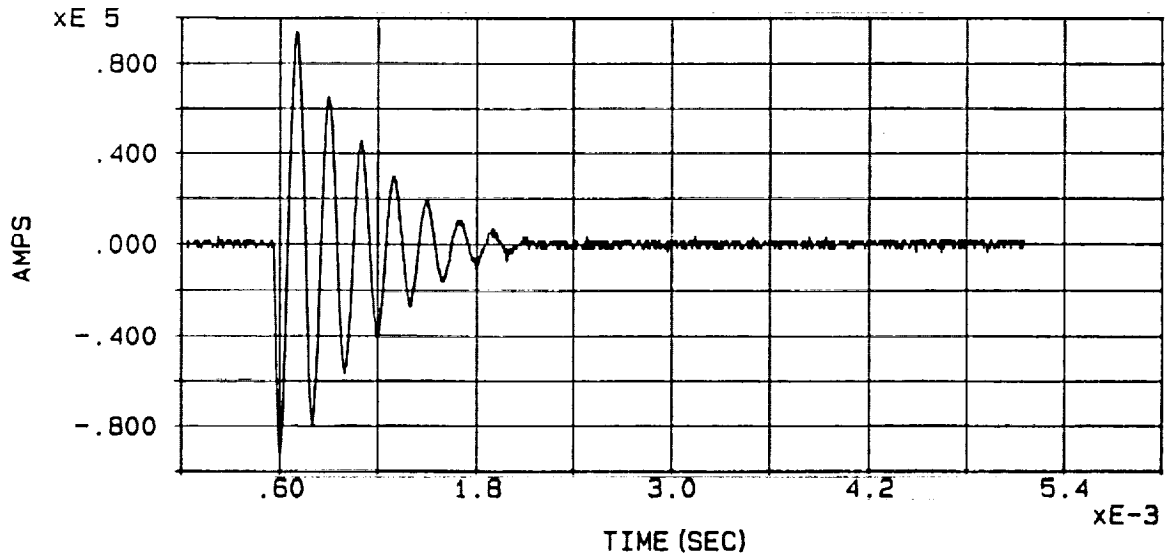

Figure 3.3.4A Peak Current = 93,600 amps
Action Integral = 1,738,000 amp^2-sec

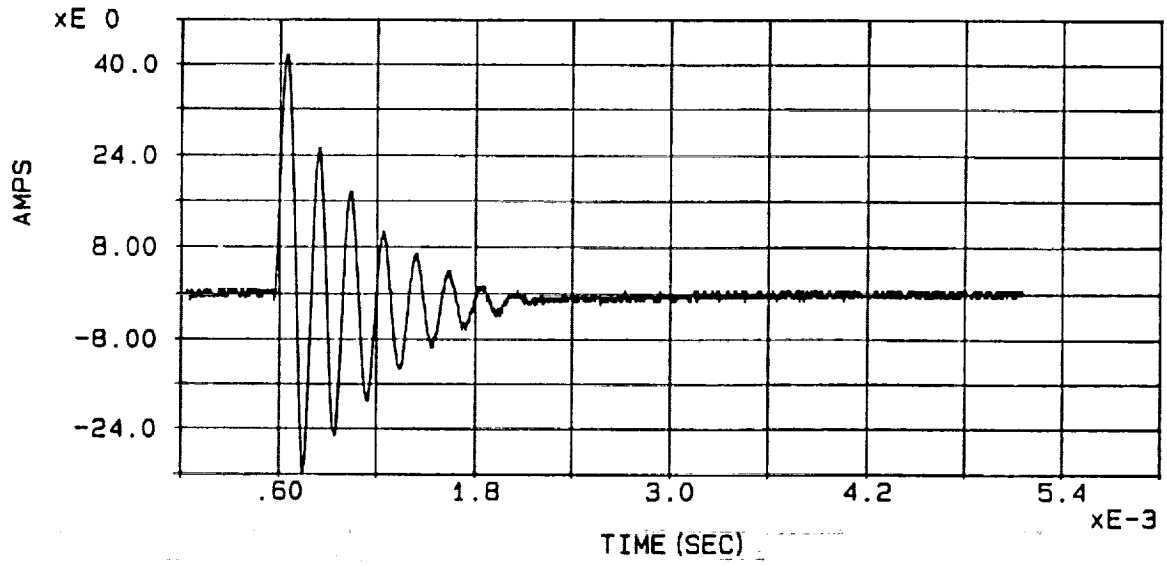

Figure 3.3.4B Peak Short Circuit Current = 42.4 amps

Figure 3.3.4 High Current Bank Injection Current (A) And Cable 8 Short Circuit Current (B) at Attachment Point 3 (Case). Fourth Test

3.4 Effect of External Bond Straps

The only bonding path for the system tunnel to the SRM case is through the internal bond straps that are epoxy bonded from the case to the system tunnel floor. It is known from testing that the bonds are destroyed at approximately 100 kA (from the High current bank), so consideration was given to creating a new type of bond strap. It is called an "external" bond strap (not to be confused with the bonding jumpers between tunnel cover segments) and connects the system tunnel cover directly to the SRM case, with four times the footprint area that the internal bond straps have. Tests conducted with these external bond straps showed that they too fail at about the same level as for the original internal bond straps, presumably because the current is not equally distributed across the footprint area but concentrates along the edges. There were concerns that the epoxy for these external bond straps had not cured long enough before testing, but subsequent coupon tests conducted at the Wendover test site have precluded this concern.

One aspect of the external bond straps is that they appear to reduce cable coupling significantly for attachment to the tunnel cover (attach point 1). Figure 3.4.1 gives the injected current and short circuit current response for cable 8 with attach point 1, and Figure 3.4.2 for the open circuit voltage. Figures 3.4.3 and 3.4.4 correspond respectively to Figures 3.4.1 and 3.4.2, with a majority of the Marx and High current bank tests conducted between the two sets of tests. Figures 3.4.5 and 3.4.6 give the short circuit current and open circuit voltage for cable 10 and attach point 1, with Figures 3.4.7 and 3.4.8 respectively the same except with a majority of the Marx and High current bank tests and all Intermediate and Continuing bank tests conducted between these two sets of cable 10 tests. The primary difference between the tests shown is that Figures 3.4.1, 3.4.2, 3.4.5 and 3.4.6 were performed with internal bond straps, and Figures 3.4.3, 3.4.4, 3.4.7 and 3.4.8 were performed with external bond straps.

Comparing the internal/external bond strap figures shows that the external bond straps reduces the cable coupling. Scaling the inductive and resistive cable responses separately to the NASA specification as in section 3.2 yields Table 3.4.1.

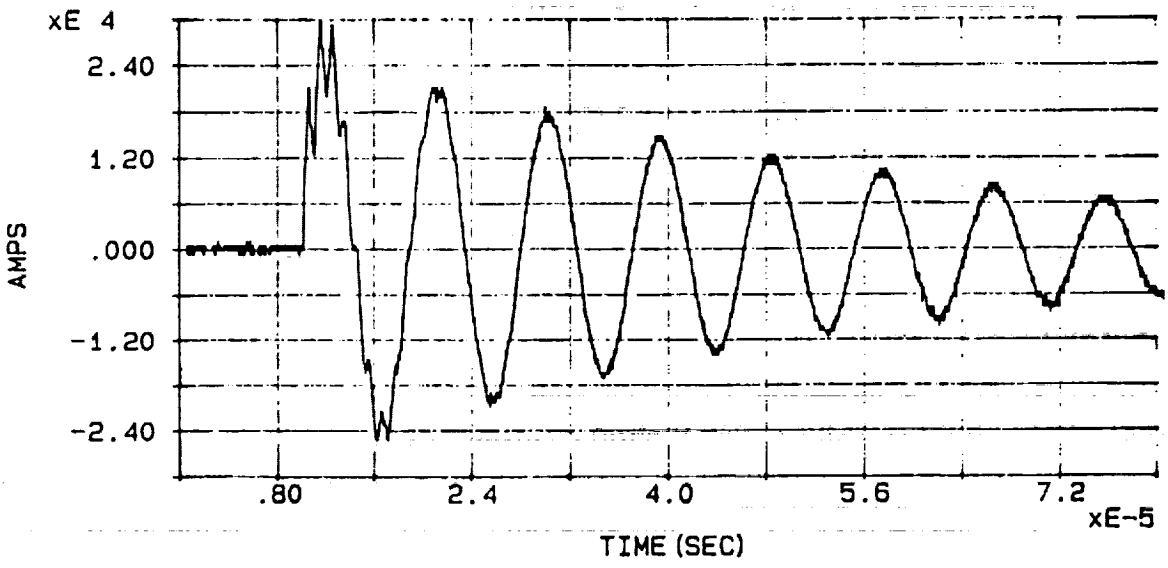

Figure 3.4.1A Peak Current = 30,010 amps
Action Integral = 8,445 amp^2-sec
Peak DI/DT = 1.060 X 10^{11} amps/sec

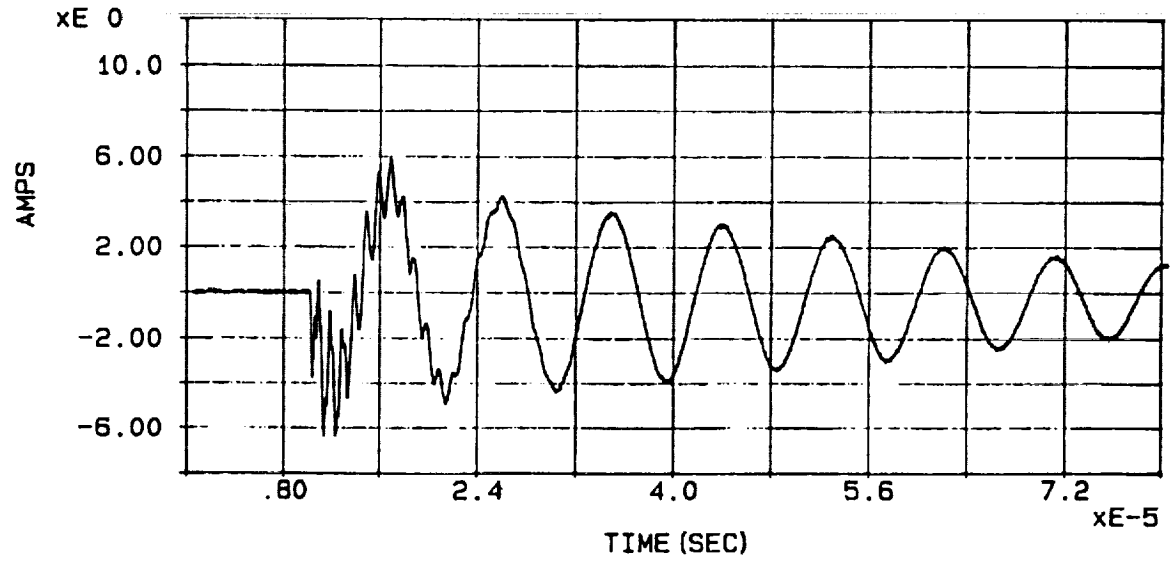

Figure 3.4.1B Peak Short Circuit Current = -6.433 amps

Figure 3.4.1 Marx Injection Current (A) And Cable 8 Short Circuit Current (B) at Attachment Point 1 (Forward System Tunnel). Internal Bond Strap

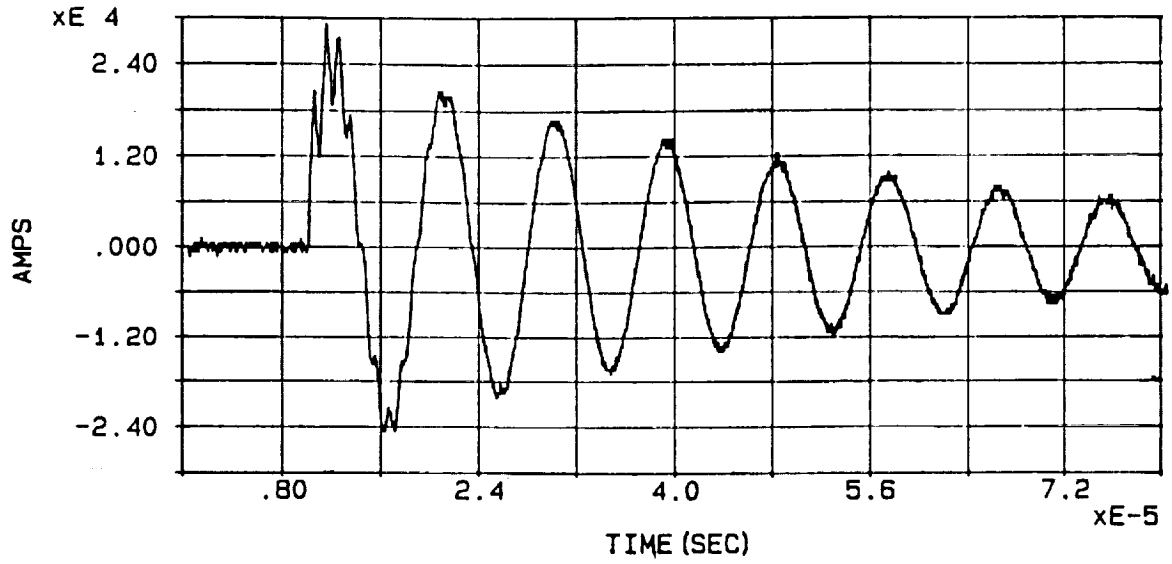

Figure 3.4.2A Peak Current = 29,420 amps
Action Integral = 8,005 amp^2-sec
Peak DI/DT = 1.007 X 10^{11} amps/sec

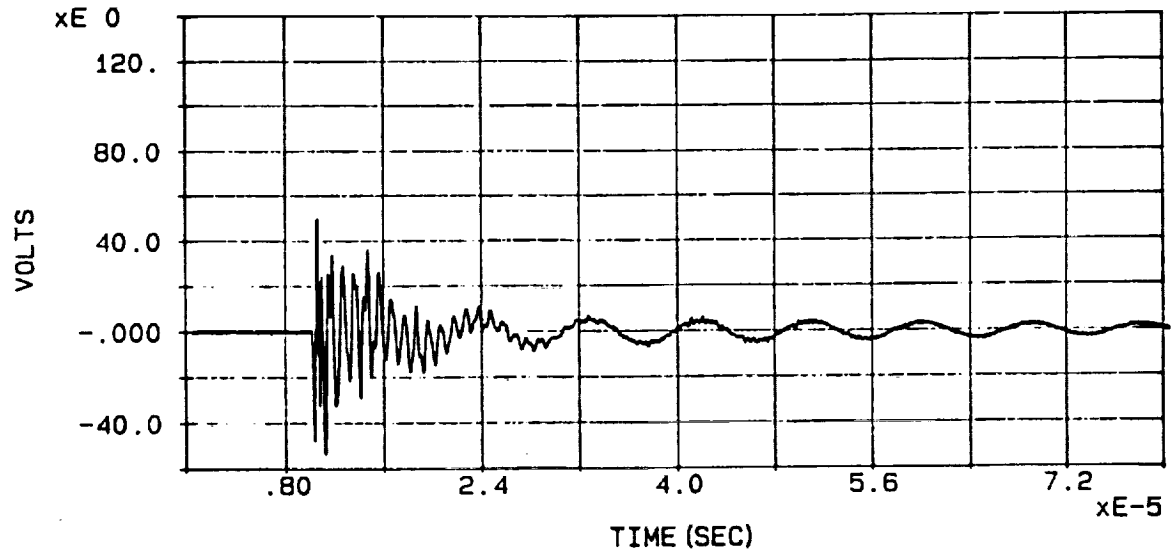

Figure 3.4.2B Peak Open Circuit Voltage = -53.55 volts

Figure 3.4.2 Marx Injection Current (A) And Cable 8 Open Circuit Voltage (B) at Attachment Point 1 (Forward System Tunnel). Internal Bond Strap

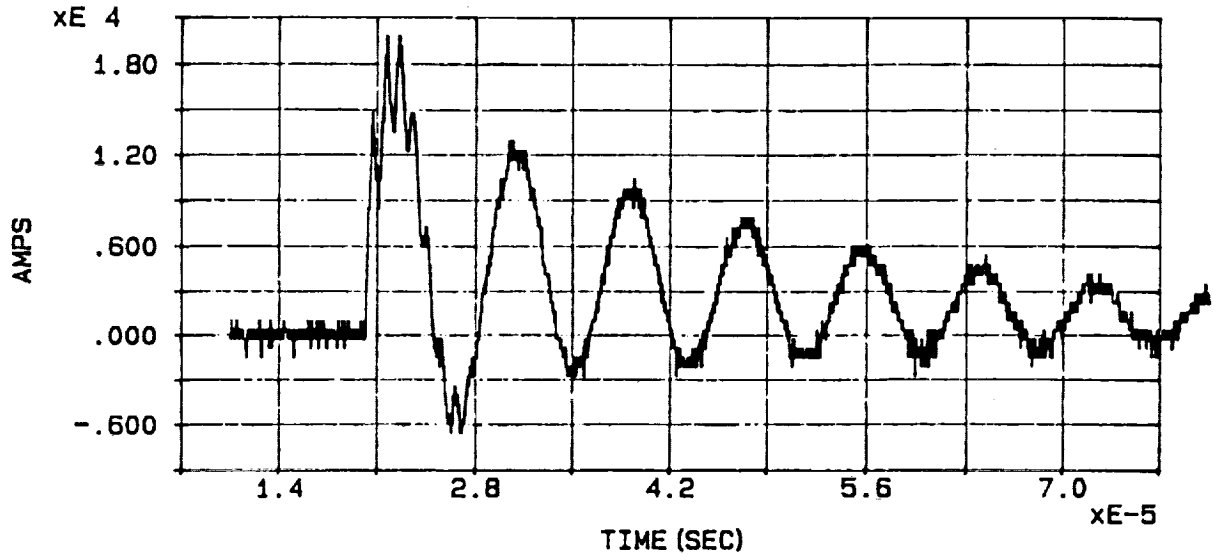

Figure 3.4.3A Peak Current = 20,480 amps
Action Integral = 1,901 amp^2-sec
Peak DI/DT = 7.496 X 10^{10} amps/sec

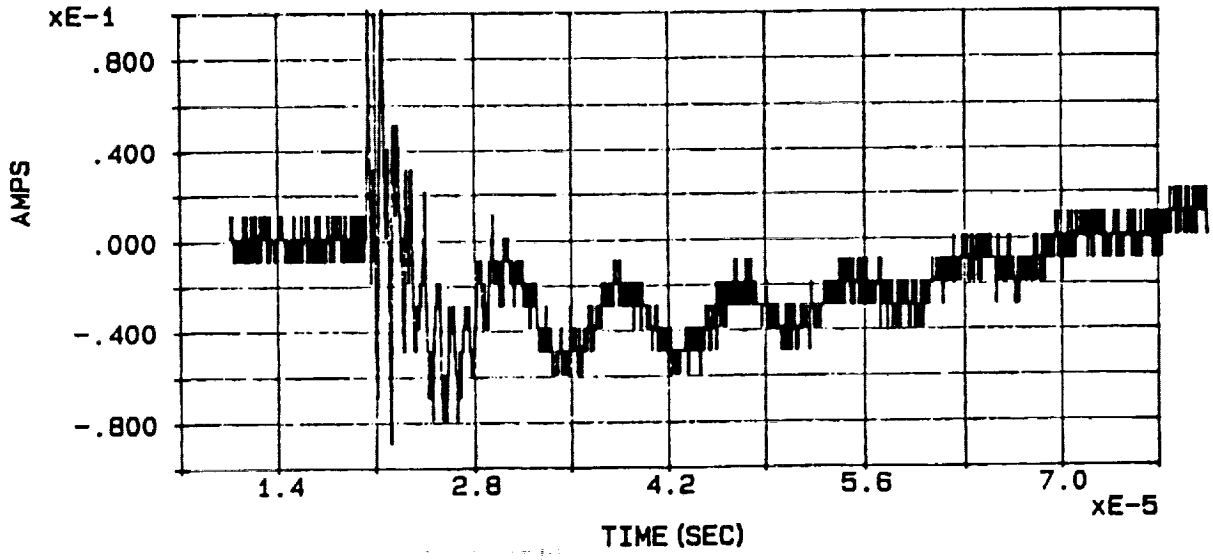

Figure 3.4.3B Peak Short Circuit Current = 0.1119 amps

Figure 3.4.3 Marx Injection Current (A) And Cable 8 Short Circuit Current (B) at Attachment Point 1 (Forward System Tunnel). External Bond Strap

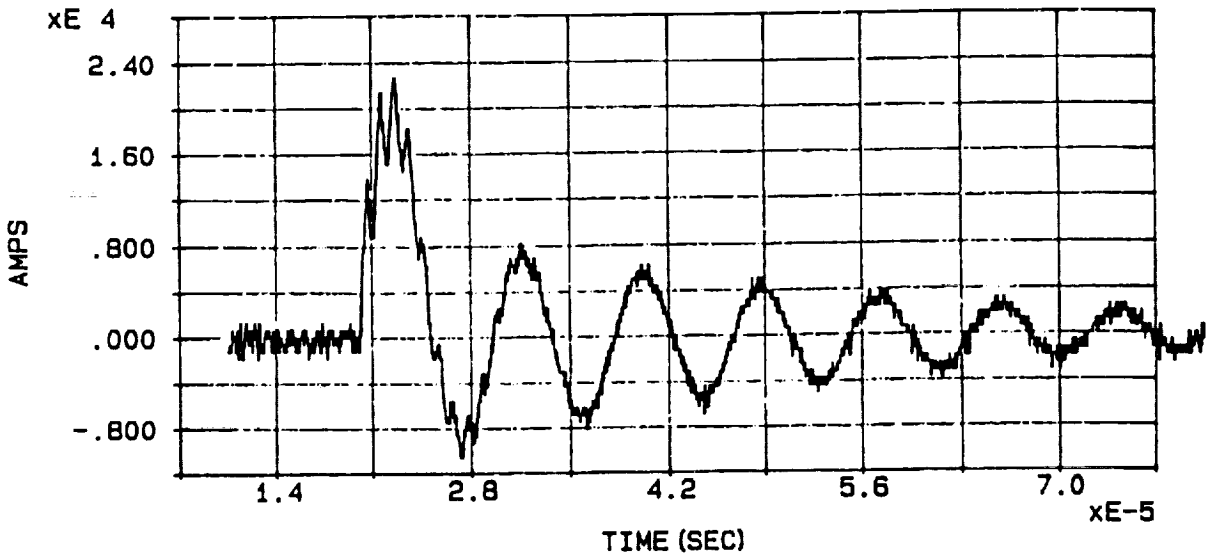

Figure 3.4.4A Peak Current = 23,300 amps
Action Integral = 1,720 amp^2-sec
Peak DI/DT = 7.371 X 10^{10} amps/sec

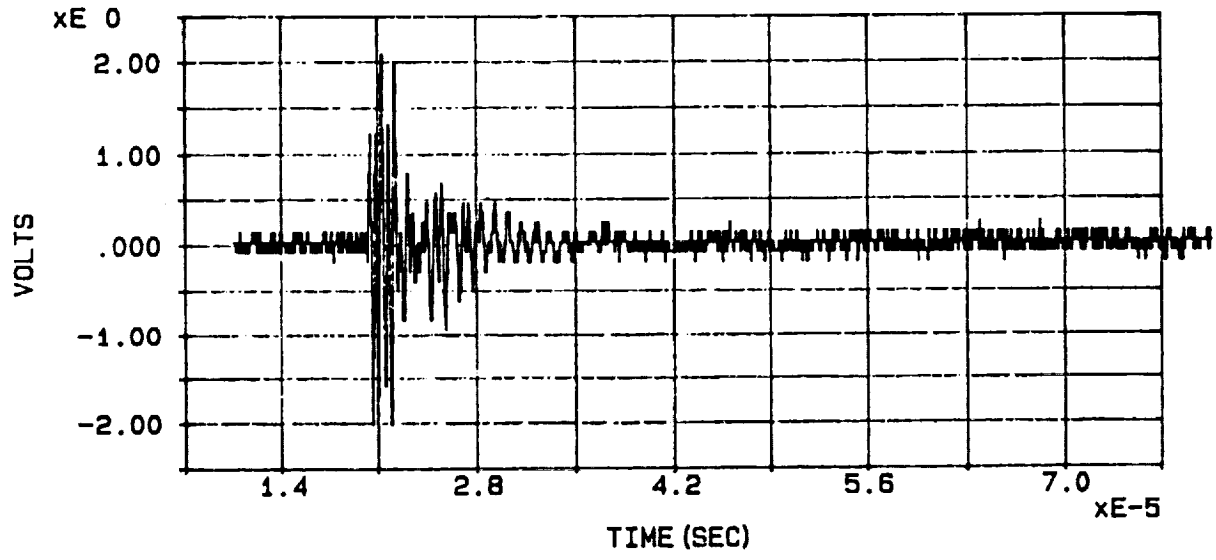

Figure 3.4.4B Peak Open Circuit Voltage = 2.194 volts

Figure 3.4.4 Marx Injection Current (A) And Cable 8 Open Circuit Voltage (B) at Attachment Point 1 (Forward System Tunnel). External Bond Strap

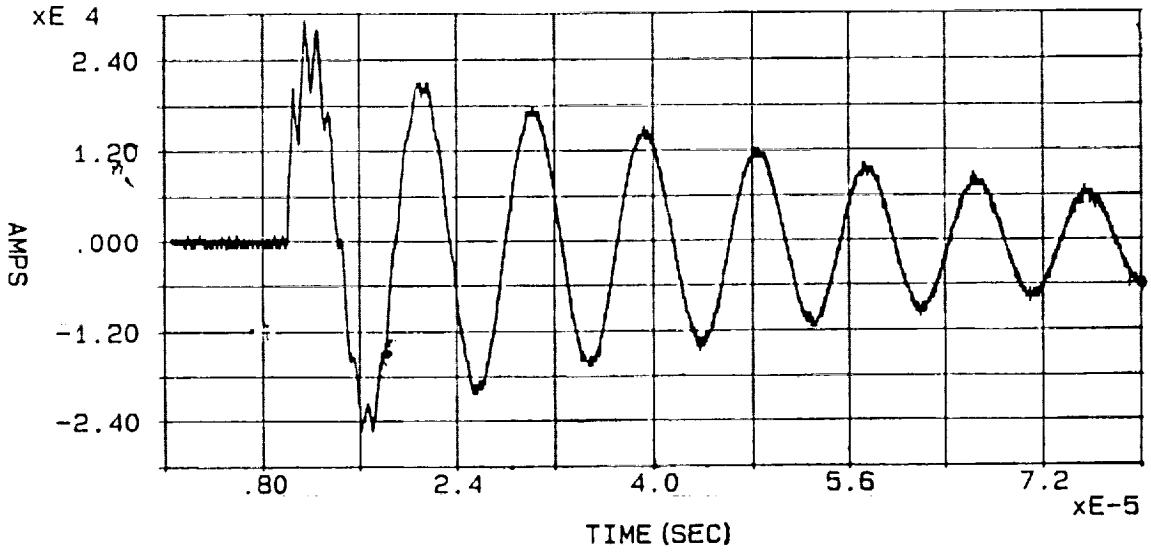

Figure 3.4.5A Peak Current = 29,250 amps
Action Integral = 8,296 amp^{2}2-sec
Peak DI/DT = 1.255 X 10^{11} amps/sec

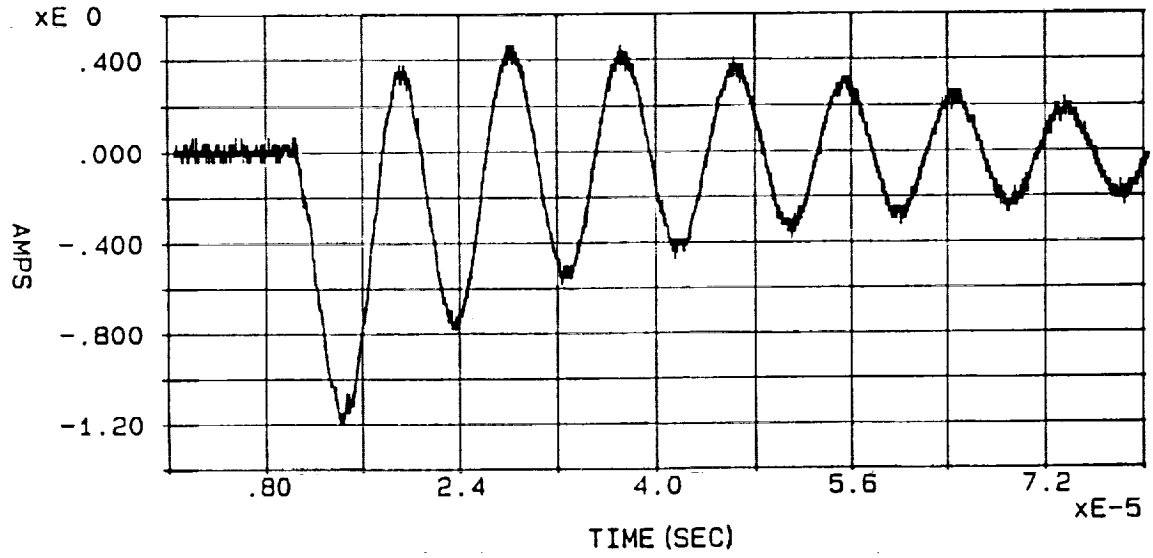

Figure 3.4.5B Peak Short Circuit Current = -1.202 amps

Figure 3.4.5 Marx Injection Current (A) And Cable 10 Short Circuit Current (B) at Attachment Point 1 (Forward System Tunnel). Internal Bond Strap

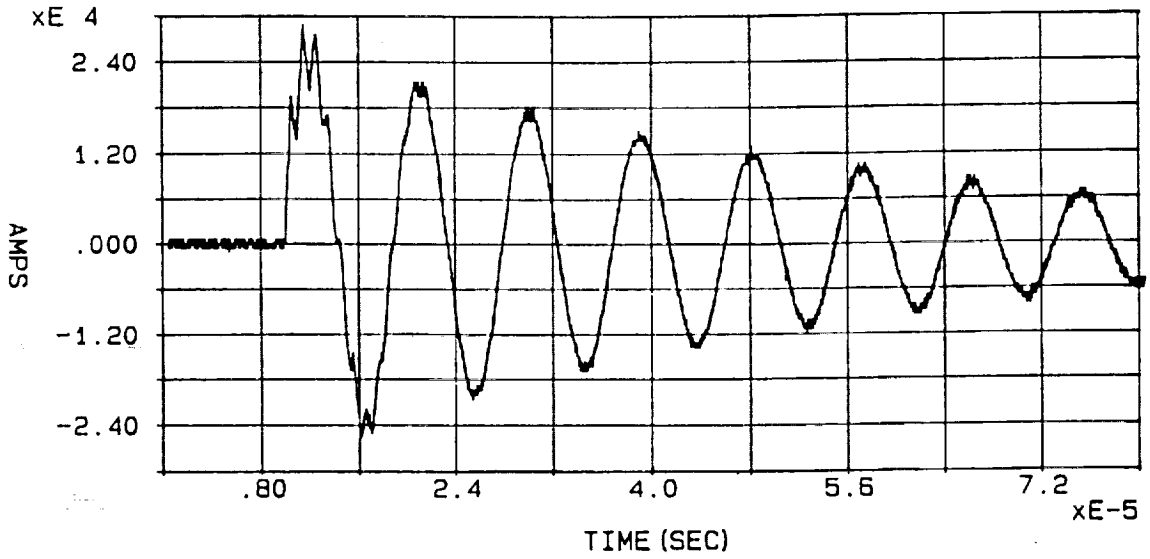

Figure 3.4.6A Peak Current = 28,920 amps
Action Integral = 8,335 amp^2-sec
Peak DI/DT = -1.255 X 10^{11} amps/sec

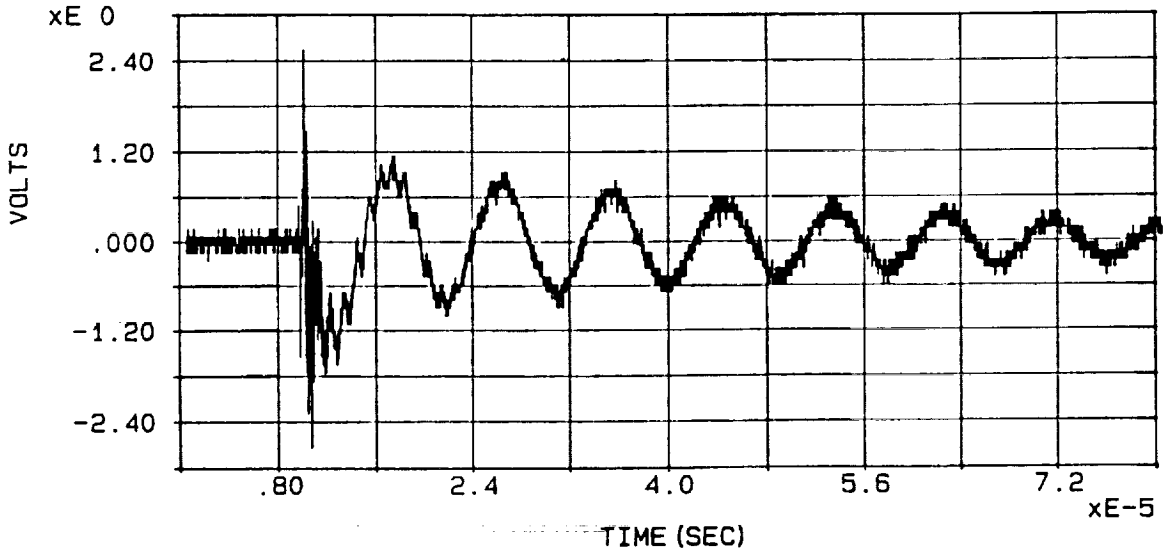

Figure 3.4.6B Peak Open Circuit Voltage = -2.837 volts

Figure 3.4.6 Marx Injection Current (A) And Cable 10 Open Circuit Voltage (B) at Attachment Point 1 (Forward System Tunnel). Internal Bond Strap

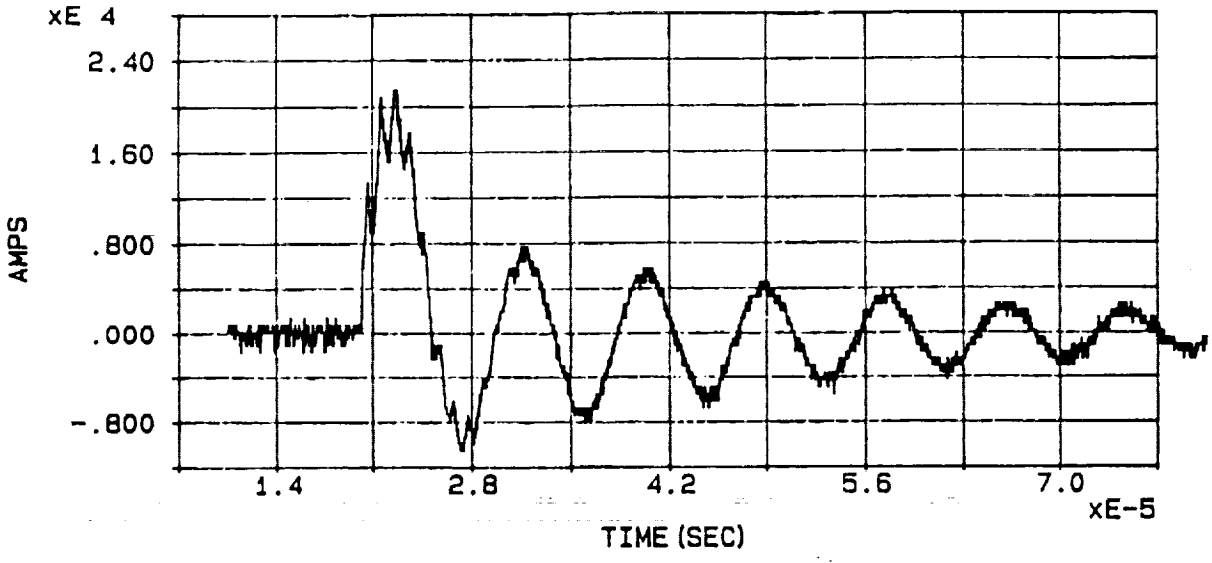

Figure 3.4.7A Peak Current = 22,780 amps
Action Integral = 1,721 amp^2-sec
Peak DI/DT = 7.214 X 10^{10} amps/sec

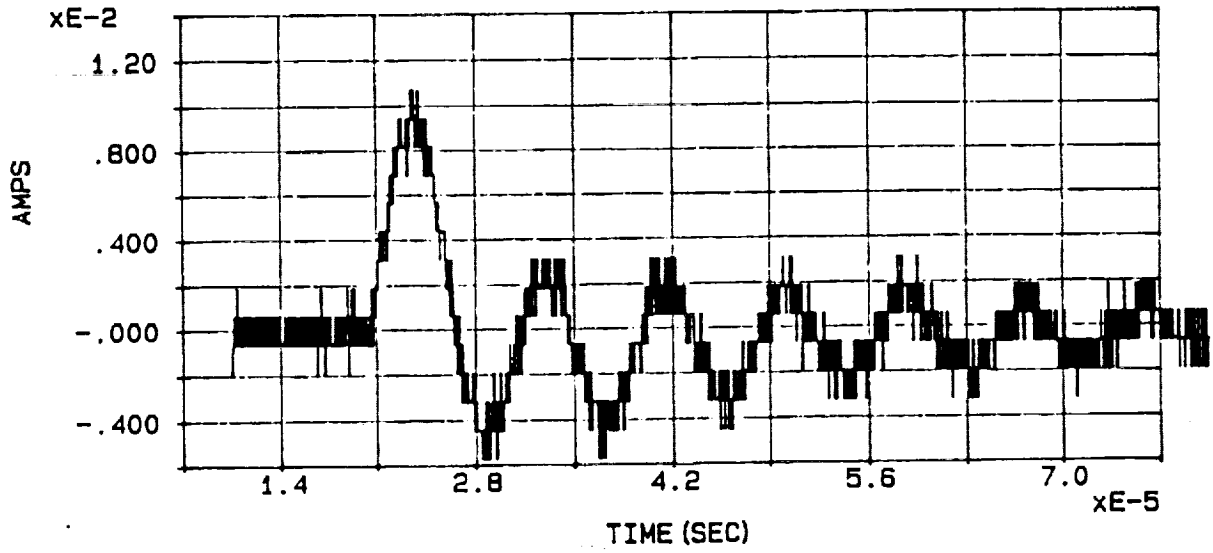

Figure 3.4.7B Peak Short Circuit Current = 0.01198 amps

Figure 3.4.7 Marx Injection Current (A) And Cable 10 Short Circuit Current (B) at Attachment Point 1 (Forward System Tunnel). External Bond Strap

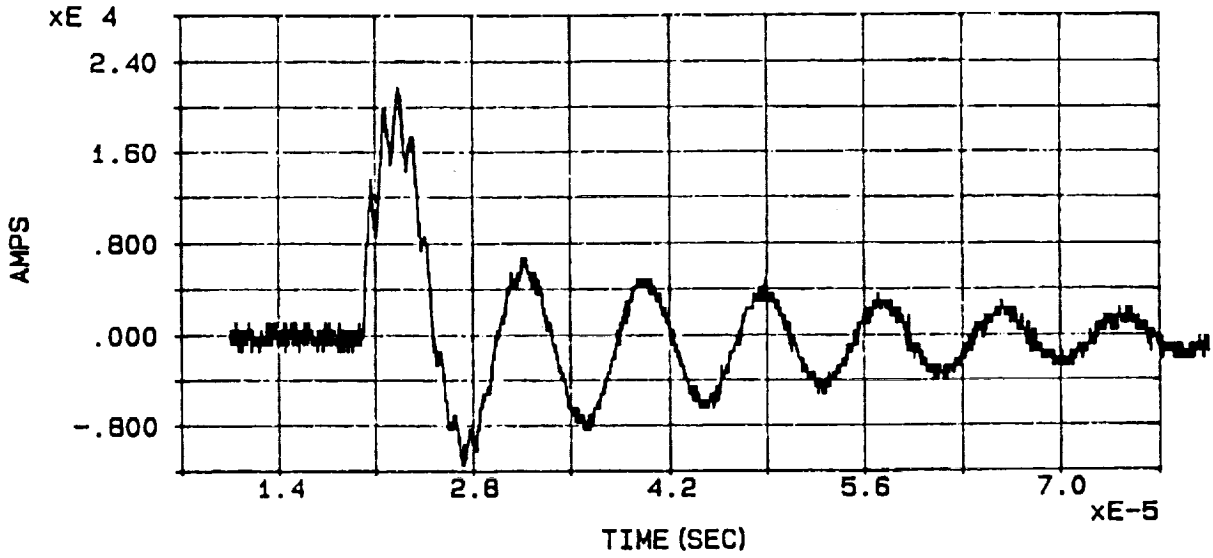

Figure 3.4.8A Peak Current = 21,810 amps
Action Integral = 1,716 amp^2-sec
Peak DI/DT = 8.406 X 10^{10} amps/sec

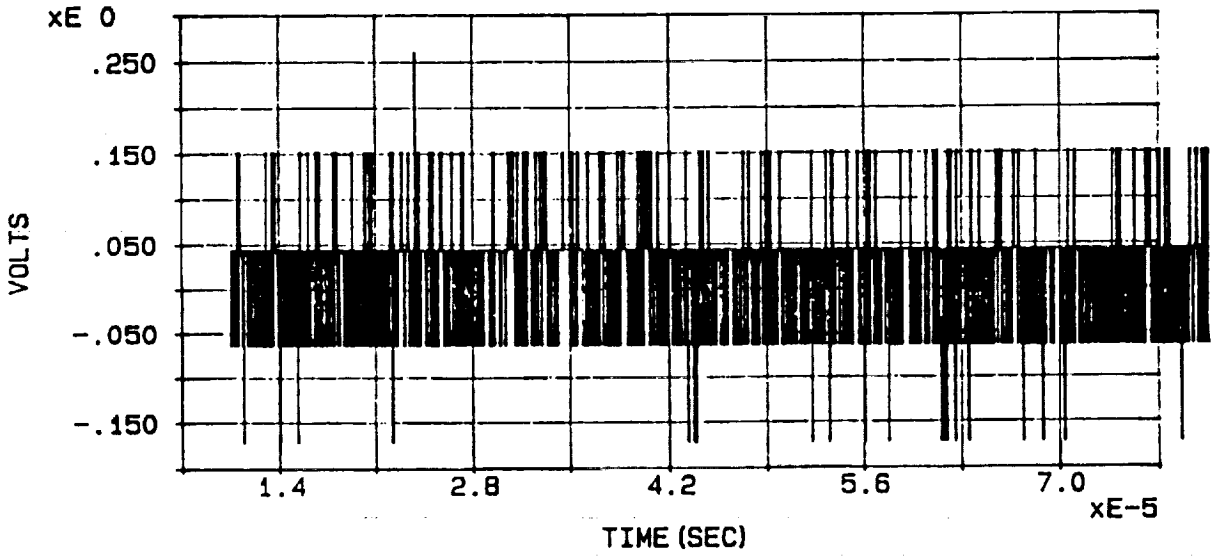

Figure 3.4.8B Peak Open Circuit Voltage = 0.2601 volts

Figure 3.4.8 Marx Injection Current (A) And Cable 10 Open Circuit Voltage (B) at Attachment Point 1 (Forward System Tunnel). External Bond Strap

Table 3.4.1

Marx Generator Test Shots for Cables 8 and 10 at Attach Point 1. Scaling Done to 200 kA, 10^{11} NASA Specification Injected Current

Cable Number	Bond Strap	Scaled I_{sc} (Amps)	Scaled V_{oc} (Volts)	Figure Numbers
8	INTERNAL	29	83	3.4.1, 3.4.2
8	EXTERNAL	0.32	3.0	3.4.3, 3.4.4
10	INTERNAL	8.2	9.6	3.4.5, 3.4.6
10	EXTERNAL	0.11	< 0.31	3.4.7, 3.4.8

Taking the ratios of external to internal bond strap cable response yields:

Cable 8	I_{sc}	0.32/29	=	0.011
Cable 8	V_{oc}	3.0/83	=	0.036
Cable 10	I_{sc}	0.11/8.2	=	0.013
Cable 10	V_{oc}	< 0.31/9.6	=	< 0.032

It is readily seen that the external bond straps provide a better than 20 factor of protection over internal bond straps for attachment to forward system tunnel (attach point 1). This is probably because the external bond strap allows the current to flow directly from the tunnel cover to the SRM case, and preventing the current from having to arc over apertures and thus inducing cable coupling through these apertures. The external bond straps were only used on the forward tunnel covers, so the large reduction of cable coupling due to the external bond straps indicates that, at least for attach point 1, the forward system tunnel apertures provide by far the greatest source of coupling. This is in agreement with the modeling as reported in Chapter 4, which concludes that the system tunnel seam and aperture coupling is dominant over DFI cable coupling into the system tunnel. The modeling was performed with the flight configuration internal bonding straps from the system tunnel floor to the SRM case.

3.5 Accuracy of Measurements

A concern has been raised that the pigtail used inside the measurement boxes to ground the cable shields may induce large voltages due to its (the pigtail's) inductance and the dI/dT of the electromagnetic environment.

The top of Figure 3.5.1 shows a shield penetrating into the measurement box, with a current I_p flowing on it and then through the pigtail. The bottom half of Figure 3.5.1 shows a nearby cable being measured, with a magnetic field B caused by I_p around its shield, with an area A of flux linkage between its shield and ground. The magnetic flux for this simple loop is

$$\Phi = \mu_o A \frac{I_p}{2\pi R} \tag{3.5.1}$$

where R is the distance between the top cable shield penetrating the box and the bottom cable being measured. We know from Faraday's induction law that the voltage induced by I_p on the cable being measured is just the time derivative of the flux, so

$$V = \frac{d\Phi}{dt} = \mu_o A \frac{\frac{dI_p}{dt}}{2\pi R} \tag{3.5.2}$$

Thiokol cables have no overall shields or backshell termination shield on entry into the measurement boxes, but the far, non-measurement end of the cable is open circuit which implies small currents. As for the USBI cables, all but cable 4 have overall shields with 360 degree backshell connectors on the measurement boxes. Cable 4 does have an EMI shield open on the far end, as do cables 7 and 11. The backshell connector should shield any large currents on overall shields from entry into the measurement boxes for most USBI cables, and the EMI shields on cables 4, 7 and 11 should have small currents on them because they are open on the far end. Therefore, only small currents should exist on cables penetrating the measurement boxes, so I_p is small.

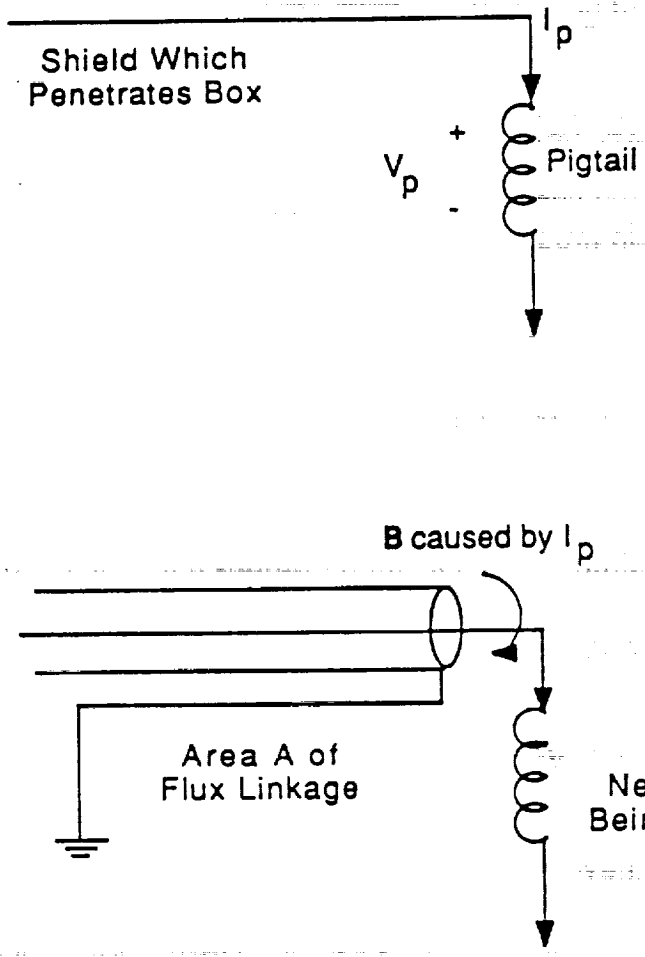

$$V = \frac{d\phi}{dt} = \mu_o A \frac{\frac{dI_p}{dt}}{2\pi R}$$

R = distance between cables

Figure 3.5.1 Mutual Coupling of Cables Within Measurement Boxes. Concern: Possible Measurement Error

The Marx generator shots have an injected current dI/dT on the order of 10^{11} amps/sec. If one assumes that dI_p/dT is at most less than a couple ten-thousandth's of the Marx's dI/dT (valid since I_p is small), and assuming R = 0.1 meters and A = 0.01 square meters, then Equation 3.5.2 above gives a voltage less than one volt. The voltages measured on the signal wires were typically much larger than one volt, so the conclusion is that no significant data contamination occurred.

CHAPTER 4

THE DEVELOPMENTAL FLIGHT INSTRUMENTATION CABLE AND SYSTEMS TUNNEL CABLE ANALYSES

4.1 Introduction

This chapter is devoted to the numerical modeling of a direct lightning strike to the solid rocket booster test object (SRB), and the coupling of electromagnetic energy to the developmental flight instrumentation (DFI) cables external to the systems tunnel and the cables within the systems tunnel. The injected lightning current waveform is the specification given in NASA Space Shuttle Program Lightning Protection Criteria Document JSC-07636 Revision D.

Analysis of the DFI cables which are exterior to the systems tunnel is presented in Section 4.2. This section is concerned with determining the open-circuit voltages and short-circuit currents of the DFI cables at the systems tunnel interface, and the current densities and normal electric fields at the surface of the SRB. These results are applied in Section 4.3 as the electromagnetic sources which couple energy to the cables within the systems tunnel through seam apertures and DFI cable penetration. This section also analyzes the effect of a sock shield in reducing coupling to a DFI cable, and the worst-case effect of the detachment point at the SRB nozzle compared to the experimental aft skirt ring detachment point.

Section 4.3 presents the analysis used to determine the coupling of electromagnetic energy to the cables within the systems tunnel. The analysis indicates that the surface current density on the systems tunnel coupling through the seam apertures of the tunnel is the dominant driver of the cables within the tunnel.

A summary of pertinent results and conclusions is provided in Section 4.4.

4.2 Developmental Flight Instrumentation Cable Analysis and Test Object Modeling

4.2.1 Introduction

The objective of the work documented in this section was to obtain information/data enabling an evaluation of the effects a worst-case lightning strike would present to the USBI cables located within the systems tunnel. The information required to perform such an evaluation are surface current densities and normal surface electric fields on the SRB test object. The current densities couple energy into the systems tunnel via seams and apertures. The electric fields in conjunction with the current densities drive the DFI cables exterior to the tunnel which couple energy directly to the interior via penetration. This section will be concerned with calculating the surface current densities and normal electric fields along with the open-circuit voltages and short-circuit currents on the DFI cables at the systems tunnel interface. These results will be used in Section 4.3 devoted to systems tunnel modeling, USBI cable analysis.

The worst-case lightning current waveform is given in Figure 4.2.1. This waveform contains the high dI/dt and the high current amplitude portions of the worst-case lightning first return stroke excerpted from the NASA Space Shuttle Program Lightning Protection Criteria Document, JSC-07636, Revision D. The waveform shown in Figure 4.2.1 rises to 200 kiloamperes in 2 microseconds yielding an average dI/dt of 10^{11} amperes/second with a maximum dI/dt of 2×10^{11} amperes/second.

The method of analyses utilized the three dimensional finite difference approach of solving Maxwell's equations (Appendix B) to inject the lightning current onto the test object and calculate the surface electric and magnetic fields. A weakly-coupled model implementing telegrapher's equations was then developed to couple the energy from the stored electric and magnetic fields onto the DFI cables. Open-circuit voltages and short-circuit currents were then calculated at the DFI cable/systems tunnel interface. The validity of this two-step approach was verified during the course of the analysis.

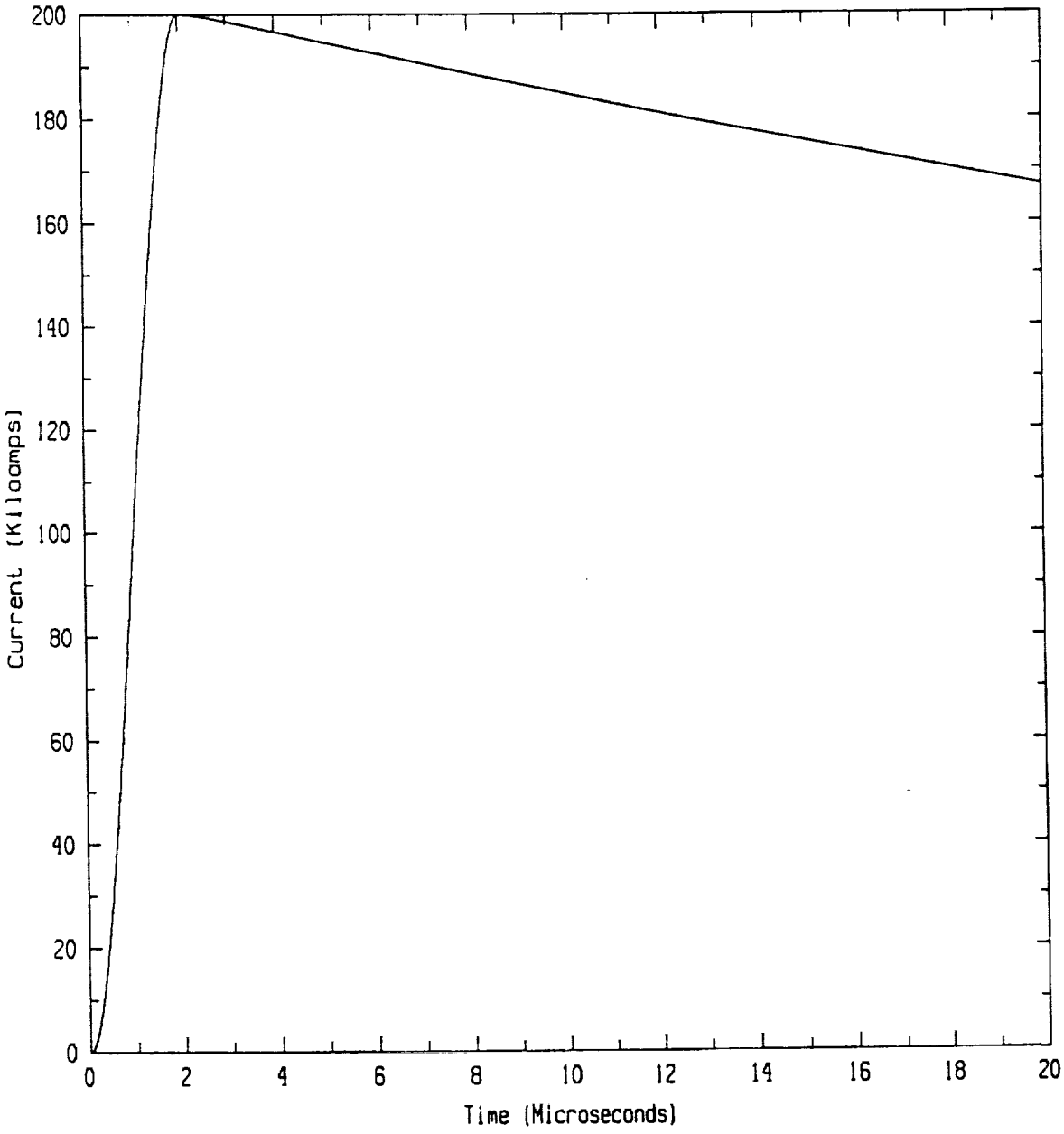

Figure 4.2.1 Worst-Case First Return Stroke Lightning Current Waveform

Information pertaining to the physical layout of the DFI cables on the test object is presented in Section 4.2.2. Modeling techniques utilized to obtain the required information is the subject of Section 4.2.3. The results of the modeling are discussed in Section 4.2.4.

4.2.2 DFI Cable Information

A drawing of the test object was provided in Figure 2.3. An illustration of the "unrolled" DFI cables is shown in Figure 4.2.2 where each individual cable within a particular bundle has been identified with a number for easy reference. For instance there are eight individual cables within the cable bundle located at station number 539.46. Information pertaining to the physical layout of the DFI cables is supplied in Table 4.2.1. This table contains eight columns. The first column lists the cable bundle test number and the corresponding TC (Thiokol Corporation) identification number (a seven character string beginning with "7U7"). The second column provides the station numbers where the cable bundles exit the systems tunnel and azimuthally traverse the test object. The third column lists the identification number given to the individual cables within each respective cable bundle.

The fourth column indicates whether an individual cable possesses an overall shield. There are a total of fifty-seven DFI cables on the test object. Seventeen of these cables possess an overall shield in addition to the instrumentation shield. This overall shield is termed a "sock shield". A typical physical representation of a DFI cable is shown in Figure 4.2.3. The cable exits the systems tunnel and traverses the test object azimuthally. The sock shield, if present, covers the cable from the systems tunnel to a point two to four inches from the sensor. The sock shield is circumferentially bonded to the systems tunnel and grounded to the test object at the opposite end. The DFI cable exits the sock shield and the instrumentation shield is terminated approximately one to two inches beyond. The lengths of the sock shield and the instrumentation shields are listed in columns five and six of Table 4.2.1 respectively. The terminated end of the instrumentation shield is left electrically floating. Typical cross-sectional views of the cable runs and the cork dams are shown in Figure 4.2.4.

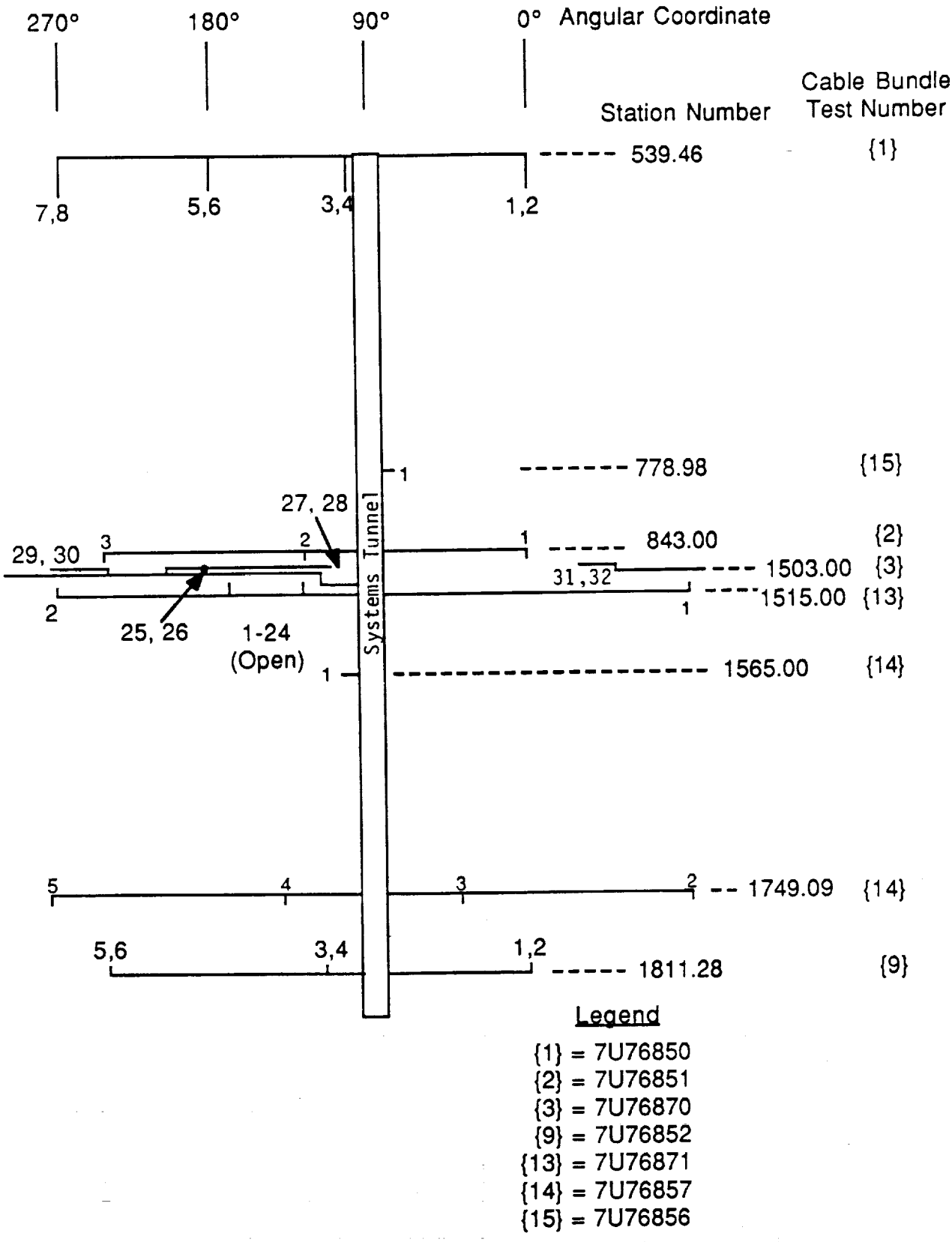

Figure 4.2.2 "Unrolled" DFI Cables with Identification Numbers

Table 4.2.1
DFI Cable Physical Layout Information

DFI Cable Bundle Number	DFI Cable Bundle Station Number	Individual DFI Cable Number	Sock Shield Present	Sock Shield Length (Inches)	Instrumentation Shield Length (Inches)	DFI Sensor Station Number	DFI Sensor Angular Location
{1} (7U76850)	539.46	1	Yes	127	128	556.50	0°
		2	Yes	127	128	556.50	0°
		3	Yes	21	22	556.50	98°
		4	Yes	21	22	556.50	98°
		5	Yes	127	128	556.50	180°
		6	Yes	127	128	556.50	180°
		7	Yes	243	244	556.50	270°
		8	Yes	243	244	556.50	270°
{15} (7U76856)	778.98	1	No	----	<4	778.98	90°
{2} (7U76851)	843.00	1	No	----	113	846.30	0°
		2	No	----	36	846.30	120°
		3	No	----	190	846.30	240°
{3} (7U76870)	Between 1501.00 and 1504.81	1	No	----	46	----	----
		2	No	----	46	----	----
		3	No	----	51	----	----
		4	No	----	51	----	----
		5	No	----	56	----	----
		6	No	----	56	----	----
		7	No	----	61	----	----
		8	No	----	61	----	----

Table 4.2.1 (Cont'd.)
DFI Cable Physical Layout Information

DFI Cable Bundle Number	DFI Cable Bundle Station Number	Individual DFI Cable Number	Sock Shield Present	Sock Shield Length (Inches)	Instrumentation Shield Length (Inches)	DFI Sensor Station Number	DFI Sensor Angular Location
{3} (7U76870) (Cont'd.)	Between 1501.00 and 1504.81	9	No	----	66	----	----
		10	No	----	66	----	----
		11	No	----	71	----	----
		12	No	----	71	----	----
		13	No	----	76	----	----
		14	No	----	76	----	----
		15	No	----	81	----	----
		16	No	----	81	----	----
		17	No	----	86	----	----
		18	No	----	86	----	----
		19	No	----	91	----	----
		20	No	----	91	----	----
		21	No	----	96	----	----
		22	No	----	96	----	----
		23	No	----	101	----	----
		24	No	----	101	----	----
		25	No	----	174	1501.00	180°
		26	No	----	174	1501.00	180°
		27	No	----	282	1501.00	98°
		28	No	----	282	1501.00	98°
		29	No	----	238	1501.00	270°
		30	No	----	238	1501.00	270°
		31	No	----	354	1501.00	0°
		32	No	----	354	1501.00	0°

Table 4.2.1 (Cont'd.)
DFI Cable Physical Layout Information

DFI Cable Bundle Number	DFI Cable Bundle Station Number	Individual DFI Cable Number	Sock Shield Present	Sock Shield Length (Inches)	Instrumentation Shield Length (Inches)	DFI Sensor Station Number	DFI Sensor Angular Location
{13} (7U76871)	1515.00	1	No	----	224	1511.00	274°
		2	Yes	222	224	1511.00	266°
{14} (7U76857)	1565.00	1	No	----	<4	1565.00	90°
	1749.09	2	No	----	228	1751.50	270°
	1749.09	3	No	----	59	1751.50	45°
	1749.09	4	Yes	57	59	1751.50	135°
	1749.09	5	Yes	226	228	1751.50	270°
{9} (7U76852)	1811.28	1	Yes	124	126	1797.00	0°
		2	Yes	124	126	1797.00	0°
		3	Yes	46	48	1797.00	120°
		4	Yes	46	48	1797.00	120°
		5	Yes	202	204	1797.00	240°
		6	Yes	202	204	1797.00	240°

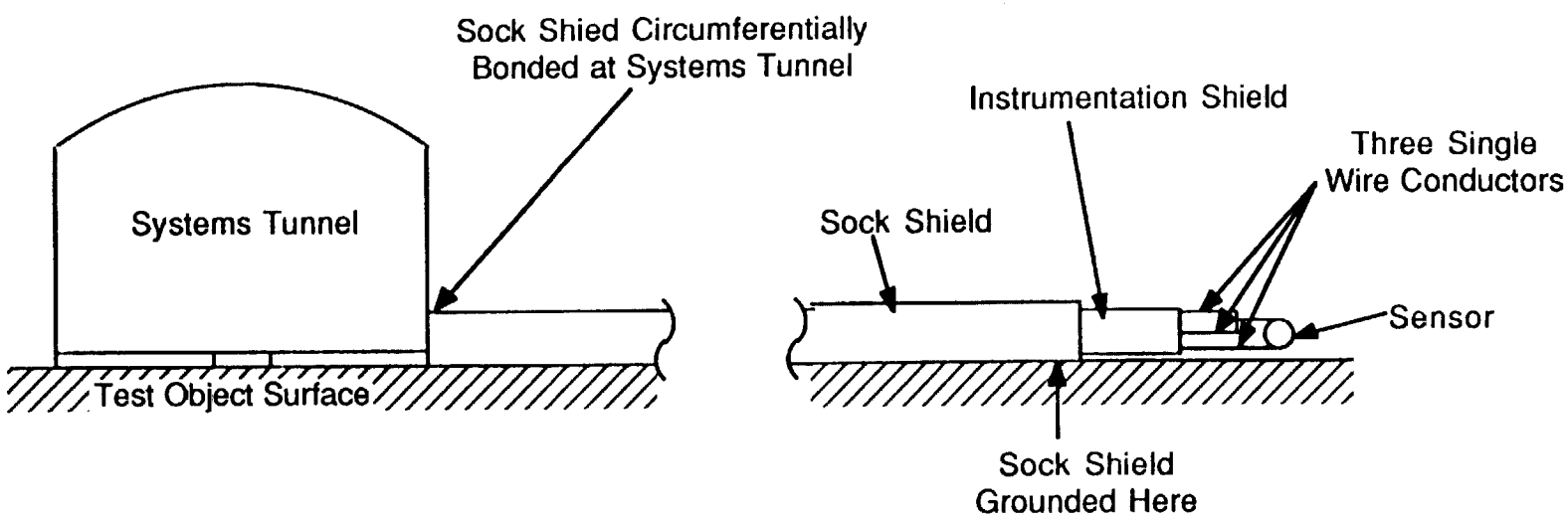

Figure 4.2.3 DFI Cable Physical Representation

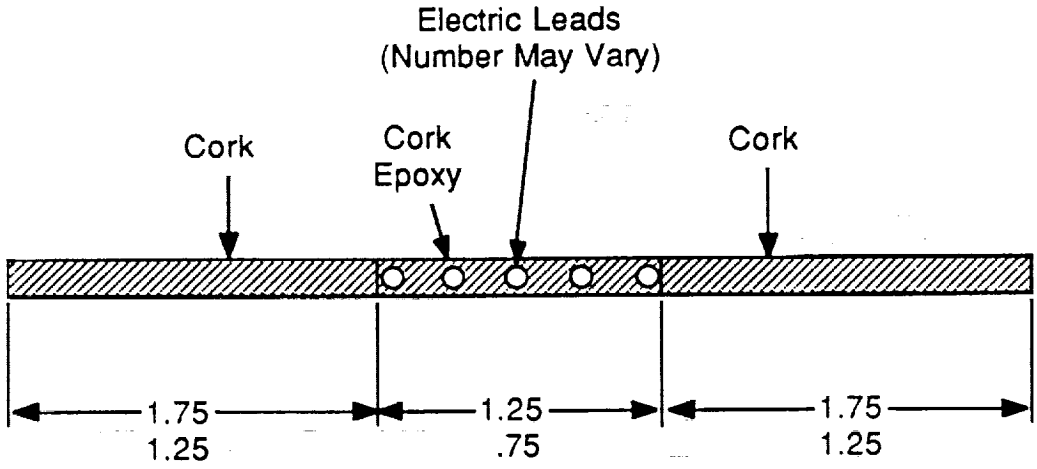

(A) Without Sock Shields

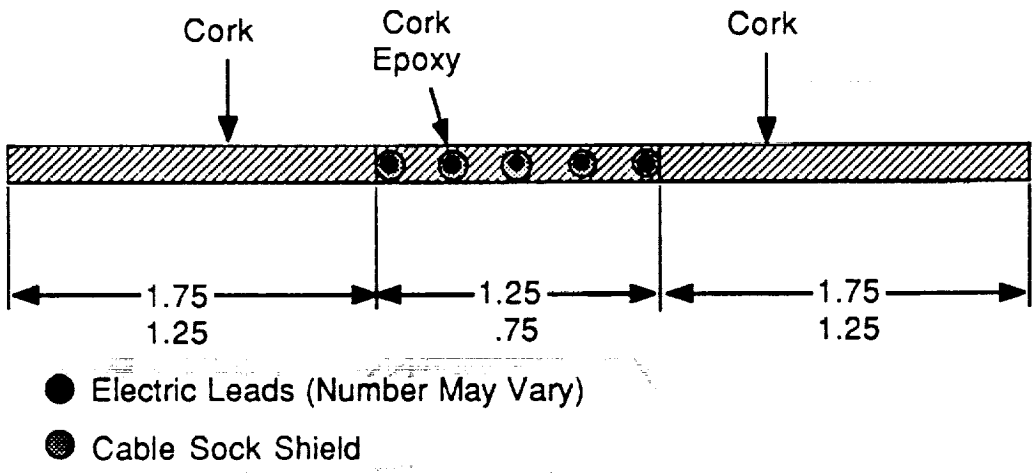

(B) With Sock Shields

Figure 4.2.4 Typical Cross-Sectional View of the Cable Runs and Cork Dams (All Dimensions are in Inches)

The DFI sensors are located approximately one to two inches beyond the instrumentation shield termination point. The station number and the angular coordinate (see Figure 4.2.2) of the sensors are provided in the seventh and eighth columns, respectively, of Table 4.2.1. A DFI cable thus exits the systems tunnel and traverses the test object azimuthally until reaching the angular location of the sensor. If the sensor is located at a different station number than the cable bundle, a right turn is instigated and the cable traverses axially to the sensor location.

To recapitulate, cable bundle number {1} (TC Number 7U76850) exits the systems tunnel at station number 539.46. There are a total of eight individual cables within this cable bundle. Each of these individual cables possess a sock shield. Individual cable 1 traverses the test object azimuthally to angular location 90°. It then bends 90° and traverses axially aftward 17.04 inches to the sensor at station number 556.50. Note that individual cables 1 through 24 of cable bundle {3} are left open, i.e. no sensors attached, and therefore the corresponding entry locations in columns seven and eight of Table 4.2.1 are left blank. Cable bundle {3} also exits the system tunnel further aftward than indicated in the table but quickly falls within the indicated bounds.

4.2.3 Modeling Techniques

The modeling technique used to determine open-circuit voltages and short-circuit currents at the DFI cable/systems tunnel interface consisted of a two-step process. The first step calculated the external surface electric and magnetic fields on the test object as a function of time due to a direct lightning strike. The second step utilized these fields to drive the DFI cables. This procedure enabled the use of a small grid to model cable behavior without imposing one on the whole test object which would result in extensive demands on computer memory and prohibitive computer runtimes.

The three dimensional finite difference technique of solving Maxwell's equations (Appendix B) was used to model the effects of a direct strike to the test object. The grid size was:

Δx = 1.0 meter,
Δy = 1.0 meter,
Δz = 1.0 meter, and
Δt = 1.8 nanoseconds,

in a problem space of dimension, 42 x 15 x 13, (x,y,z). The cubic meter grid enabled accurate calculations of electromagnetic phenomena containing frequency components up to 35 MHz. This is well-above the highest significant components in the lightning waveform of Figure 4.2.1.

The second modeling step utilized telegrapher's equations to determine the extent of EM coupling to the instrumentation shield of the DFI cables. The extended exposure lengths and smaller inductances associated with the instrumentation shields relegates the energy coupled to the sensor wires as insignificant in comparison. Telegrapher's equations are shown below:

$$\frac{dI(z,t)}{dt} + \frac{R}{L} I(z,t) = \frac{\mu h}{L} \frac{dH(z,t)}{dt} + \frac{1}{L} \frac{dV(z,t)}{dz} \qquad (4.1)$$

$$\frac{dV(z,t)}{dt} = \frac{L}{\mu\varepsilon} \frac{dI(z,t)}{dz} - h \frac{dE(z,t)}{dt} \qquad (4.2)$$

where:

- I is the outer cable shield current,
- V is the potential difference between the outer shield and the test object surface,
- R is the cable resistance per unit length,
- L is the cable inductance per unit length,
- h is the distance between the outer shield and the test object surface,
- ε, μ are the permittivity and permeability, respectively, of the intervening media between the cable and the test object surface,
- H is the magnetic field component perpendicular to the area created by the cables and the test object surface, and
- E is the test object surface normal electric field.

These equations were numerically implemented by the transformation into the finite differenced form given below:

$$\frac{I\left(z,\ t+\frac{1}{2}\Delta t\right) - I\left(z,\ t-\frac{1}{2}\Delta t\right)}{\Delta t} + \frac{R}{L}\ \frac{I\left(z,\ t+\frac{1}{2}\Delta t\right) + I\left(z,\ t-\frac{1}{2}\Delta t\right)}{2}$$

$$= \frac{\mu h}{L}\ \frac{H\left(z,\ t+\frac{1}{2}\Delta t\right) - H\left(z,\ t-\frac{1}{2}\Delta t\right)}{\Delta t}$$

$$+ \frac{1}{L}\ \frac{V\left(z+\frac{1}{2}\Delta z,t\right) - V\left(z-\frac{1}{2}\Delta z,t\right)}{\Delta z} \qquad (4.3)$$

$$\frac{V\left(z,\ t+\frac{1}{2}\Delta t\right) - V\left(z,\ t-\frac{1}{2}\Delta t\right)}{\Delta t} = \frac{L}{\mu\varepsilon}\ \frac{I\left(z+\frac{1}{2}\Delta z,t\right) - I\left(z-\frac{1}{2}\Delta z,t\right)}{\Delta z}$$

$$- h\ \frac{E\left(z,\ t+\frac{1}{2}\Delta t\right) - E\left(z,\ t-\frac{1}{2}\Delta t\right)}{\Delta t} \qquad (4.4)$$

where z is the spatial dimension along the cables. These equations require the selection of a Δz and a Δt. Such a selection is based upon levels of necessary accuracy, incorporating known uncertainties, and available computer resources. Combining these aspects the particular grid values selected were:

$$\Delta z = 2 \text{ inches, and}$$
$$\Delta t = 150 \text{ picoseconds.}$$

The electrical and some physical parameters associated with the DFI cables are listed in Table 4.2.2. The medium in which the cables are immersed was issued a relative dielectric constant of 3 to simulate the surrounding cork dams and epoxy. The characteristic inductances of the cables are 43 nanohenrys/meter for segments possessing sock shields and 137 nanohenrys/meter otherwise.

The boundary conditions imposed on the cables are portrayed in Figure 4.2.5. These conditions were selected to model the floating end of the instrumentation shields. When sock shields are employed the cables are driven by the respective unshielded segments only.

TABLE 4.2.2
DFI CABLE PHYSICAL AND ELECTRICAL PARAMETERS

CABLE PARAMETER	VALUE
Cable Resistance, R	0
Cable Radius, r	66 mils
Distance Above the SRM, h	16 mils
Inner Radius of Sock Shield, b	82 mils
Permittivity of Medium, ε	$3\varepsilon o$(1)
Permeability of Medium, μ	μo(2)
Characteristic Inductances:	
Segment Without Sock Shield L_1(3)	$137 \frac{nH}{m}$
Segment With Sock Shield L_2(4)	$43 \frac{nH}{m}$

(1) ε_o = 8.854 E-12 Farads/meter

(2) μ_o = 1.26 E-6 Henrys/meter

(3) $L_1 = \frac{\mu}{2\pi} \cosh^{-1} \frac{h+r}{r}$

(4) $L_2 = \frac{\mu}{2\pi} \ln \frac{b}{r}$

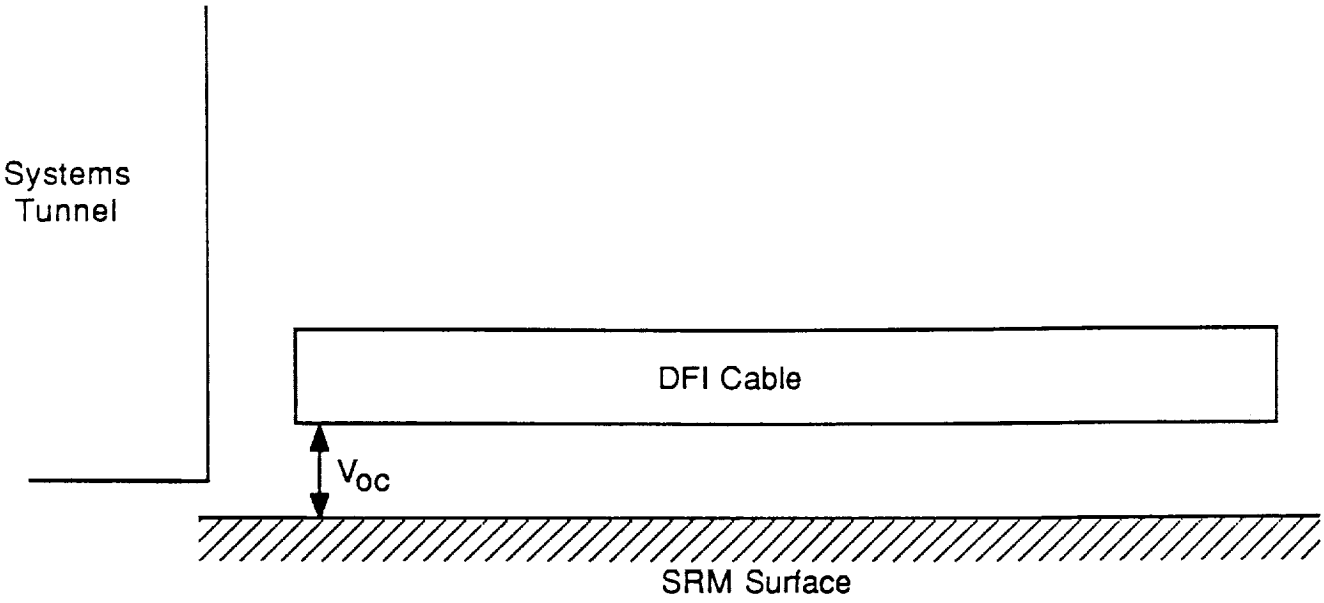

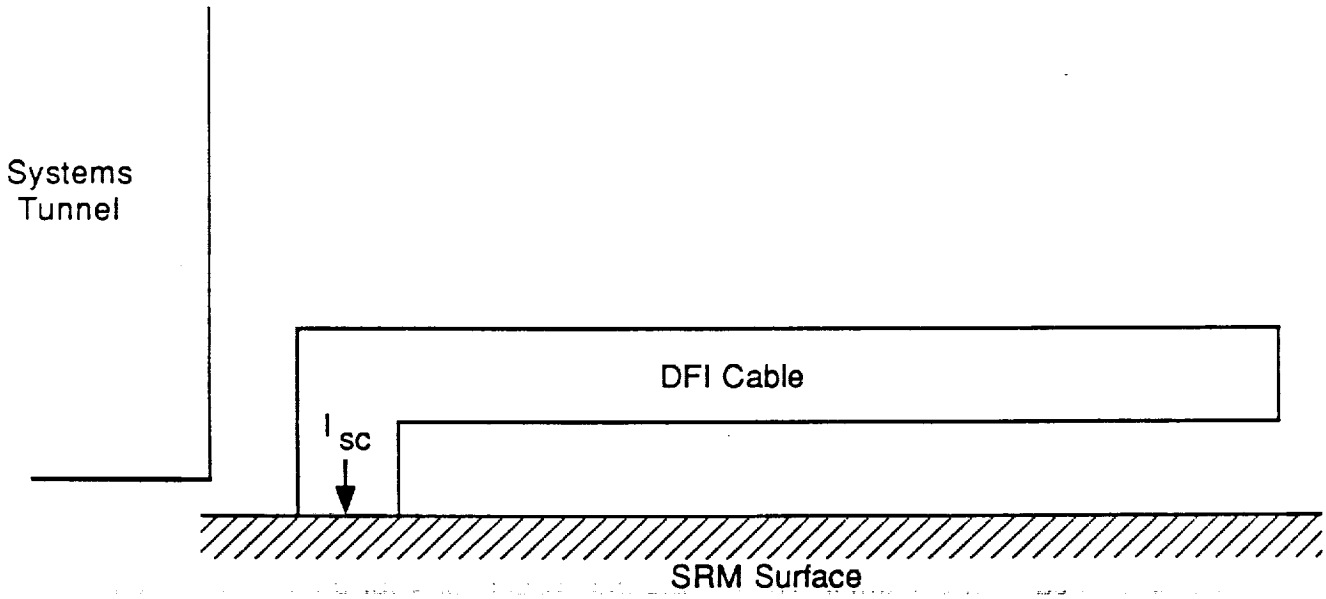

Figure 4.2.5 Open-Circuit Voltage and Short-Circuit Current Models Illustrating the Boundary Conditions

4.2.4 Modeling Results and Analysis

This section discussed the results that were obtained by implementing the modeling procedures described in the previous section. The attachment and detachment points are shown in Figure 4.2.6. The attachment point corresponds to experimental attachment point #1. Detachment point #1 corresponds to the point used during the lightning simulation tests. Detachment point #2 is a more likely representative of an actual flight configuration lightning interaction event and was selected for comparison purposes. Only one attachment point was investigated due to the relative insignificance of the DFI cables, as USBI cable drivers, when compared with the results due to systems tunnel, seam and aperture coupling (see Section 4.3).

The distribution of peak surface current density values on the test object for detachment point #1 are presented linearly and logarithmically, in an "unrolled" fashion, in Figure 4.2.7 and Figure 4.2.8 respectively. The linear and logarithmic plots for detachment point #2 are shown in Figure 4.2.9 and Figure 4.2.10 respectively. In these figures the systems tunnel runs vertically down the center at an angular coordinate of 90°. The vertical line of arrows at either side (at -90° and at 270°) are identical because the test object was unrolled and overlapped to present symmetric figures. The blank points at 875 and at 500 inches along the length of the test object and at -90° and 270° correspond to the forward and the aft struts. These struts connect the test object to the ET simulation structure. Examination of Figures 4.2.7 and 4.2.9 reveal greater densities of current below 500 inches than above. This line corresponds to the aft segment/forward segment junction. The difference in current densities is a consequence of the ET simulation structure which diverts a large portion of the current from the forward segment. The surface current density waveforms mirror the injected lightning waveform in Figure 4.2.1 with a superimposed oscillation attributable to test object resonance. A typical example is plotted in Figure 4.2.11.

The peak open-circuit voltage and short-circuit current values for each individual DFI cable are listed in Table 4.2.3 and Table 4.2.4 for detachment point #1 and #2, respectively. Examination of these tables reveal detachment point #2 to render a more severe cable environment. Voltages and currents are approximately five to ten percent higher than those for point #1. The maximum voltage value for point #2 is 970 volts on cable 1 of cable bundle {15}. The maximum current value is 1.1 amperes on cables 27 and 28 of bundle {3}. Inspection of either table reveal current

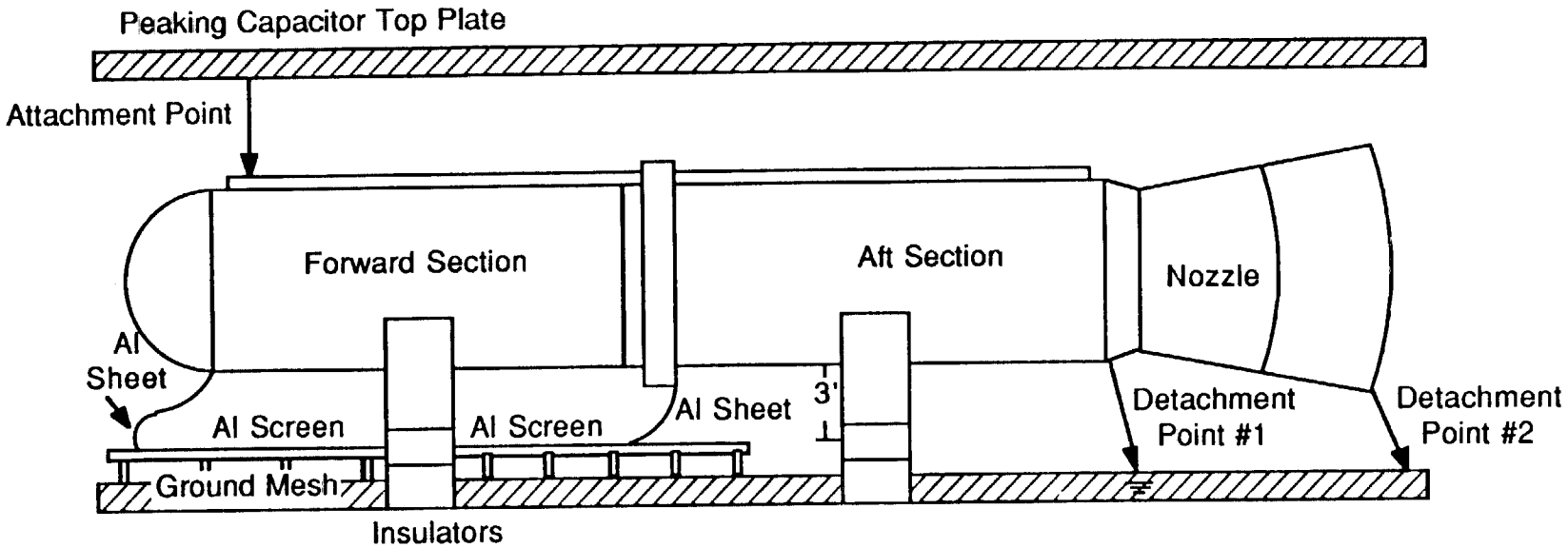

Figure 4.2.6 Test Object Showing Lightning Attachment and Detachment Points

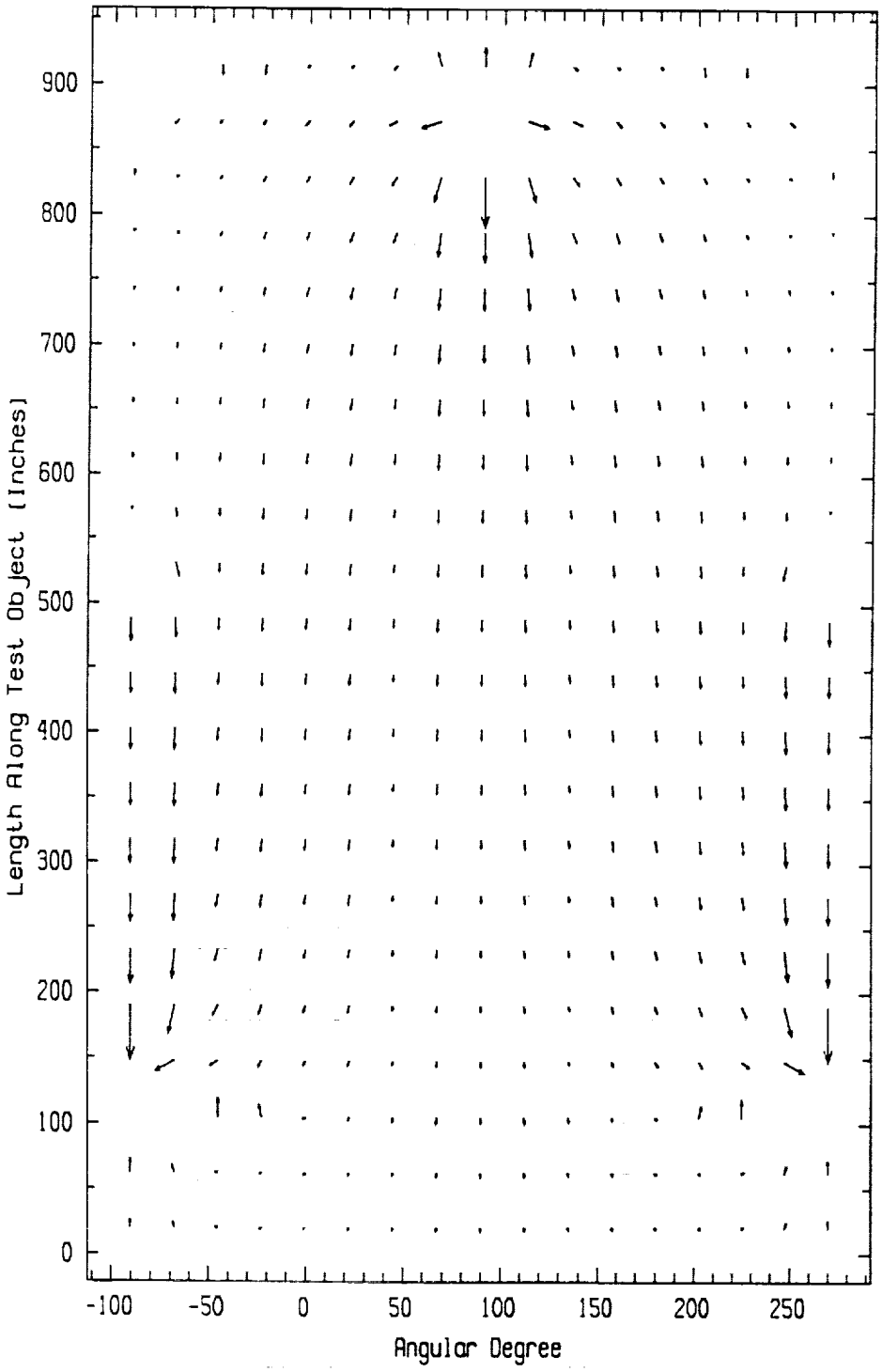

Figure 4.2.7 Current Density Vectors Over the Surface of the Test Object for a Lightning Attachment to the Front End of the Systems Tunnel and a Detachment at Point #1. The Maximum Arrow Length Corresponds to an Amplitude of 80.2 Kiloamperes/Meter

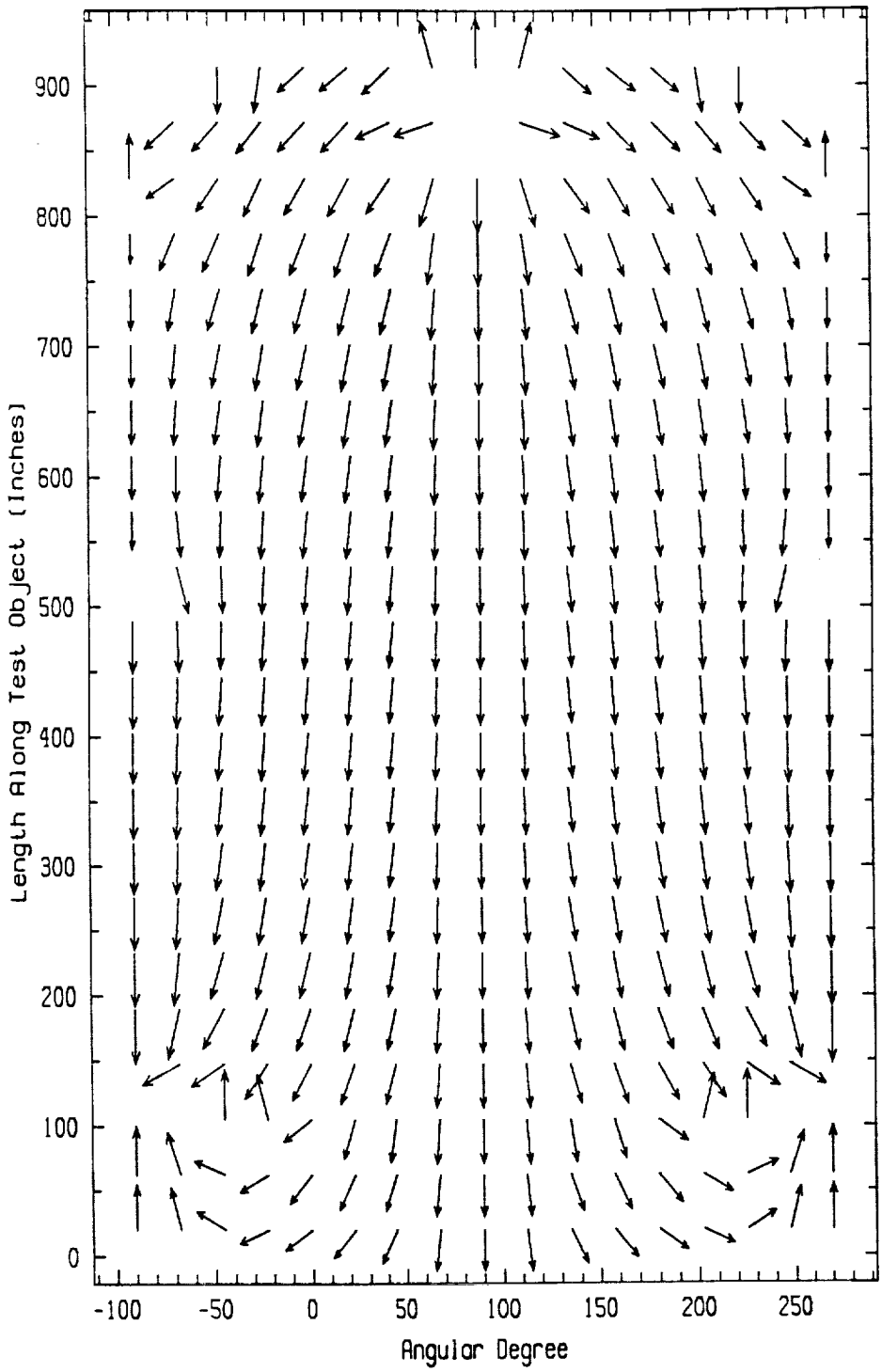

Figure 4.2.8 Current Density Vectors Over the Surface of the Test Object for a Lightning Attachment to the Front End of the Systems Tunnel and a Detachment at Point #1. The Arrow Lengths are Scaled Logarithmically

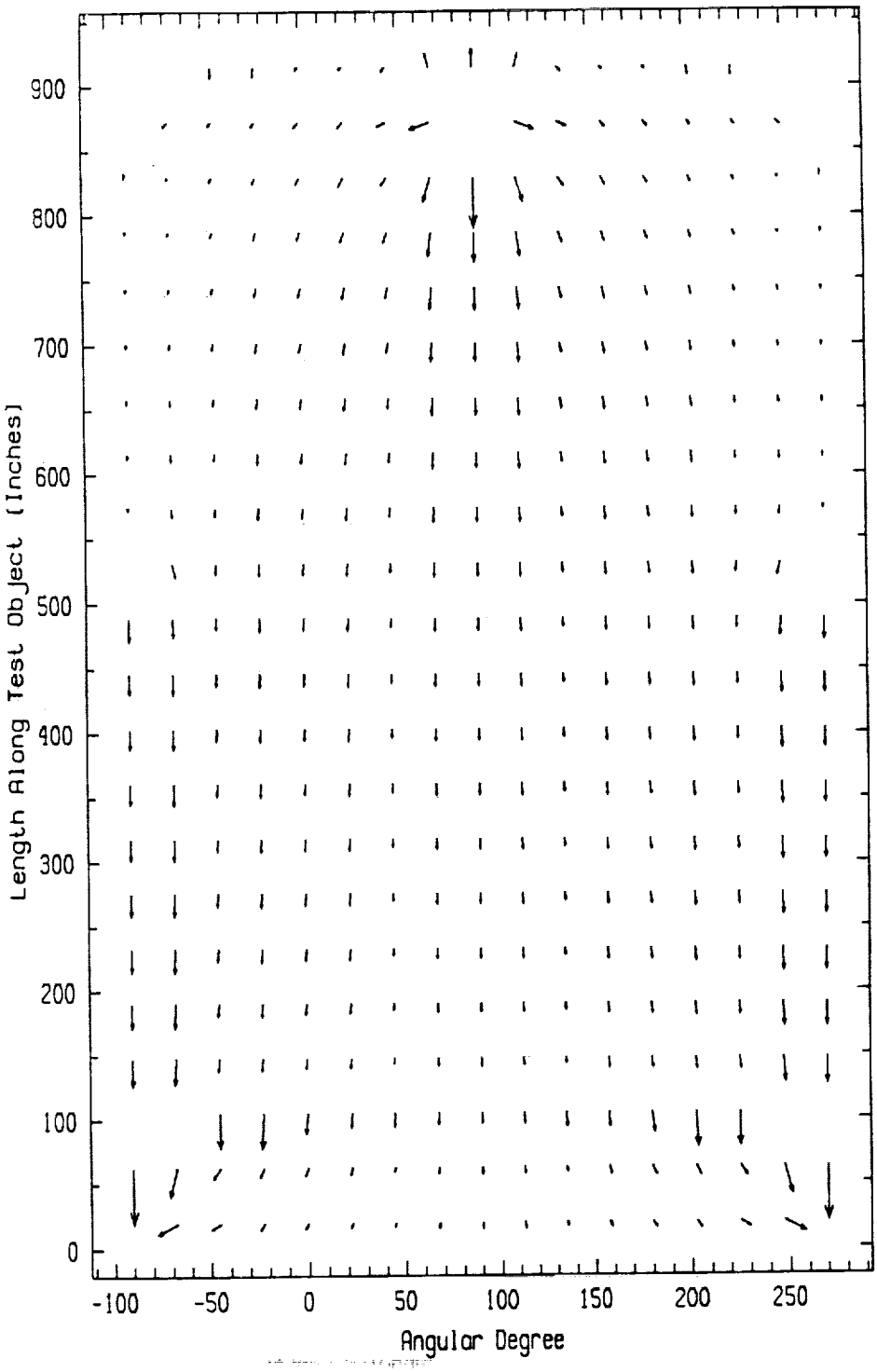

Figure 4.2.9 Current Density Vectors Over the Surface of the Test Object for a Lightning Attachment to the Front End of the Systems Tunnel and a Detachment at Point #2. The Maximum Arrow Length Corresponds to an Amplitude of 79.6 Kiloamperes/Meter

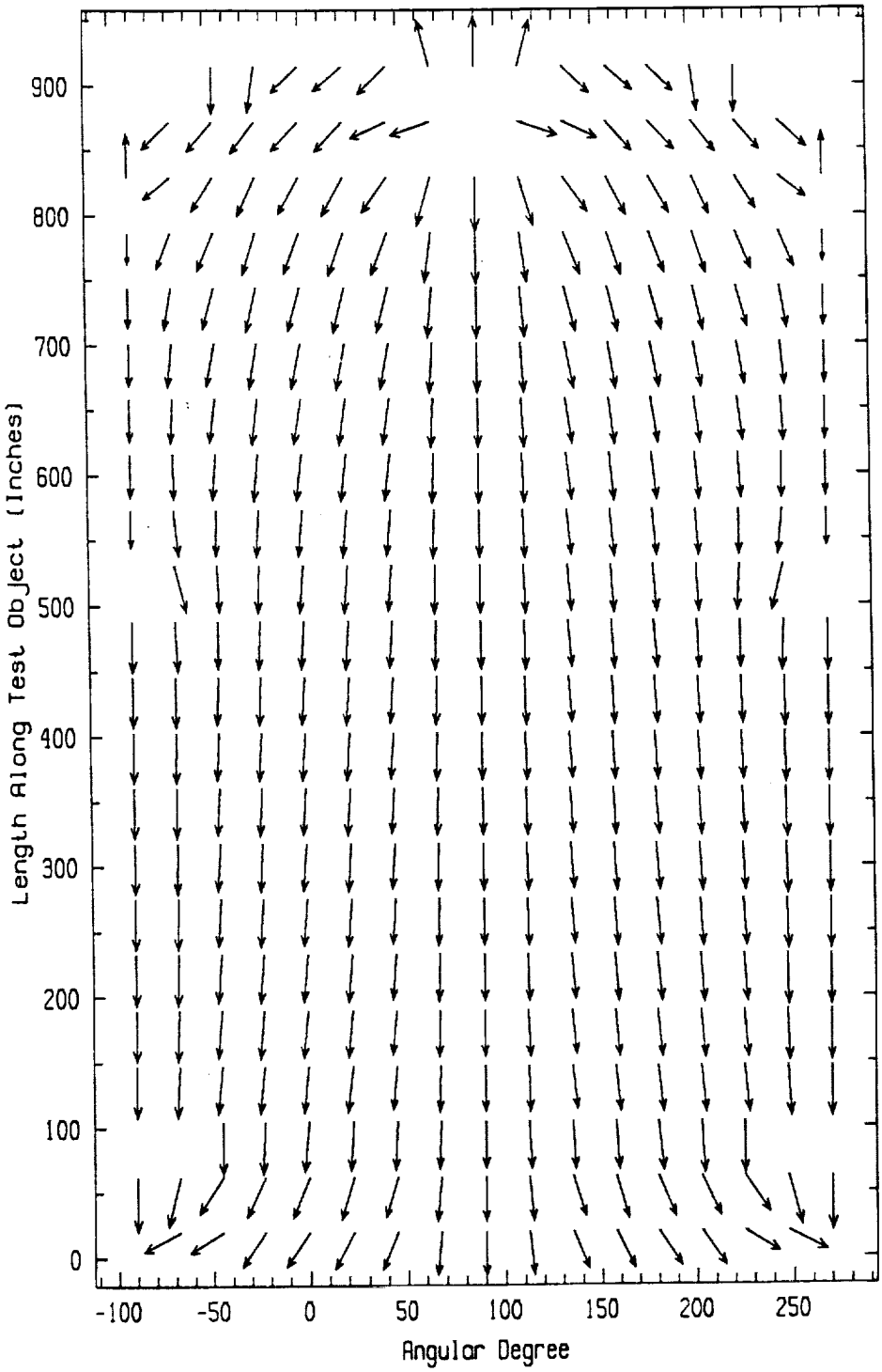

Figure 4.2.10 Current Density Vectors Over the Surface of the Test Object for a Lightning Attachment to the Front End of the Systems Tunnel and a Detachment at Point #2. The Arrow Lengths are Scaled Logarithmically

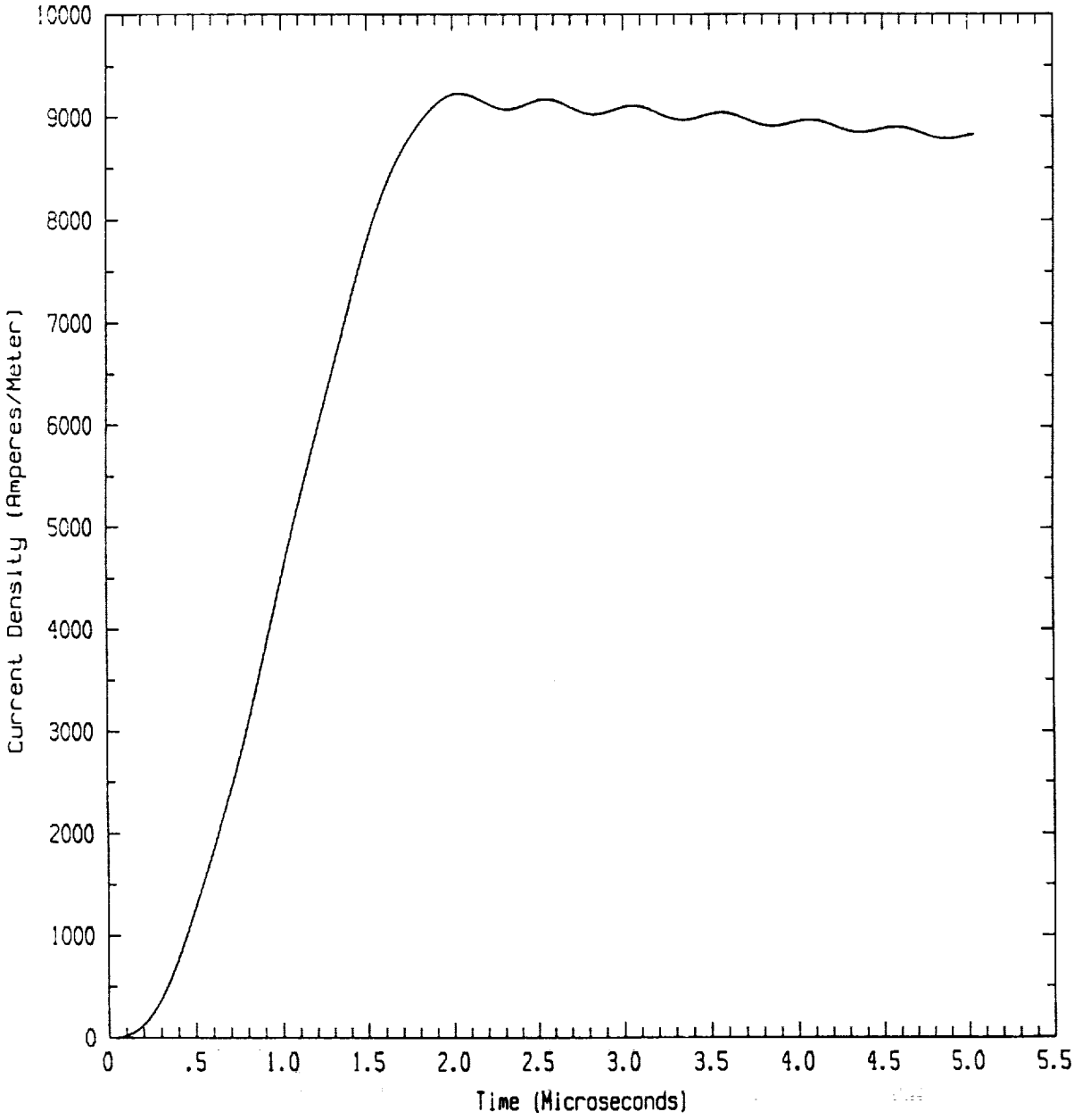

Figure 4.2.11 Typical Test Object Surface Current Density

C-2

Table 4.2.3
Peak Open-Circuit Voltages, Short-Circuit Currents, and Thevenin Equivalent Capacitive Values for Detachment Point #1

DFI Cable Bundle Number	Individual DFI Cable Number	Peak Open-Circuit Voltage Value (Volts)	Peak Short-Circuit Current Value (milliamperes)	Thevenin Equivalent Capacitive Value (Nanofarads)
	1	2.2	8.5	2.4
	2	2.2	8.5	2.4
	3	77	28	0.38
{1}	4	77	28	0.38
(7U76850)	5	2.2	8.5	2.4
	6	2.2	8.5	2.4
	7	0.002	0.49	----
	8	0.002	0.49	----
{15} (7U76856)	1	960	13	0.013
{2}	1	470	390	0.69
(7U76851)	2	670	140	0.19
	3	330	540	1.2
	1	550	170	0.28
	2	550	170	0.28
	3	550	190	0.30
{3}	4	550	190	0.30
(7U76870)	5	540	210	0.34
	6	540	210	0.34
	7	540	230	0.36
	8	540	230	0.36
	9	540	250	0.40
	10	540	250	0.40
	11	530	260	0.42
	12	530	260	0.42
	13	510	270	0.46

Table 4.2.3 (Cont'd.)
Peak Open-Circuit Voltages, Short-Circuit Currents, and Thevenin Equivalent Capacitive Values for Detachment Point #1

DFI Cable Bundle Number	Individual DFI Cable Number	Peak Open-Circuit Voltage Value (Volts)	Peak Short-Circuit Current Value (milliamperes)	Thevenin Equivalent Capacitive Value (Nanofarads)
	14	510	270	0.46
	15	500	280	0.49
	16	500	280	0.49
	17	480	300	0.52
	18	480	300	0.52
	19	470	310	0.55
{3}	20	470	310	0.55
(7U76870)	21	460	330	0.59
(Continued)	22	460	330	0.59
	23	460	340	0.61
	24	460	340	0.61
	25	340	520	1.1
	26	340	520	1.1
	27	360	880	1.8
	28	360	880	1.8
	29	260	600	1.5
	30	260	600	1.5
	31	210	820	2.2
	32	210	820	2.2
{13}	1	260	560	1.4
(7U76871)	2	0.0055	0.13	----
	1	580	8.8	0.012
{14}	2	150	430	1.4
(7U76857)	3	260	130	0.31
	4	3.4	5.1	0.93
	5	0.25	3.6	4.2

Table 4.2.3 (Cont'd.)
Peak Open-Circuit Voltages, Short-Circuit Currents, and Thevenin Equivalent Capacitive Values for Detachment Point #1

DFI Cable Bundle Number	Individual DFI Cable Number	Peak Open-Circuit Voltage Value (Volts)	Peak Short-Circuit Current Value (milliamperes)	Thevenin Equivalent Capacitive Value (Nanofarads)
	1	0.63	3.5	----
	2	0.63	3.5	----
{9}	3	3.0	4.9	0.87
(7U76852)	4	3.0	4.9	0.87
	5	0.17	1.8	3.0
	6	0.17	1.8	3.0

Table 4.2.4
Peak Open-Circuit Voltages, Short-Circuit Currents, and Thevenin Equivalent Capacitive Values for Detachment Point #2

DFI Cable Bundle Number	Individual DFI Cable Number	Peak Open-Circuit Voltage Value (Volts)	Peak Short-Circuit Current Value (milliamperes)	Thevenin Equivalent Capacitive Value (Nanofarads)
	1	2.4	10	2.4
	2	2.4	10	2.4
	3	77	29	0.38
{1}	4	77	29	0.38
(7U76850)	5	2.4	10	2.4
	6	2.4	10	2.4
	7	0.004	0.66	----
	8	0.004	0.66	----
{15} (7U76856)	1	970	14	0.013
{2}	1	500	440	0.69
(7U76851)	2	690	140	0.19
	3	360	650	1.2
	1	580	190	0.28
	2	580	190	0.28
	3	580	210	0.30
{3}	4	580	210	0.30
(7U76870)	5	570	230	0.34
	6	570	230	0.34
	7	570	250	0.36
	8	570	250	0.36
	9	570	280	0.40
	10	570	280	0.40
	11	550	290	0.42
	12	550	290	0.42
	13	540	310	0.46

Table 4.2.4 (Cont'd.)
Peak Open-Circuit Voltages, Short-Circuit Currents, and Thevenin Equivalent Capacitive Values for Detachment Point #2

DFI Cable Bundle Number	Individual DFI Cable Number	Peak Open-Circuit Voltage Value (Volts)	Peak Short-Circuit Current Value (milliamperes)	Thevenin Equivalent Capacitive Value (Nanofarads)
	14	540	310	0.46
	15	530	320	0.49
	16	530	320	0.49
	17	510	340	0.52
	18	510	340	0.52
	19	510	350	0.55
{3}	20	510	350	0.55
(7U76870)	21	490	370	0.59
(Continued)	22	490	370	0.59
	23	490	390	0.61
	24	490	390	0.61
	25	370	630	1.1
	26	370	630	1.1
	27	390	1100	1.8
	28	390	1100	1.8
	29	290	730	1.5
	30	290	730	1.5
	31	230	940	2.2
	32	230	940	2.2
{13}	1	290	670	1.4
(7U76871)	2	0.014	0.14	----
	1	610	9.6	0.013
{14}	2	180	620	1.4
(7U76857)	3	280	150	0.31
	4	3.6	5.9	0.93
	5	0.45	7.0	4.3

Table 4.2.4 (Cont'd.)
Peak Open-Circuit Voltages, Short-Circuit Currents, and Thevenin Equivalent Capacitive Values for Detachment Point #2

DFI Cable Bundle Number	Individual DFI Cable Number	Peak Open-Circuit Voltage Value (Volts)	Peak Short-Circuit Current Value (milliamperes)	Thevenin Equivalent Capacitive Value (Nanofarads)
	1	0.77	4.7	----
	2	0.77	4.7	----
{9}	3	3.2	9.0	0.91
(7U76852)	4	3.2	9.0	0.91
	5	0.36	4.7	3.6
	6	0.36	4.7	3.6

and voltage values on unshielded cables to greatly exceed those on cables possessing shields. In addition, the longer the sock shield length the smaller the voltages and currents. This is due to the increase of cable impedance associated with longer shielded cables.

The open-circuit voltage waveforms are, for the most part, proportional to the derivative of the test object surface current densities or proportional to the normal electric fields. Only when sock shields are employed, yielding voltage waveforms that are small and dominated by oscillations, do significant differences occur. The voltage on cable 2 of bundle {14} associated with detachment point #2 is plotted in Figure 4.2.12. The corresponding voltage on cable 5 within the same bundle is plotted in Figure 4.2.13. These two cables are symmetrically located on the test object about the attachment point and about the two detachment points. Cable 2 does not employ a sock shield while cable 5 does. Comparisons between these cables should thus provide an adequate evaluation of the effects of using sock shields. Examination of Figures 4.2.12 and 4.2.13 reveal a decrease in voltage by 52 dB when utilizing a sock shield. Cables 3 and 4 of bundle {14} and cables 1 and 2 of bundle {13} also provide a similar type scenario for comparisons. Analysis of the peak voltage values from the unshielded cable 3 to the shielded cable 4 reveal a 38 dB reduction. For cables 1 and 2 the reduction is 88 dB. For detachment point #1 the reductions are 56 dB, 38 dB, and 93 dB respectively.

The short-circuit currents are, for the most part, proportional to the derivatives of the corresponding open-circuit voltages with a superimposed oscillation equal to four times the DFI cable length. The short-circuit current for detachment point #2 associated with cable 2 of bundle {14} is plotted in Figure 4.2.14. The current for cable 5 of bundle {14} is plotted in Figure 4.2.15. Comparisons between these cables reveal a 39 dB reduction when utilizing a sock shield. Comparisons between cables 3 and 4 of bundle {14} and cables 1 and 2 of bundle {13} show a 28 dB and a 74 dB reduction respectively. For detachment point #1 the reductions are 41 dB, 28 dB, and 73 dB respectively.

To drive the DFI cables that are inside the systems tunnel requires an equivalent circuit to simulate the behavior of the exterior cable portion. Since the short-circuit currents are primarily proportional to the derivative of the corresponding

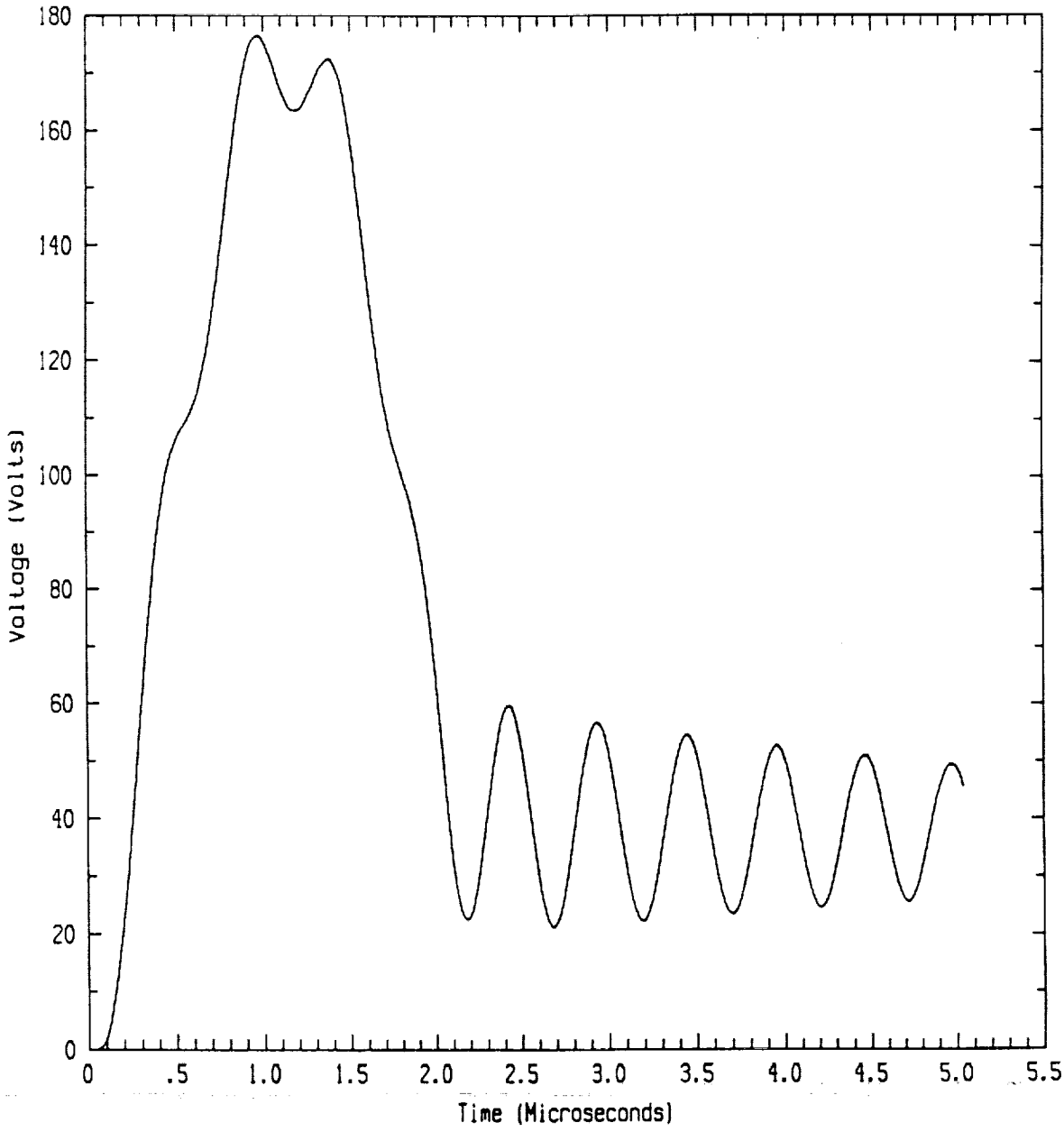

Figure 4.2.12 Open Circuit Voltage on Cable 2 of Cable Bundle {14} for Detachment Point #2

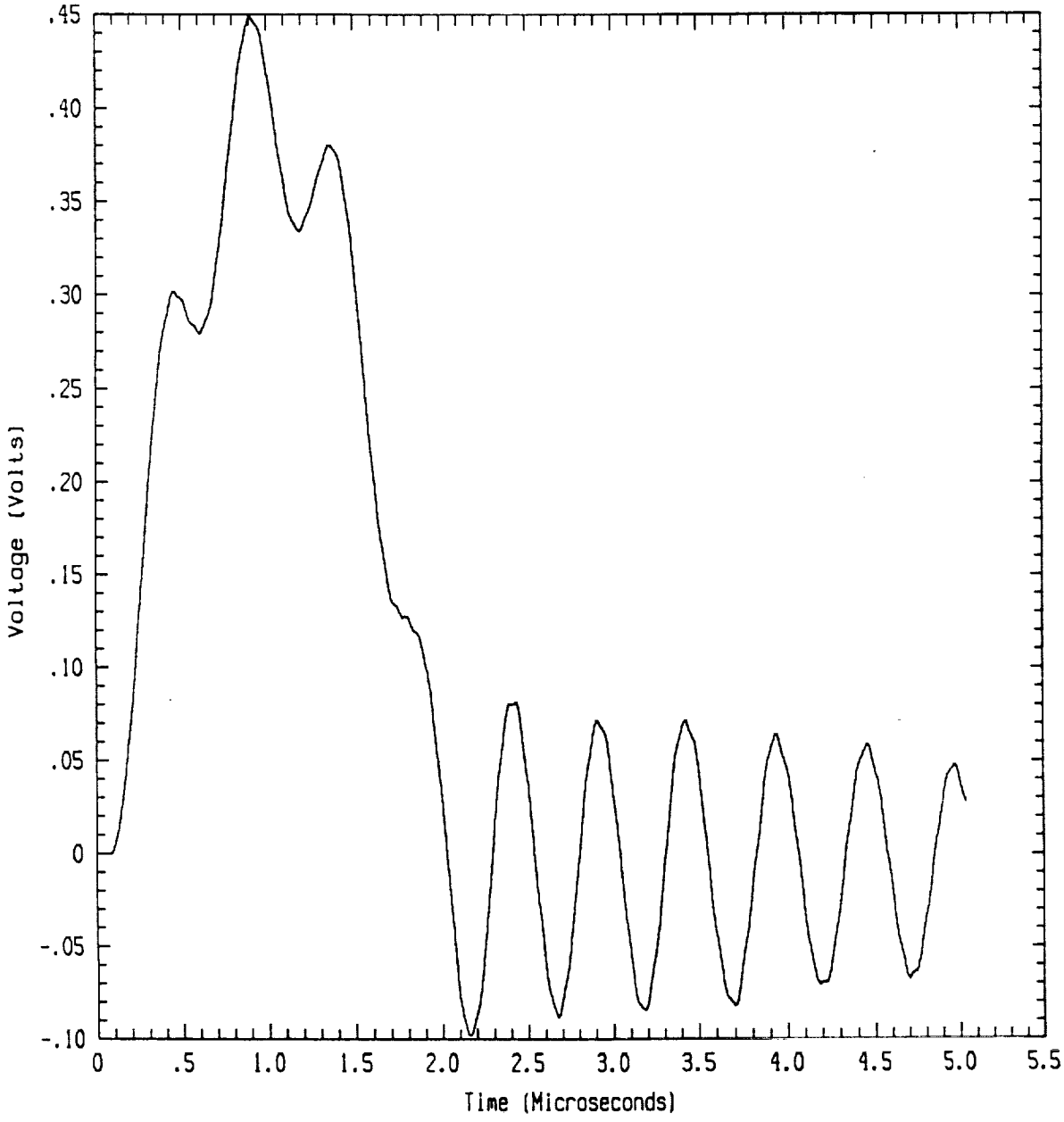

Figure 4.2.13 Open Circuit Voltage on Cable 5 of Cable Bundle {14} for Detachment Point #2

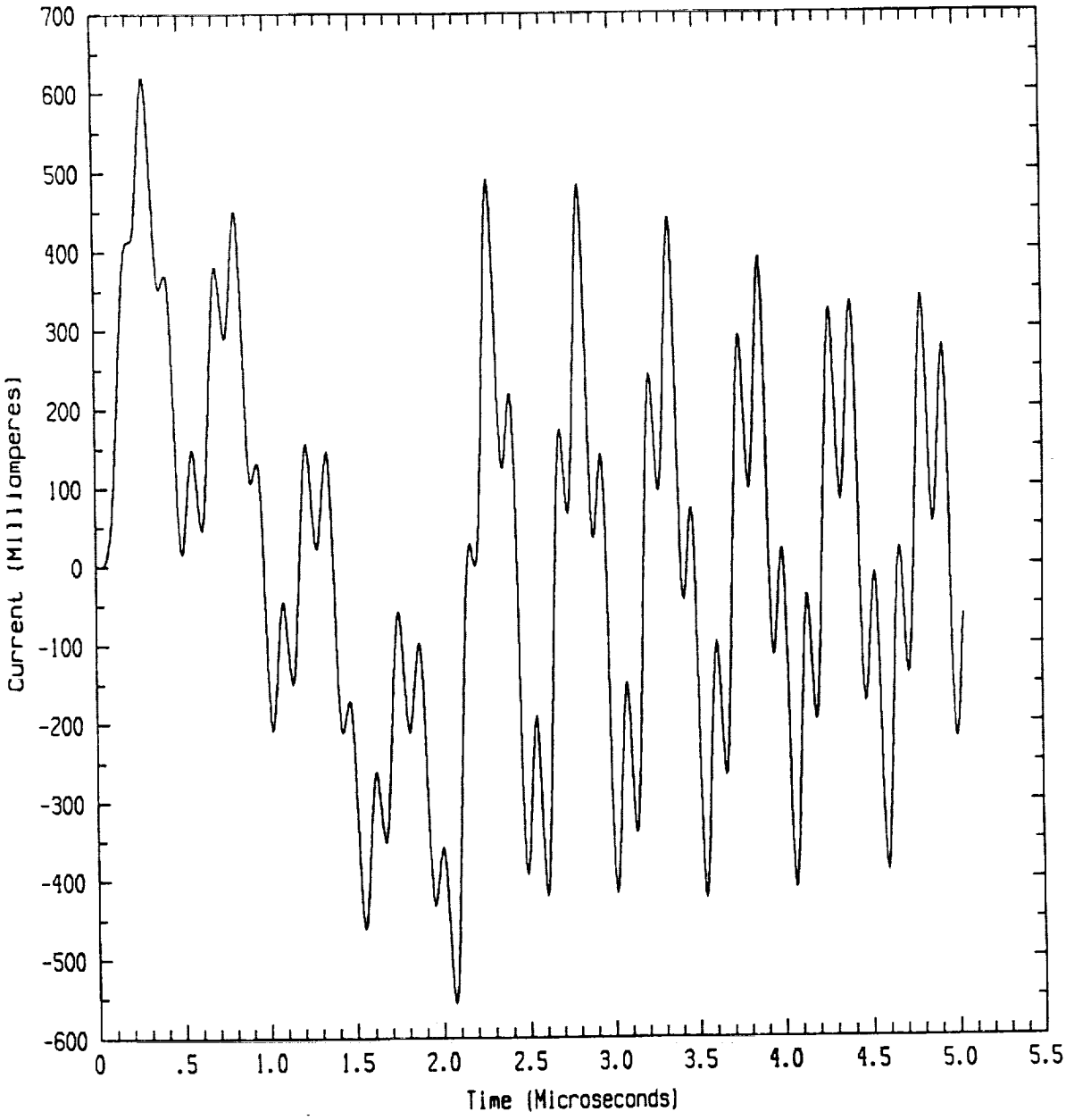

Figure 4.2.14 **Short Circuit Current on Cable 2 of Cable Bundle {14} for Detachment Point #2**

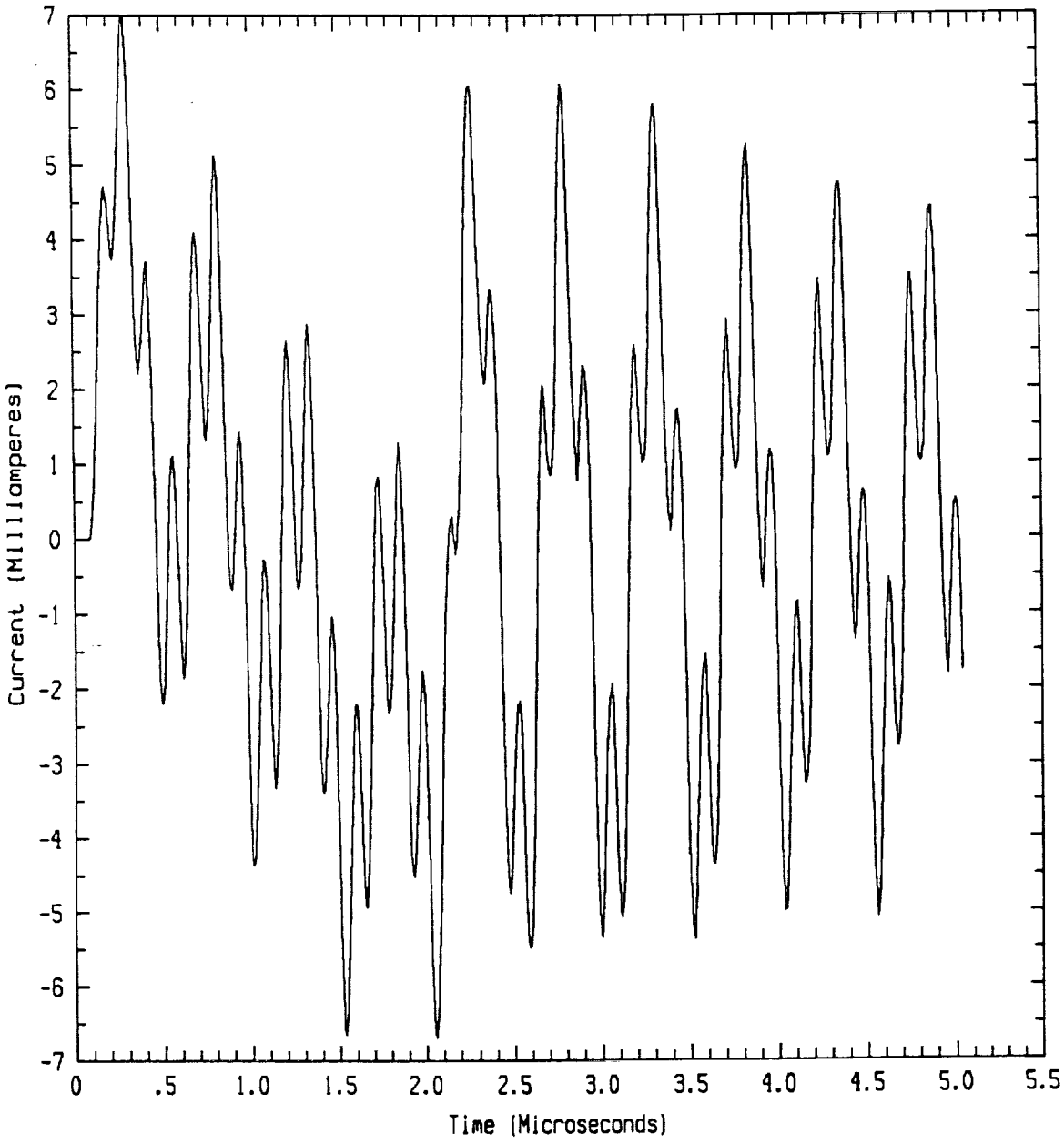

Figure 4.2.15 **Short Circuit Current on Cable 5 of Cable Bundle {14} for Detachment Point #2**

open-circuit voltages, a Thevenin equivalent circuit need only employ a capacitive element. This behavior is described by Equation (4.5):

$$V_{oc} = \frac{1}{C} \int I_{sc}\, dt \qquad (4.5)$$

where V_{oc} is the open-circuit voltage, I_{sc} is the short-circuit current, and C is the Thevenin equivalent capacitive element.

The capacitive values required to solve Equation (4.5) for each individual DFI cable are listed in the last column of Tables 4.2.3 and 4.2.4. The values between tables are identical as expected. For cases when sock shields are not employed the capacitive values listed solve Equation (4.5) exactly. For cables possessing sock shields the capacitive solutions are fair to poor. The longer the shield lengths the worse the solution. For poor cases the column entries were left blank. To properly characterize the actual voltage/current relationships for these cables would require other circuit elements resulting in a more complex equation. However, for these particular shielded cables the voltages and currents are insignificant when compared with those on unshielded cables.

The validity of the weakly-coupled model utilized in the above analysis can be verified by comparing the magnetic fields produced by the currents on the various DFI cables to those driving the model. Examination of Table 4.2.4 reveals a maximum short-circuit current of 1.1 amperes. This current value results in a peak magnetic field at the surface of the DFI cable instrumentation shield of approximately 100 amperes/m. This value is approximately 40 dB to 50 dB below the driving fields existent over most of the test object surface. The driving fields thus completely overwhelm any fields produced by current on the DFI cables thus proving the validity of the weakly-coupled model.

4.3 Systems Tunnel Cable Analysis

4.3.1 Introduction

The systems tunnel analysis is divided into two parts: a multiconductor cable analysis and a single conductor cable analysis. The objective of the multiconductor cable analysis is to determine whether the coupling from excited DFI cables which penetrate the systems tunnel or the coupling through the seam apertures created by the tunnel covers is the dominant mechanism for electromagnetic energy to enter the systems tunnel. This is accomplished by determining the mutual coupling between cables and calculating the currents on the outer shields of the USBI cables. The multiconductor cable analysis is documented in Section 4.3.2 and the results are presented in Section 4.3.3.

The objective of the single conductor cable analysis is to determine the open-circuit voltages and short-circuit currents of the inner conductors of the USBI cables. The analysis is documented in Section 4.3.4 and a discussion of the results are presented in Section 4.3.5.

4.3.2 Multiconductor Cable Analysis

The coupling of electromagnetic energy from a lightning strike to the cables within the systems tunnel can be modeled using a one-dimensional time domain representation of the telegrapher's equations. The voltages and currents induced on a multiconductor transmission line are determined from [1]

$$\frac{\partial}{\partial x}\left[V(x,t)\right] + \frac{\partial}{\partial t}\left[L(x)\right]\left[I(x,t)\right] + \left[R(x)\right]\left[I(x,t)\right] = \left[E(x,t)\right]$$

$$\frac{\partial}{\partial x}\left[I(x,t)\right] + \frac{\partial}{\partial t}\left[C(x)\right]\left[V(x,t)\right] + \left[G(x,t)\right]\left[V(x,t)\right] = \left[J(x,t)\right]$$

where

N	is the number of cables in the transmission line,
$[V(x,t)]$	is the NX1 matrix of voltages on each cable,
$[I(x,t)]$	is the NX1 matrix of currents on each cable,

$[C(x)]$ is the NXN capacitance matrix in farads/meter,

$[L(x)]$ is the NXN inductance matrix in henries/meter where $[L(x)] = \mu\varepsilon \quad [C(x)]^{-1}$, μ is the permeability and ε is the permittivity of the surrounding homogeneous medium,

$[R(x)]$ is the NXN diagonal resistance matrix in ohms/meter,

$[G(x)]$ is the NXN conductance matrix in mhos/meter,

$[E(x)]$ is the NX1 matrix of distributed voltage sources in volts/meter, and

$[J(x,t)]$ is the NX1 matrix if distributed current sources in amperes/meter.

These equations are numerically implemented in a finite difference scheme. With k defined as the spatial step index and n as the time step index, the equations are expressed as

$$[I_k^{n+1}] = \left[L_k + \frac{\Delta t R_k}{2}\right]^{-1} \left\{\Delta t[E_k^{n+1}] - \frac{\Delta t}{\Delta x}\left[V_{k+1}^{n} - V_k^{n}\right] + \left[L_k - \frac{\Delta t R_k}{2}\right][I_k^{n}]\right\}$$

for $k=1,2,\ldots,k_{max}-1$,

$$[V_k^{n+1}] = [V_k^{n}]) + [C_k]^{-1}\left\{\frac{\Delta t}{\Delta x}\left[I_k^{n+1} - I_{k-1}^{n+1}\right]\right\}$$

for $k=2,3,\ldots,k_{max}-1$,
and $n=0,1,2,\ldots,n_{max}$.

The cable boundary conditions for resistive terminations yields the following voltage equations:

$$[V_1^{n+1}] = \left[\frac{C_1}{\Delta t} + \frac{4}{3\Delta x} Y_1\right]^{-1}\left\{\left[\frac{C_1}{\Delta t} - \frac{4}{3\Delta x}\right][V_1^{n}] - \frac{1}{3\Delta x}\left[9I_1^{n+1} - I_2^{n+1}\right]\right\}$$

$$\left[V_{k_{max}}^{n+1}\right] = \left[\frac{C_{k_{max}}}{\Delta t} - \frac{4}{3\Delta t} Y_{k_{max}}\right]^{-1}\left\{\left[\frac{C_{k_{max}}}{\Delta t} - \frac{4}{3\Delta x} Y_{k_{max}}\right]\left[V_{k_{max}}^{n}\right]\right.$$

$$\left. + \frac{1}{3\Delta x}\left[9I_{k_{max}-1}^{n+1} - I_{k_{max}-2}^{n+1}\right]\right\}$$

where $[Y_k]$ is the NXN matrix with the following definitions:

$$Y_{ij} = -\frac{1}{R_{ij}} \quad \text{for } i \neq j, \text{ and } Y_{ii} = \sum_{j=1}^{N} \frac{1}{R_{ij}}$$

where the $[R_k]$ are the load resistances.

The medium surrounding the cables can be characterized as a dielectric with low permittivity, so the conductivity of the medium is negligibly small. Also there is no cable excitation due to the J(x,t) current source term. The spatial step increment is 0.3 meter and the time step increment is 0.6 nanosecond.

The capacitive and inductive matrices in the above transmission line equations are calculated from the cross sectional geometry of the systems tunnel. (The geometries are discussed later in this section).

For a multiconductor transmission line of N conductors where the N+1 conductor is chosen as the reference conductor (in this analysis the systems tunnel is the reference conductor), the elements of the capacitance matrix are defined as follows:

C_{ii} is the per-unit-length self capacitance of the i'th conductor and is numerically equal to the charge per-unit-length on the i'th conductor when it is at one volt potential, and all other conductors are at zero potential with respect to the reference conductor. These values are greater than zero.

C_{ij} is the per-unit-length mutual capacitance between the i'th conductor when the j'th conductor is at one volt potential, and the rest of the conductors are at zero potential with respect to the reference conductor. These capacitance values are less than zero.

The capacitance matrix is determined by solving Laplace's equation by assuming that each conductor boundary consists of a finite number of line charges and applying Gauss' law to solve the resulting potential problem. This leads to a system of integral equations which are expressed as a set of linear equations by breaking the contour of each conductor into subintervals where the charge per-unit-length is uniform over a subinterval. This allows the set of linear equations to be written in matrix form.

The calculations are performed by dividing the N conductors into two groups and assigning a potential difference of one volt between the two groups. One conductor at a time is raised to the one volt potential with the remaining conductors held at the reference potential (ground). The matrix equation is solved to determine the charge per-unit-length. Once the charge density is determined, the desired capacitance is calculated using

$$C = \sum_{q=1}^{M_i} p_{qi} \int_{c_{qi}} dl$$

where M_i is the number of subcontours for the i'th conductor,

p_{qi} is the charge per-unit-length of the q'th subcontour of the i'th conductor, and

$\int_{c_{qi}} dl$ is the contour line integral for the i'th conductor.

The inductance matrix is calculated by solving the equation $[L][C] = \mu_o \varepsilon_o \varepsilon_r$. The relative permittivity ε_r was chosen to have a value of 2. This value is slightly lower than the cable insulation dielectric constants for teflon (ε_r = 2.4) and polytetrafluoroethylene (TFE, ε_r = 2.3) in order to take into account air within the surrounding medium. The complete theoretical formulation and analytical procedure of the capacitance matrix analysis is presented in detail in references [2] and [3].

The multiconductor cable model configuration is shown in Figure 4.3.1. The cable numbering system in the figure is consistent with the test article cable numbering system as presented in Figure 2.2.5.

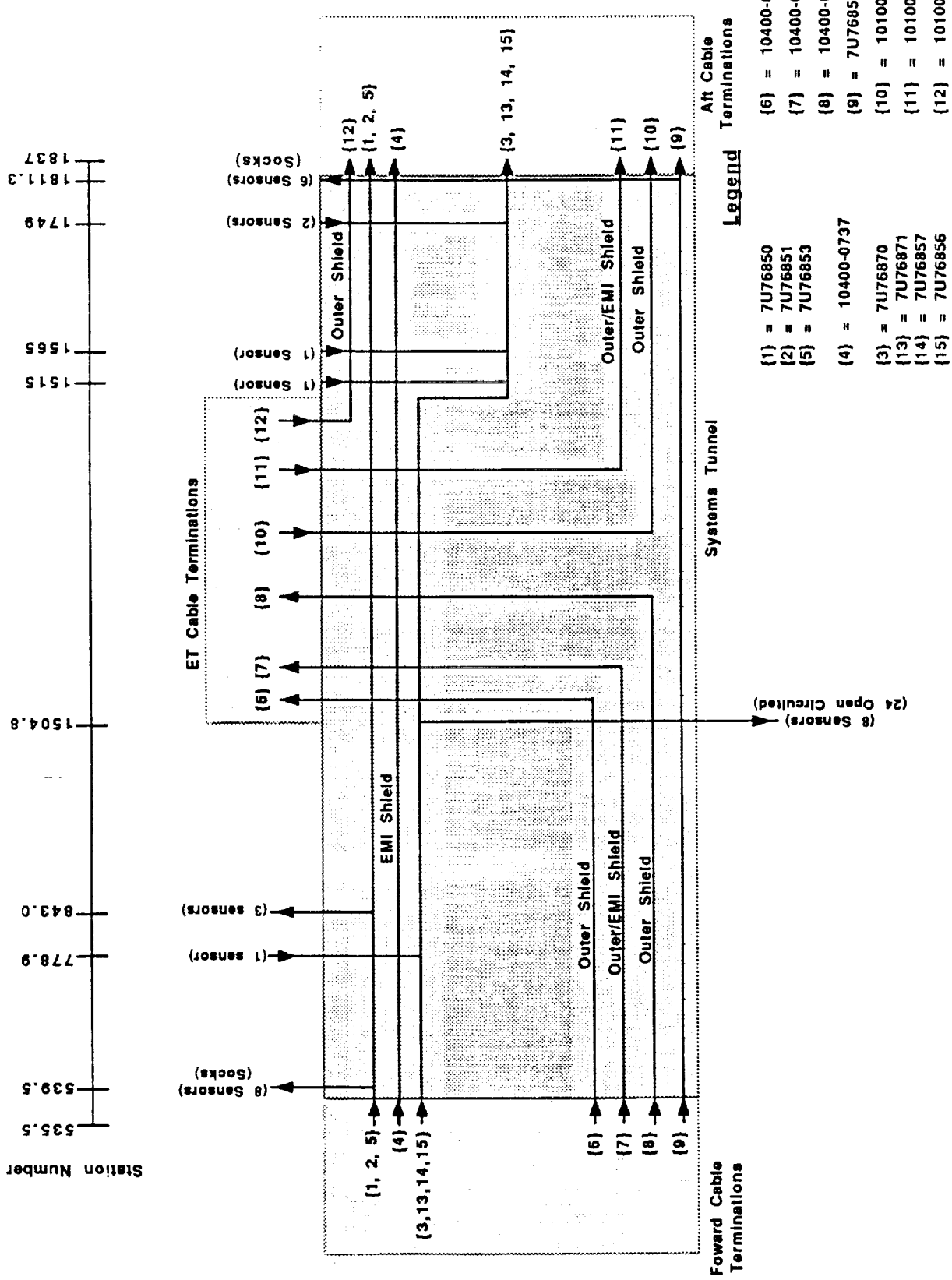

Figure 4.3.1 Cable Diagram Sketch/Systems Tunnel

The systems tunnel cable model combines cables 1, 2, and 5, and cables 3, 13, 14, and 15 into two bulk conductors that run the length of the tunnel. The diameter of each bulk conductor is determined by summing the cross-sectional areas of each cable and then calculating a diameter from this summation. The bulk conductors change in diameter as DFI cables enter and exit the systems tunnel. The cable model incorporates six systems tunnel cross-sectional changes. Table 4.3.1 lists the outer shield diameters of the USBI cables, and the DFI bulk conductor diameters and station numbers where the diameters change. Illustrative examples of a forward tunnel cross section and an aft tunnel cross section are shown in Figures 4.3.2 and 4.3.3 . The capacitive and inductive matrices which electrically describe these two cross-sectional geometries are given in Appendix D. The cable model simplifications were necessary in order to satisfy the numerical stability constraints of this problem.

The multiconductor systems tunnel cable model is used to analyze the coupling effects of the two main points of entry for electromagnetic energy to enter the systems tunnel: the DFI cables which penetrate the systems tunnel, and the seam apertures which occur at the interface of systems tunnel covers. The DFI cables are connected to sensors on the external surface of the solid rocket booster (SRB), run along the surface of the SRB and penetrate the systems tunnel at numerous station number locations. When a lightning strike occurs, a current pulse is induced on the DFI cables, propagates along the cables, enters the systems tunnel, and induces a current on the cables inside the tunnel. The analysis of a lightning strike to the SRB has been presented in Section 4.2. In this analysis the open circuit voltages and short circuit currents of the DFI cables external to tunnel were used to calculate a Thevenin equivalent circuit impedance which characterizes the external DFI cables. The equivalent impedance was determined to be dominantly capacitive, and the values were listed in Table 4.2.4.

Each external DFI cable is represented as an equivalent circuit which drives a bulk conductor inside the systems tunnel. Figure 4.3.4 is an illustration of an equivalent circuit. Applying Kirchhoff's voltage law gives

$$V_k = V_{oc} + L_d \frac{dI_d}{dt} + \frac{1}{C_d} \int I_d dt$$

Table 4.3.1

Cable Parameters Used in Multi-Conductor Cable Model

USBI SHIELDED CABLES

Cable No.	Cable OD (IN)	Jacket Thickness (IN)	Shield OD (IN)
[4]	0.790	0.02	0.75
[6]	0.396	0.058	0.279
[7]	1.116	0.02	1.076
[8]	0.858	0.02	0.818
[10]	0.858	0.02	0.818
[11]	1.116	0.02	1.076
[12]	0.396	0.058	0.279

DFI BULK CONDUCTORS

Cable No.	Cable OD (IN)	Change at Station No.	New Cable OD	Change at Station No.	New Cable OD	Change at Station No.	New Cable OD
[1,2,5]	0.62	539.5	0.49	843	0.44	---	---
[3,13,14,15]	0.75	1504.8	0.186	1565	0.49	1749	0.53
[9]	1.02	---	---	---	---	---	---

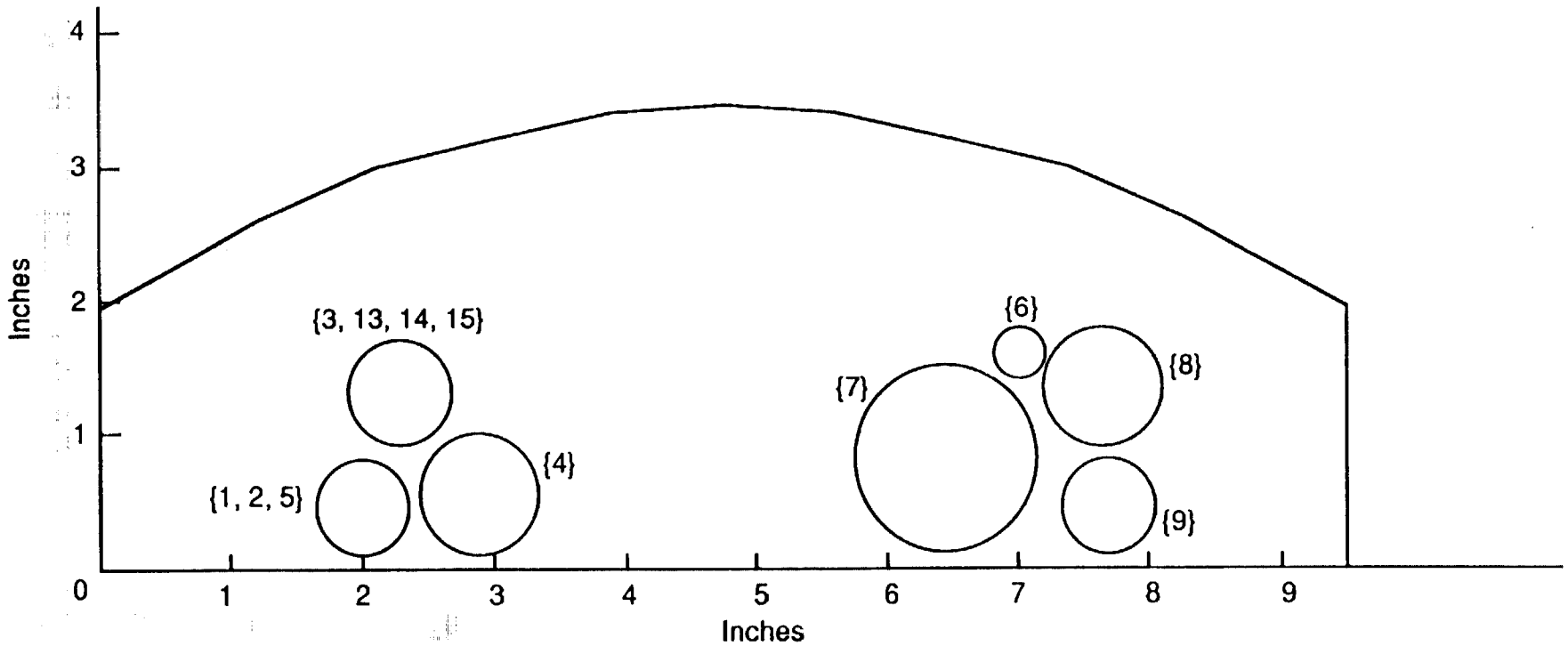

Figure 4.3.2 Cross-Section of Forward Tunnel (Cross-Section Number 1)

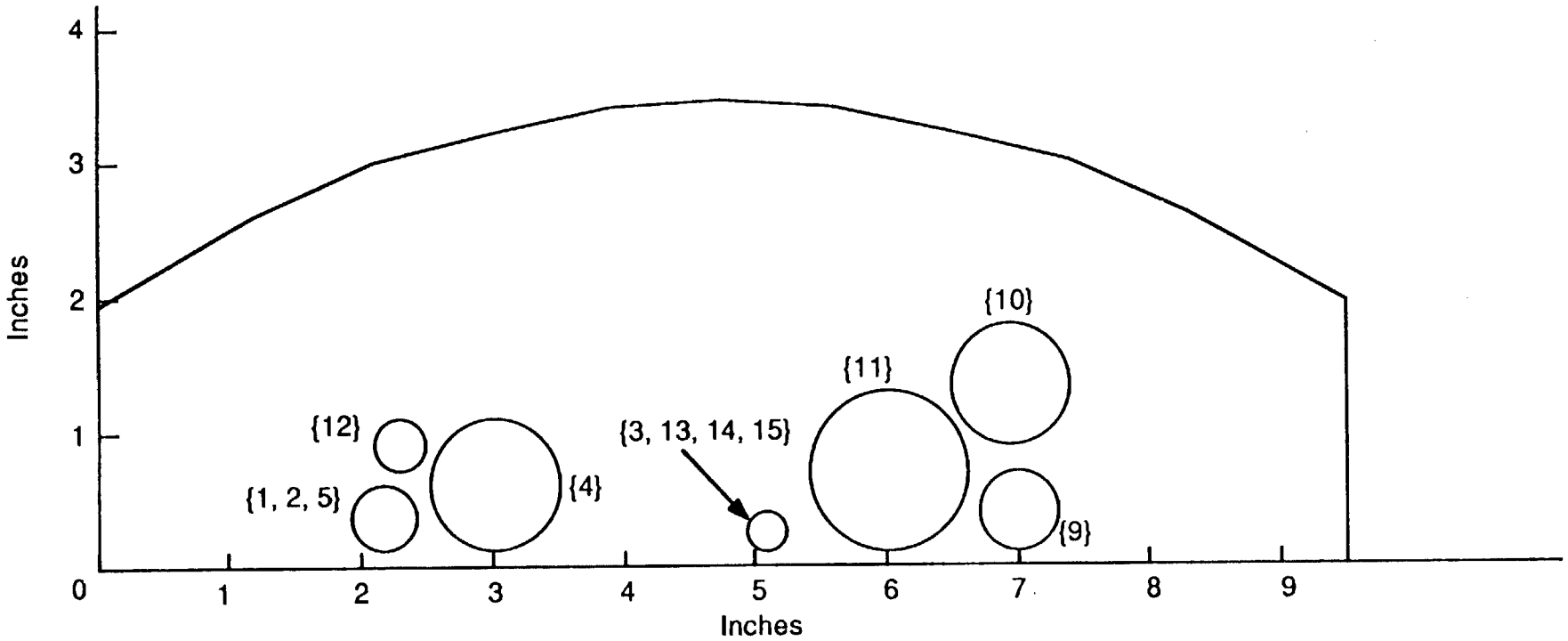

Figure 4.3.3 Cross-Section of Aft Tunnel (Cross-Section Number 4)

Table 4.3.2
Tabulation of Seam Aperture Locations

SEAM NO.	STATION NUMBER
Forward Tunnel	
1	583
2	638
3	697
4	740
5	798
6	857
7	864
Aft Tunnel	
8	1518
9	1583
10	1596
11	1635
12	1655
13	1684
14	1703
15	1715
16	1732
17	1755
18	1775
19	1804
20	1823

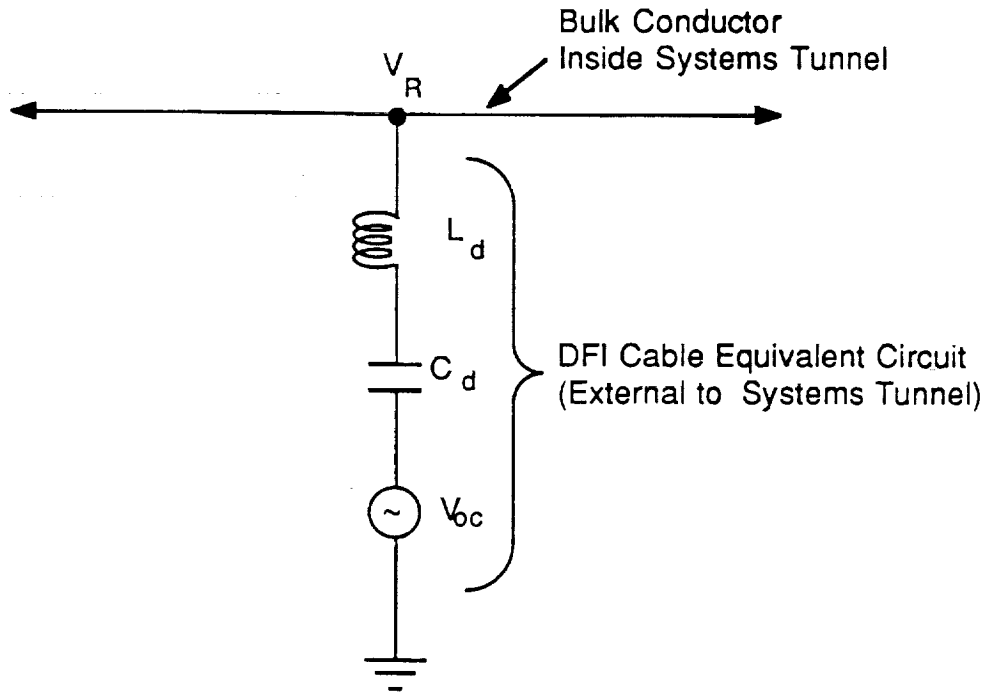

Figure 4.3.4 DFI Cable Equivalent Circuit

From the above equation and in finite difference form, the current I_d entering the systems tunnel on a DFI cable is written as

$$I_d^{n+1} = \left(2 - \frac{\Delta t^2}{L_d C_d}\right) I_d^n - I_d^{n-1} + \frac{\Delta t}{L_d}\left(V_k^n - V_k^{n-1} - V_{oc}^n + V_{oc}^{n-1}\right)$$

where V_k is the voltage at the bulk conductor, V_{oc} is the external DFI cable open circuit voltage, and C_d is the equivalent circuit capacitance. A small inductance L_d is added to the equivalent circuit in order to lend numerical stability.

The current I_d is coupled into the bulk conductor by applying Kirchhoff's current law. The voltage equation for the bulk conductor at the k'th spatial position in finite difference form becomes

$$\left[V_k^{n+1}\right] = \left[V_k^n\right] + \left[C_k\right]^{-1}\left\{\frac{\Delta t}{\Delta x}\left[I_k^{n+1} - I_{k-1}^{n+1}\right]\right\} - \frac{1}{C_{kii}}\frac{\Delta t}{\Delta x} I_d^{n+1}$$

The second point-of-entry for lightning electromagnetic energy is the seam apertures created by the joining of the tunnel covers. The cable model incorporates 20 tunnel seam apertures, and the station number of each seam is presented in Table 4.3.2. The impedance of each seam is characterized by the "jumper" straps which run across the seam and are bonded to the adjoining tunnel covers. The analysis assumes that there are two 4 inch straps across each seam, and the resistance and inductance per-unit-length of each strap is 132μΩ/inch and 25nH/inch, respectively [4].

The electric field E(x,t) inside the tunnel is expressed as

$$E(x,t)=R_{seam}\, J_{seam}(x,t) + L_{seam}\ \frac{d}{dt} J_{seam}(x,t)$$

where R_{seam} = 0.26mΩ, L_{seam} = 0.05μH, and $J_{seam}(x,t)$ is the tunnel surface current density at the seam. The values used for the surface current density on the tunnel were calculated in the analysis presented in Section 4.2. In this analysis the surface current density on the SRB at the location of the tunnel were determined for a 1 meter grid size, and are used as the current density on the systems tunnel.

4.3.3 Results of the Multiconductor Cable Analysis

The results of the multiconductor systems tunnel cable analysis is presented in Table 4.3.3. The table is a tabulation of the peak currents on the USBI shielded cables for the 3 cases where the cables inside the tunnel are driven by all 20 tunnel seams, the first 3 seams of the forward tunnel, and the DFI cables which enter the systems tunnel. The 3 seam case was included in order to present the dominant effect of the coupling through the seam apertures nearest a lightning strike to the tunnel. In this analysis, the attachment point is to the head of the forward tunnel. Table 4.3.3 indicates that the DFI coupling response is more than 45 dB below the response due to coupling through the 20 seam aperatures, and more than 35 dB below the cable response of the 3 seam case. The results also indicate that greater than 70% of the electromagnetic energy coupling to cables inside the tunnel is due to the first 3 seam apertures.

Table 4.3.3

Results of Multi-Conductor Cable Model Calculations Short Circuit Current Peak Values on USBI Cable Outer Shields

Cable No.	Excitation Due to 20 Seams	Excitation Due to Initial 3 Seams	Excitation Due to DFI Cables
6	115	84	0.003
7	773	588	0.031
8	431	371	0.002
10	306	-98	0.023
11	930	-115	2
12	169	-245	1

Figures 4.3.5 through 4.3.7 illustrate the waveforms of the currents on the outer shields of the USBI cables for the three coupling cases described above. For the seam driven cases, the currents on the shields are proportional to the time integral of the electric field inside the systems tunnel. For the case where only the first 3 seam apertures are driven, the currents on the USBI cable shields in the aft tunnel are due to the coupling between these cables and the cables which run the length of the systems tunnel. The cables which run the length of the tunnel are driven by the electric field in the forward tunnel and induce a current in the opposite direction on the USBI cable shields in the aft tunnel. Figure 4.3.6 (d) through (f) illustrate these induced currents.

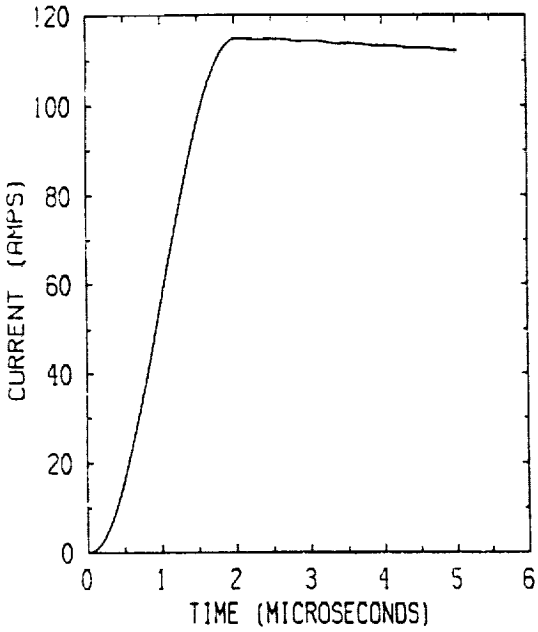

(a) Short Circuit Current on Cable {6} Outer Shield

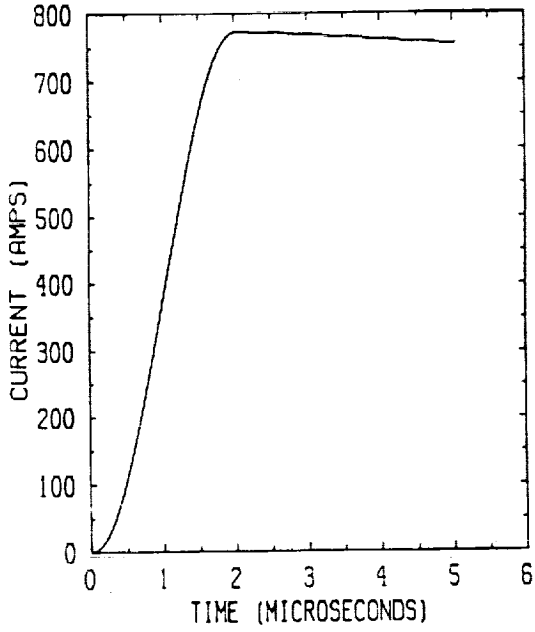

(b) Short Circuit Current on Cable {7} Outer Shield

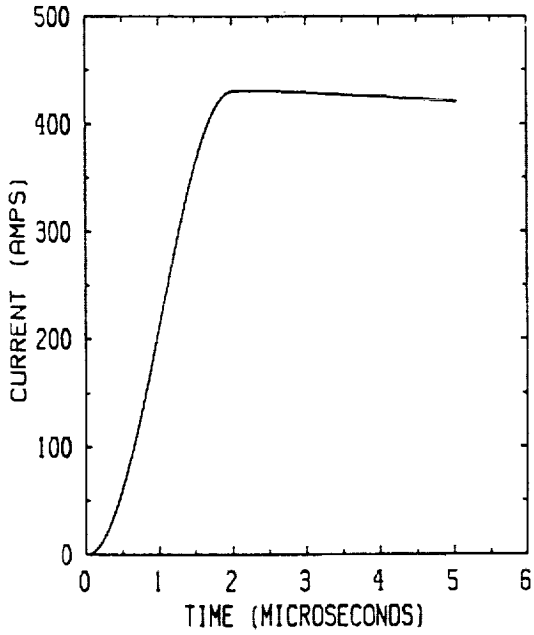

(c) Short Circuit Current on Cable {8} Outer Shield

Figure 4.3.5 Current on USBI Cable Outer Shields. Shield Currents are Driven by Coupling Through 20 Seam Apertures

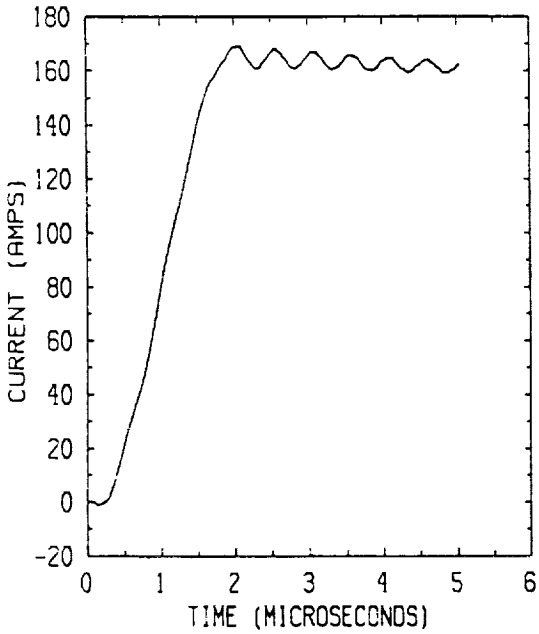

(d) Short Circuit Current on Cable {12} Outer Shield

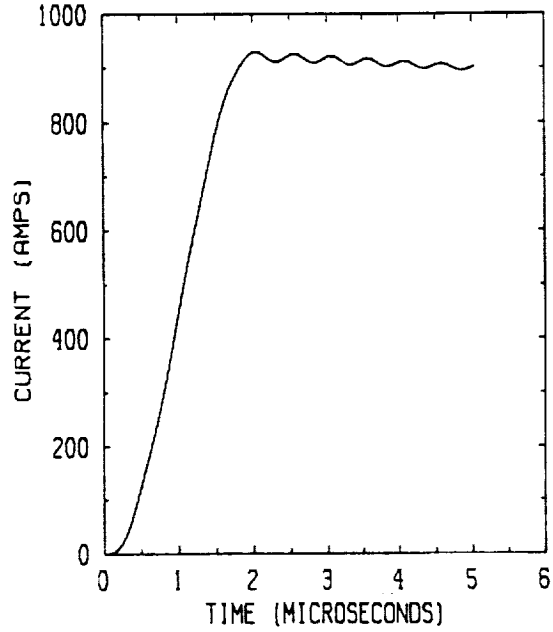

(e) Short Circuit Current on Cable {11} Outer Shield

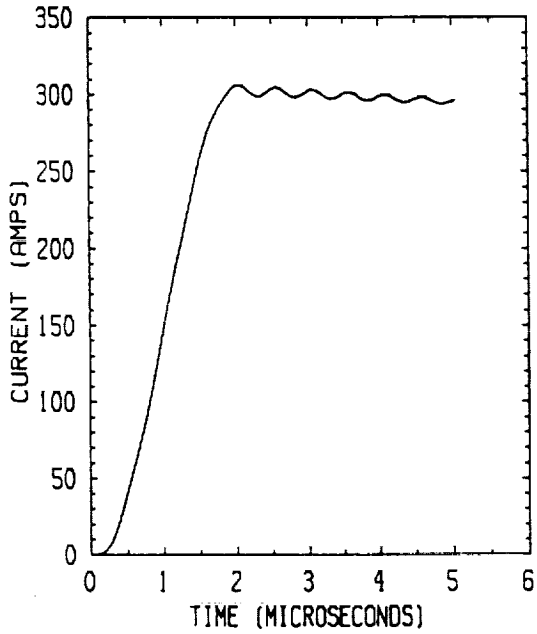

(f) Short Circuit Current on Cable {10} Outer Shield

Figure 4.3.5 (Cont'd.) Current on USBI Cable Outer Shields. Shield Currents are Driven by Coupling Through 20 Seam Apertures

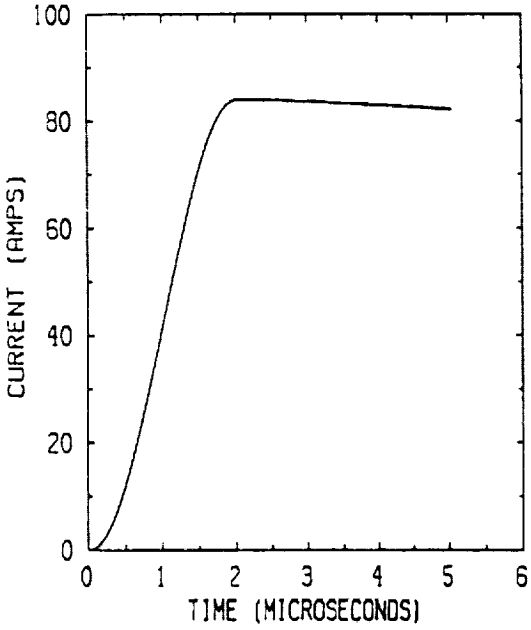

(a) Short Circuit Current on Cable {6} Outer Shield

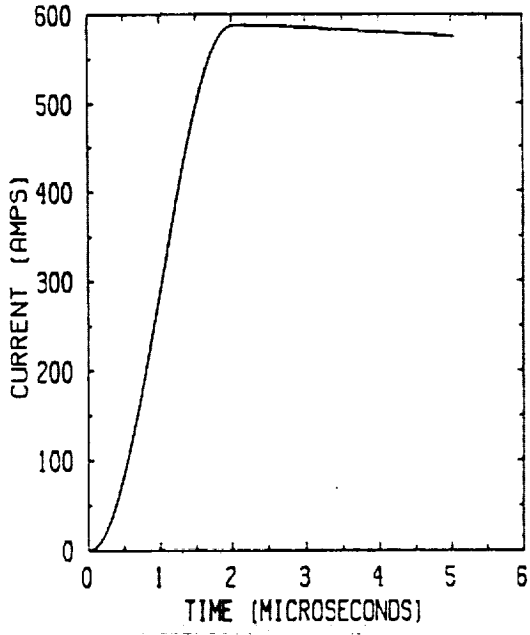

(b) Short Circuit Current on Cable {7} Outer Shield

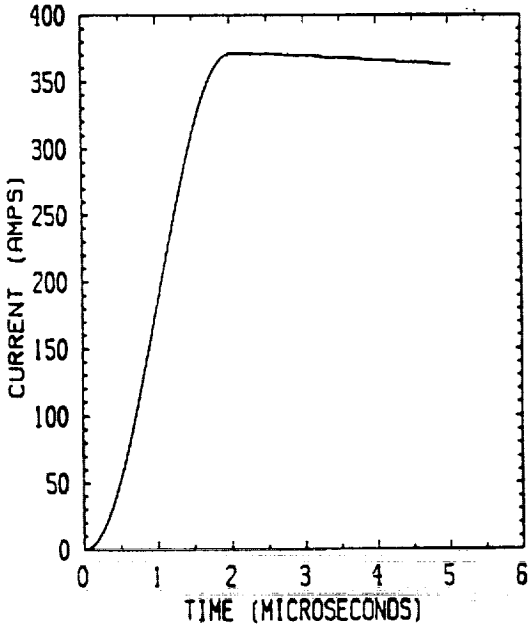

(c) Short Circuit Current on Cable {8} Outer Shield

Figure 4.3.6 Current on USBI Cable Outer Shields. Shield Currents are Driven by Coupling Through Initial 3 Seam Apertures of Forward Tunnel

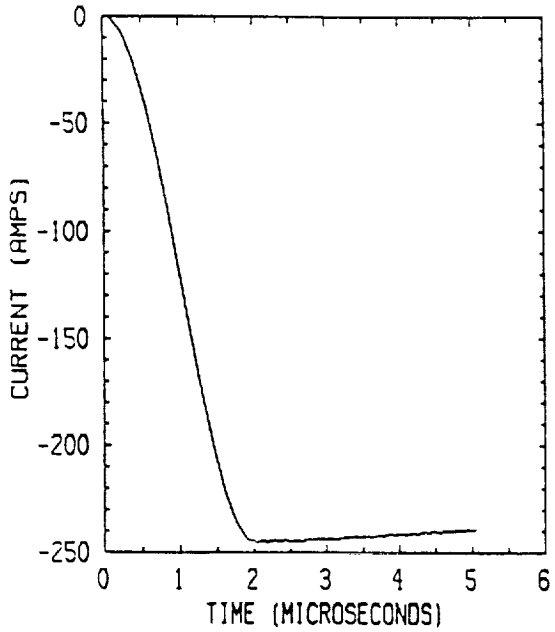

(d) Short Circuit Current on Cable {12} Outer Shield

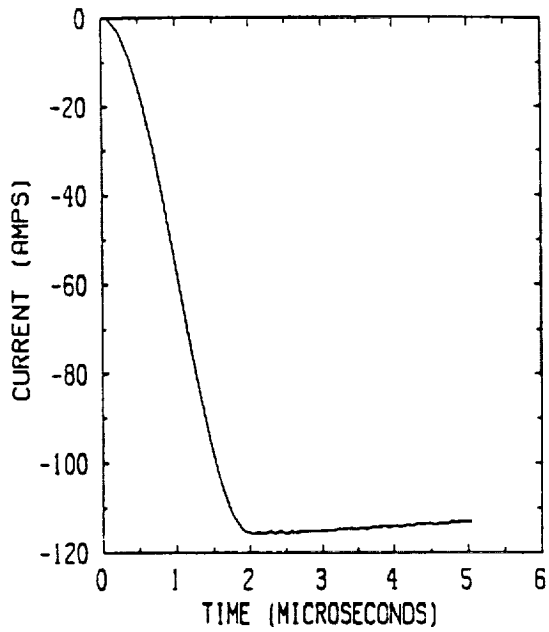

(e) Short Circuit Current on Cable {11} Outer Shield

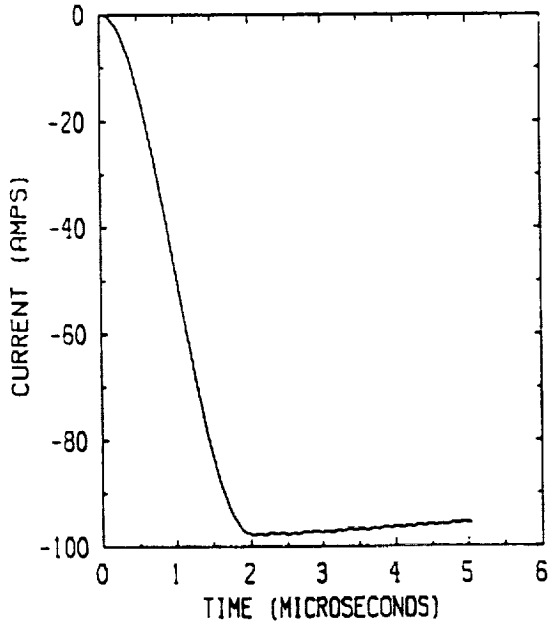

(f) Short Circuit Current on Cable {10} Outer Shield

Figure 4.3.6 (Cont'd.) Current on USBI Cable Outer Shields. Shield Currents are Driven by Coupling Through Initial 3 Seam Apertures of Forward Tunnel

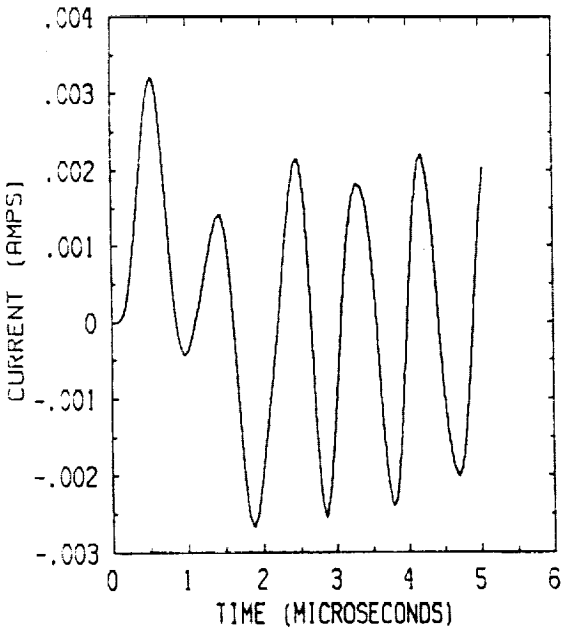

(a) Short Circuit Current on Cable {6} Outer Shield

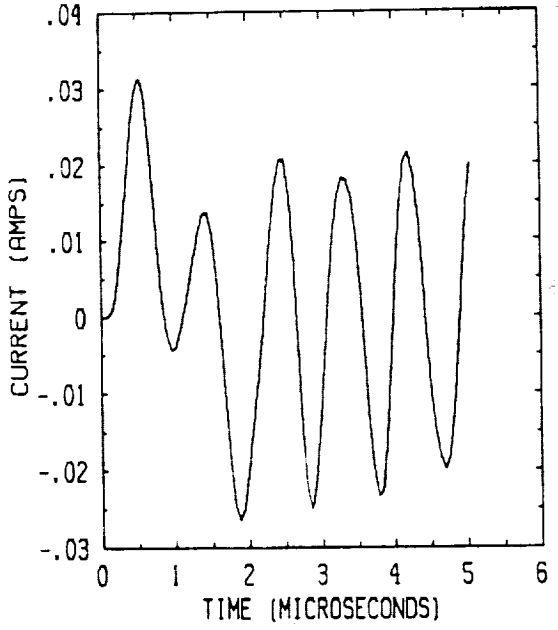

(b) Short Circuit Current on Cable {7} Outer Shield

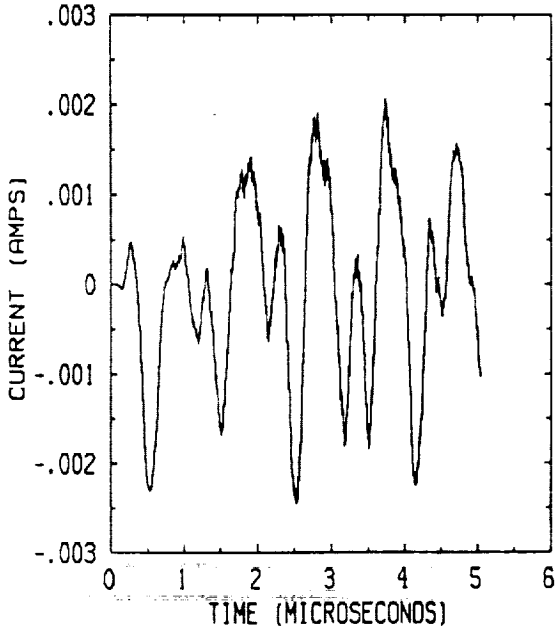

(c) Short Circuit Current on Cable {8} Outer Shield

Figure 4.3.7 Current on USBI Cable Outer Shields. Shield Currents are Driven by Coupling From DFI Cables

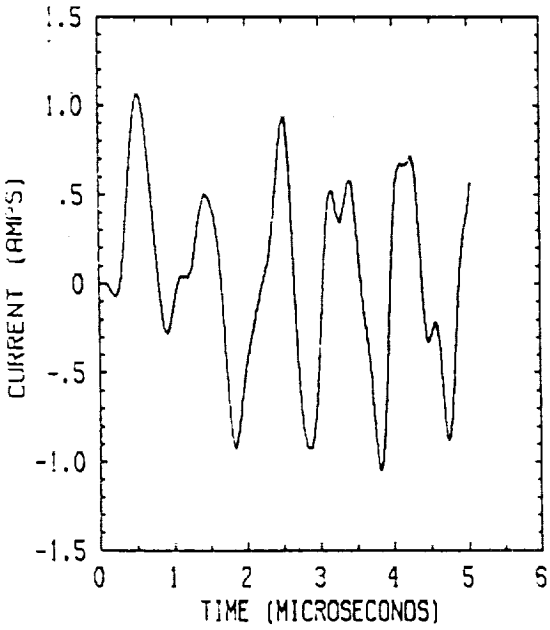

(d) Short Circuit Current on Cable {12} Outer Shield

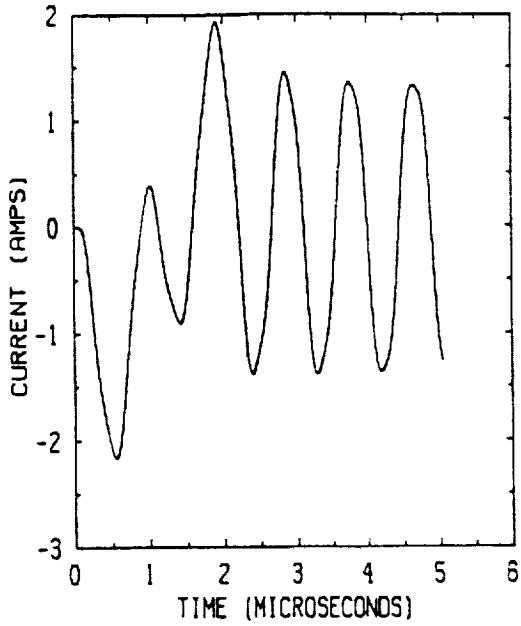

(e) Short Circuit Current on Cable {11} Outer Shield

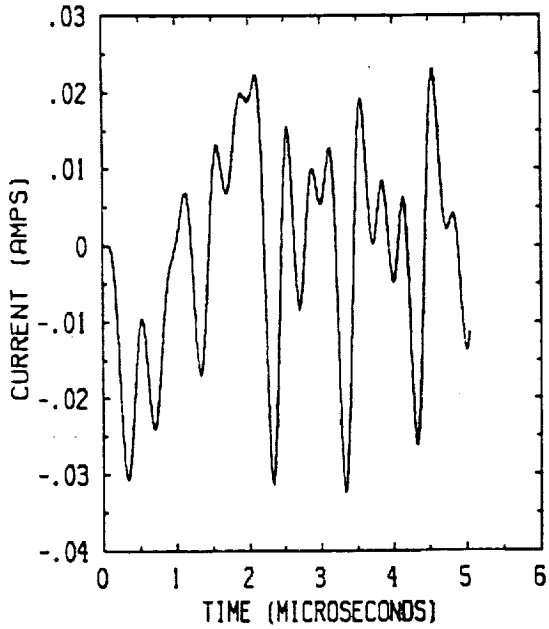

(f) Short Circuit Current on Cable {10} Outer Shield

Figure 4.3.7 (Cont'd.) Current on USBI Cable Outer Shields. Shield Currents are Driven by Coupling From DFI Cables

The shield current plots shown in Figure 4.3.7 illustrate the coupling between the DFI driven cables and the USBI shielded cables in the systems tunnel. For this case the USBI cable shields in the aft tunnel display greater peak amplitudes than their counterpart in the forward tunnel. The reason for this is because the USBI aft tunnel cables are located much closer to the driven DFI cables so the coupling is much stronger than for the USBI cables in the forward tunnel. The bipolar character of these waveforms is due to the resonance which appears on the surface current density waveform. This resonance is associated with the geometry of the SRB test object.

4.3.4 Single Conductor Cable Analysis

The second part of the cable modeling analysis involved developing a single conductor cable model in order to calculate the short circuit currents and open-circuit voltages of the inner conductors of USBI shielded cables 6, 8, 10, and 12. In this analysis, each USBI cable is excited by the electric field due to the seam apertures of the forward and aft systems tunnel sections. There is no mutual coupling effects between cables. The inner conductor is driven by an electric field $E_{in}(x,t)$ inside the shield which is defined as

$$E_{in}(x,t) = R_{sh}\, I_{sh}(x,t) + L_{sh}\, \frac{d}{dt}\, I_{sh}(x,t)$$

where R_{sh} is the resistance per-unit-length of the outer shield, L_{sh} is the inductance per-unit-length of the outer shield, and $I_{sh}(x,t)$ is the current on the outer shield. The impedance values of the USBI shields were scaled from measured values of a shielded cable 18 inches long with a diameter of 0.52 inches [5]. Table 4.3.4 lists these shield impedance values for cables 6, 8, 10, and 12. The inner conductor of the USBI cable model represents the internal wires of the shielded cable. The diameter of the inner conductor is determined from its cross-sectional area which is the sum of the cross-sectional areas of the individual wires.

The single conductor cable model is a self-consistent model which takes into account the negative coupling of the inner conductor current to the outer shield current. The electric field $E_{ic}(x,t)$ which acts to suppress the growth of the current on the outer shield is defined as

$$E_{ic}(x,t) = R_{sh}\, I_{ic}(x,t) + L_{sh}\, \frac{d}{dt}\, I_{ic}(x,t)$$

where $I_{ic}(x,t)$ is the current on the inner conductor. The transmission line equations which describe this cable model are the the same equations used in the multiconductor cable analysis, except the capacitance and inductance matrices become a single value. The capacitance and inductance values of the outer shields are determined by adding the matrix values (used in the multiconductor analysis) of

Table 4.3.4
Outer Cable Shield Transfer Impedances

Cable No.	R_{sh} (mΩ/meter)	L_{sh} (nH/meter)
6	6.1	4
8	2.2	1.1
10	2.2	1.1
12	6.1	4

the respective row which represents that particular USBI cable (see Appendix D). The capacitance and inductance of the inner conductor are calculated using the following equations:

$$C = \frac{2\pi\varepsilon_o\varepsilon_r}{\ln (b/a)} \qquad (F/m)$$

$$L = \frac{\mu_o}{2\pi} \ln (b/a) \qquad (H/m)$$

where b is the shield inner diameter, a is the inner conductor diameter, and $\varepsilon_r = 2$. The cable diameters and capacitive and inductive values are given in Table 4.3.5.

Table 4.3.5
Cable Parameters Used in Single-Conductor Cable Model

Cable No.	Shield OD (IN)	Shield ID (IN)	Inner Conductor OD (IN)	Shield Capacitance (pF/meter)	Shield Inductance (nH/meter)	Inner Conductor Capacitance (pF/meter)	Inner Conductor Inductance (nH/meter)
6	0.279	0.255	0.134	11	2020	178	124
8	0.818	0.794	0.252	40.2	553	96.9	229
10	0.818	0.794	0.252	33.3	668	96.9	229
12	0.279	0.255	0.134	12.3	1800	178	124

4.3.5 Results of the Single Conductor Cable Model Analysis

The results of the single conductor cable model calculations are presented in Table 4.3.6. The table is a tabulation of peak short-circuit currents and open-circuit voltages for USBI cables 6, 8, 10, and 12. Comparing the calculated shield currents in the table and the shield currents listed in Table 4.3.3 indicates reasonable agreement. The calculated current and voltage waveforms for the cables listed in the table are illustrated in Figures 4.3.8 and 4.3.9.

Table 4.3.6 also lists the scaled high current bank experimental values. The comparison between the scaled measurements and the calculations indicates discrepancies between the cable model and the test article. The calculations of the peak short-circuit current values are an average of 62% greater and the peak open-circuit voltages are an average of 44% smaller than the scaled measured values. One possible reason for the discrepancies is the impedance used for the jumper strap cable. The resistive and inductive values used to define the impedance were based upon the generic values of an AWG-12 copper wire, and the length of the strap was determined by scaling from assembly drawings of the systems tunnel [4]. A change in the impedance will significantly effect the electric field inside the tunnel which is the dominant source of cable excitation.

The resistive and inductive values which define the impedance of the USBI cable shields are another set of critical parameters which effect the accuracy of the modeling. Since accurate values for the impedance of the cable shields were unobtainable, the impedances were scaled from shield measurements given in reference [5]. The electric field inside a cable shield which drives the inner conductor (internal wires) is determined from the shield impedance, so a change in the electric field inside the shield will effect the open-circuit voltage and short-circuit current calculations.

A third possible reason for the discrepancies is the dependence of the capacitive and inductive matrix calculations on the accuracy of the systems tunnel cross-sectional layout. The cross-sectional geometries were determined from USBI and TC drawings, but the cable placements, and spacings between cables and cables to systems tunnel floor were arbitrary. The cable simplifications incorporated in the

Table 4.3.6

Results of Single Conductor Cable Model Calculations in Comparison with Scaled High Current Bank (HCB) Measurements

Cable No.	Calculated Outer Shield Current (Amps)	Inner Conductor Short-Circuit Current (Amps)	Scaled HCB Short-Circuit Current (Amps)	Inner Conductor Open-Circuit Voltage (Volts)	Scaled HCB Open-Circuit Voltage (Volts)
6	115	71	81	5.9	26.7
8	418	126	90.6	7.7	16.8
10	319	100	22.9	5.9	9.4
12	119	72	13.6	6.1	6.4

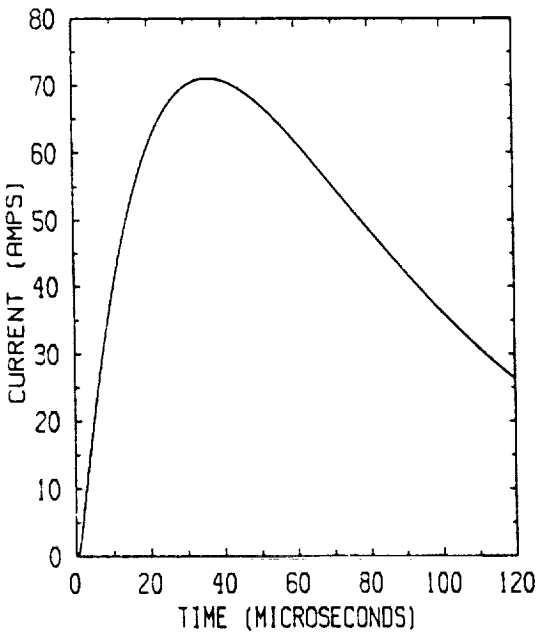

(a) Short Circuit Current on Cable {6} Inner Conductor

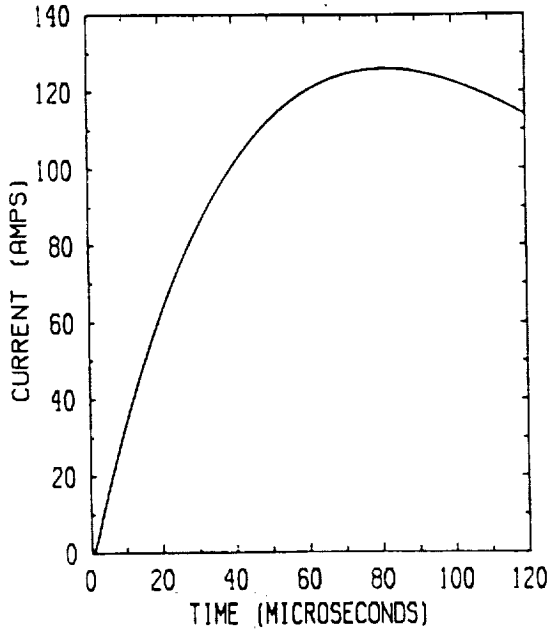

(b) Short Circuit Current on Cable {8} Inner Conductor

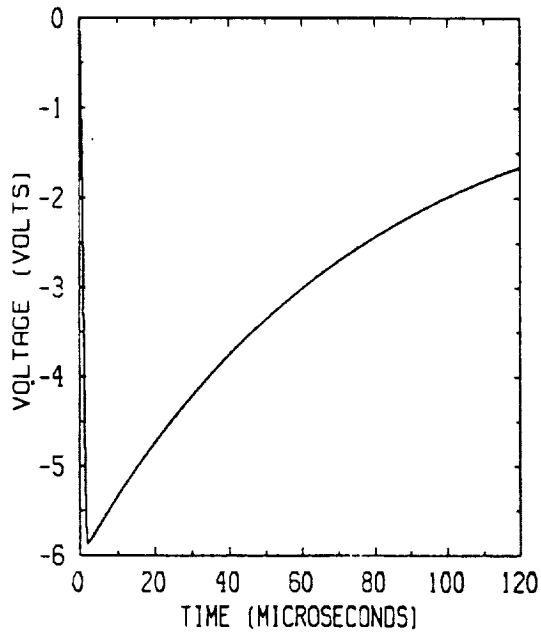

(c) Open Circuit Voltage on Cable {6} Inner Conductor

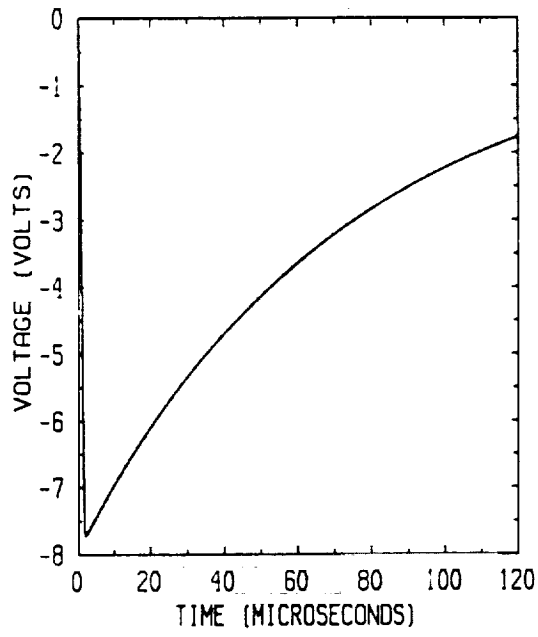

(d) Open Circuit Voltage on Cable {8} Inner Conductor

Figure 4.3.8 Short Circuit Currents and Open Circuit Voltages of USBI Cables {6} and {8} Inner Conductors. Cable Excitation is due to Forward Tunnel Seam Apertures

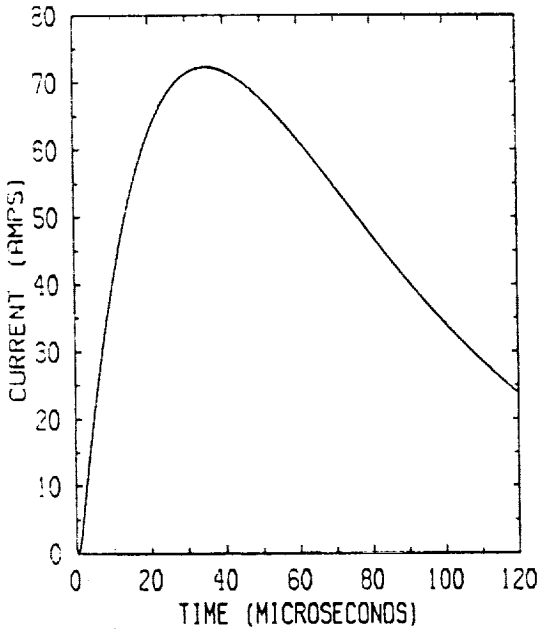

(a) Short Circuit Current on Cable {12} Inner Conductor

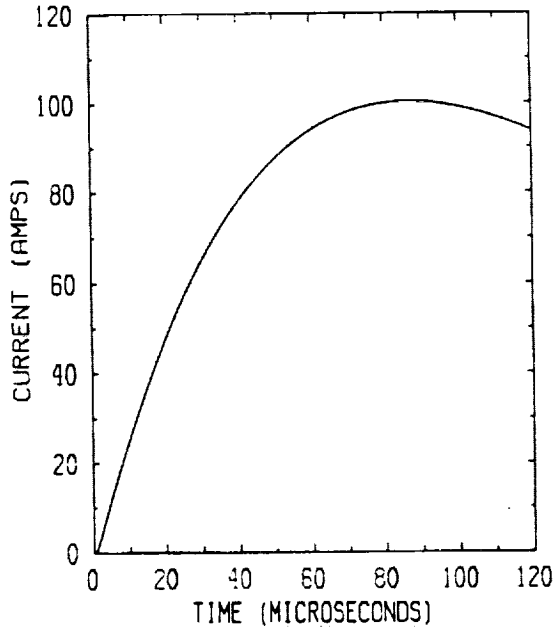

(b) Short Circuit Current on Cable {10} Inner Conductor

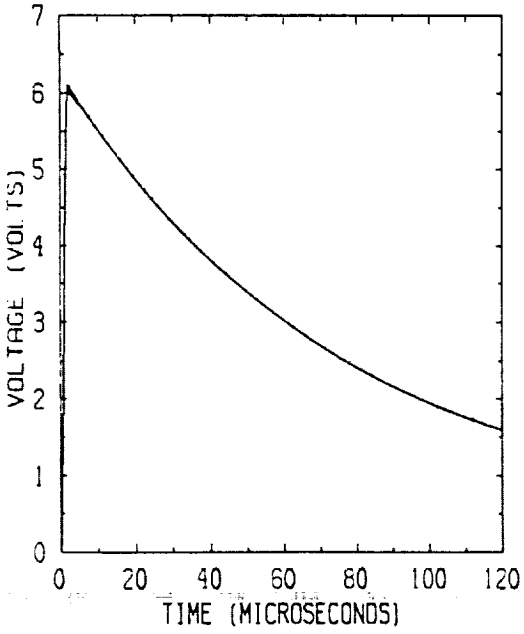

(c) Open Circuit Voltage on Cable {12} Inner Conductor

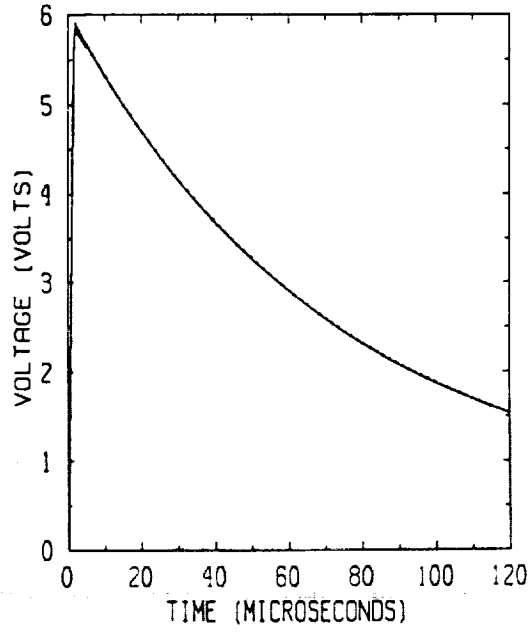

(d) Open Circuit Voltage on Cable {10} Inner Conductor

Figure 4.3.9 Short Circuit Currents and Open Circuit Voltages of USBI Cables {10} and {12} Inner Conductors. Cable Excitation is due to Forward Tunnel Seam Apertures

model also introduce a degree of error in the matrix calculations. Also accurate diameter dimensions of the cables within the tunnel were unavailable.

It is believed that with accurate measured impedances and lengths of the jumper straps and impedances and diameters of the cable shields, along with iteratively calculating the capacitive and inductive matrices, much better correlation between model calculations and test measurements can be achieved.

4.4 Modeling Analyses Summary and Conclusions

The maximum open-circuit voltage calculated on the DFI cables at the systems tunnel interface is 970 volts. The maximum short-circuit current is 1.1 amperes. The utilization of sock shields results in cable voltage reductions of 40 dB to 90 dB and current reductions of 30 dB to 70 dB. The longer the sock shield length the greater the reduction.

The results of the systems tunnel analysis indicates that coupling through the seam apertures, created by the joining of tunnel covers, is the dominant mechanism by which lightning electromagnetic energy excites the cables within the tunnel. The currents induced on the USBI cable shields due to this coupling mechanism are 45 db or greater in comparison to the shield currents induced by excited DFI cables penetrating the systems tunnel.

For a direct lightning strike to the head of the systems tunnel greater than 70% of the electromagnetic energy penetrating the systems tunnel is through the initial 3 seam apertures. Applying a grounding scheme which would short the surface currents on the tunnel to the SRB case would significantly reduce the coupling through the seam apertures. An example of a grounding scheme would be to introduce additional grounding straps from the tunnel covers to the SRB case, and apply better shielding to the tunnel cover seams and other apertures where lightning electromagnetic energy can couple to the interior.

A comparison of the open-circuit voltage and short circuit current calculations with the scaled high current bank measurements indicated discrepancies between the cable model and the test experiment. The calculations of the peak short-circuit current values are an average of 62% greater and the peak open-circuit voltage

values are an average of 44% smaller than the scaled measured values. Possible reasons for the discrepancies are due to the approximations used in defining the impedance of the "jumper" straps across the tunnel cover seams, the impedance of the USBI cable shields, and the diameters of the cables within the systems tunnel. Accurate values for these parameters were unavailable, so best estimates were used. Also, the high current bank results indicated that nonlinear effects occur at high injection current levels (an example is arcing), whereas the systems tunnel models are linear.

4.5 References

1. Cook, Roger B., "Wires User's Manual," AMRC-R-140 (Contract No. DAA639-78-C-0026), Mission Research Corporation, July 1978.

2. Licking, Leonard D., "Capacitance Analysis for Arbitrary Cylindrical Geometries," SL-RR-72-0299, Guidance Components and EM Effects Division, Sandia Laboratories, June 1972.

3. Eriksen, F.J., T.H. Rudolph, R.A. Perala, "Atmospheric Electricity Hazards Analytical Model Development and Application," EMA-81-R-21, April 1981.

4. Rigden, G.J., A.B. Lankford, R. Auguston, P.B. Papazian, "Analysis of the Bonding Straps, the DFI Cables and the Test Configuration for the Lightning Test Program," EMA-88-R-50, August 1988.

5. Perala, R.A., R.B. Cook, J.D. Robb, "Support of Lightning Analysis and Testing on the Solid Rocket Booster (SRB) Vehicle," AMRC-R-122 (Contract No. NASB-31168), Mission Research Corporation, March 1978.

APPENDIX B

FINITE DIFFERENCE TECHNIQUE

APPENDIX B

FINITE DIFFERENCE TECHNIQUE

In this report, extensive use was made of the finite difference technique of solving Maxwell's equations. The following is a description of this numerical method.

Maxwell's equations are given by:

$$\nabla x \vec{E} = -\mu \frac{\partial \vec{H}}{\partial t} \tag{B.1}$$

and

$$\nabla x \vec{H} = \vec{J} + \sigma \vec{E} + \varepsilon \frac{\partial \vec{E}}{\partial t} \tag{B.2}$$

where MKS units and common notation have been used.

In cartesian coordinates, Equations (B.1) and (B.2) can be written in component form yielding six equations:

$$-\mu \left(\frac{\partial H_x}{\partial t}\right) = \left(\frac{\partial E_z}{\partial y}\right) - \left(\frac{\partial E_y}{\partial z}\right) \tag{B.3}$$

$$-\mu \left(\frac{\partial H_y}{\partial t}\right) = \left(\frac{\partial E_x}{\partial z}\right) - \left(\frac{\partial E_z}{\partial x}\right) \tag{B.4}$$

$$-\mu \left(\frac{\partial H_z}{\partial t}\right) = \left(\frac{\partial E_y}{\partial x}\right) - \left(\frac{\partial E_x}{\partial y}\right) \tag{B.5}$$

$$\varepsilon \frac{\partial E_x}{\partial t} + \sigma E_x = \left(\frac{\partial H_z}{\partial y}\right) - \left(\frac{\partial H_y}{\partial z}\right) - j_x \tag{B.6}$$

$$\varepsilon \frac{\partial E_y}{\partial t} + \sigma E_y = \left(\frac{\partial H_x}{\partial z}\right) - \left(\frac{\partial H_z}{\partial x}\right) - j_y \qquad \text{(B.7)}$$

$$\varepsilon \frac{\partial E_z}{\partial t} + \sigma E_z = \left(\frac{\partial H_y}{\partial x}\right) - \left(\frac{\partial H_x}{\partial y}\right) - j_z \qquad \text{(B.8)}$$

The solution proceeds by replacing each derivative by its finite difference approximation. For example, the difference form of Equation (B.3) is:

$$-\mu \left(\frac{H_x(x,y,z,t + 1/2\Delta t) - H_x(x,y,z,t - 1/2\Delta t)}{\Delta t} \right)$$

$$= \frac{E_z(x,y + 1/2\Delta y,z,t) - E_z(x,y - 1/2\Delta y,z,t)}{\Delta y} \qquad \text{(B.9)}$$

$$- \frac{E_y(x,y,z+ 1/2\Delta z,t) - E_y(x,y,z - 1/2\Delta z,t)}{\Delta z}$$

where center-differencing has been used; that is, derivatives at "x", "y", "z" and "t" are approximated by differences centered at these points. This method results in smaller discretization error than that which results from one-sided differences. The differenced forms of Equations (B.4) through (B.8) are arrived at similarly.

The centered differencing procedure yields a grid of three dimensional space as shown in Figure B.1.

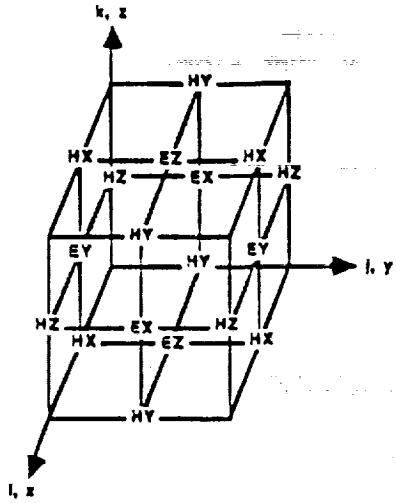

Figure B.1 Three Dimensional Space Grid

To simplify the notation resulting from the finite difference approximations to Equations (B.3) through (B.8), let:

$$H_x^n(i,j,k) = H_x(x(i),y_o(j),z_o(k),t_H(n))$$

$$H_y^n(i,j,k) = H_y(x_o(i),y(j),z_o(k),t_H(n))$$

$$H_z^n(i,j,k) = H_z(x_o(i),y_o(j),z(k),t_H(n)) \qquad \text{(B.10)}$$

$$E_x^n(i,j,k) = E_x(x_o(i),y(j),z(k),t_E(n))$$

$$E_y^n(i,j,k) = E_y(x(i),y_o(j),z(k),t_E(n))$$

$$E_z^n(i,j,k) = E_z(x(i),y(j),z_o(k),t_E(n))$$

where

$$x_o(i) = (i-1)\Delta x\ ,\ y_o(j) = (j-1)\Delta y\ ,\ z_o(k) = (k-1)\Delta z\ ,\ t_H(n) = (n-1)\Delta t$$

$$x(i) = (i-1/2)\Delta x\ ,\ y(j) = (j-1/2)\Delta y\ ,\ z(k) = (k-1/2)\Delta z\ ,\ t_E(n) = (n-1/2)\Delta t$$

Using Equations (B.10), Equations (B.3) through (B.8) can be written as:

$$H_x^{n+1}(i,j+1,k+1) = H_x^{n}(i,j+1,k+1) - \frac{\Delta t}{\mu}\left(\frac{E_z^{n}(i,j+1,k+1) - E_z^{n}(i,j,k+1)}{y(j+1) - y(j)}\right) + \frac{\Delta t}{\mu}\left(\frac{E_y^{n}(i,j+1,k+1) - E_y^{n}(i,j+1,k)}{z(k+1) - z(k)}\right) \quad \begin{matrix} ie\{1,i_{can}] \\ je\{1,i_{can}-1] \\ ke\{1,k_{can}-1] \end{matrix}$$

$$H_y^{n+1}(i+1,j,k+1) = H_y^{n}(i+1,j,k+1) - \frac{\Delta t}{\mu}\left(\frac{E_x^{n}(i+1,j,k+1) - E_x^{n}(i+1,j,k)}{z(k+1) - z(k)}\right) + \frac{\Delta t}{\mu}\left(\frac{E_z^{n}(i+1,j,k+1) - E_z^{n}(i,j,k+1)}{x(i+1) - x(i)}\right) \quad \begin{matrix} ie\{1,i_{can}-1] \\ je\{1,j_{can}] \\ ke\{1,k_{can}-1] \end{matrix}$$

$$H_z^{n+1}(i+1,j+1,k) = H_z^{n}(i+1,j+1,k) - \frac{\Delta t}{\mu}\left(\frac{E_y^{n}(i+1,j+1,k) - E_y^{n}(i,j+1,k)}{x(i+1) - x(i)}\right) + \frac{\Delta t}{\mu}\left(\frac{E_x^{n}(i+1,j+1,k) - E_x^{n}(i+1,j,k)}{y(j+1) - y(j)}\right) \quad \begin{matrix} ie\{1,i_{can}-1] \\ je\{1,i_{can}-1] \\ ke\{1,k_{can}] \end{matrix} \qquad \text{(B.11)}$$

$$B \cdot E_x^{n+1}(i,j,k) = A \cdot E_x^{n}(i,j,k) - j_x(i,j,k) + \left(\frac{H_z^{n+1}(i,j+1,k) - H_z^{n+1}(i,j,k)}{y_o(j+1) - y_o(j)}\right) - \left(\frac{H_y^{n+1}(i,j,k+1) - H_y^{n+1}(i,j,k)}{z_o(k+1) - z_o(k)}\right) \quad \begin{matrix} ie\{2,i_{can}] \\ je\{1,i_{can}] \\ ke\{1,k_{can}] \end{matrix}$$

$$B \cdot E_y^{n+1}(i,j,k) = A \cdot E_y^{n}(i,j,k) - j_y(i,j,k) + \left(\frac{H_x^{n+1}(i,j,k+1) - H_x^{n+1}(i,j,k)}{z_o(k+1) - z_o(k)}\right) - \left(\frac{H_z^{n+1}(i+1,j,k) - H_z^{n+1}(i,j,k)}{x_o(i+1) - x_o(i)}\right) \quad \begin{matrix} ie\{1,i_{can}] \\ je\{2,i_{can}] \\ ke\{1,k_{can}] \end{matrix}$$

$$B \cdot E_z^{n+1}(i,j,k) = A \cdot E_z^{n}(i,j,k) - j_z(i,j,k) + \left(\frac{H_y^{n+1}(i+1,j,k) - H_y^{n+1}(i,j,k)}{x_o(i+1) - x_o(i)}\right) - \left(\frac{H_x^{n+1}(i,j+1,k) - H_x^{n+1}(i,j,k)}{y_o(j+1) - y_o(i)}\right) \quad \begin{matrix} ie\{1,i_{can}] \\ je\{1,i_{can}] \\ ke\{2,k_{can}] \end{matrix}$$

where

$$A = \left(\frac{\varepsilon}{\Delta t} - \frac{\sigma}{2}\right)\ ,\ B = \left(\frac{\varepsilon}{\Delta t} + \frac{\sigma}{2}\right)\ ,\ j_x(i,j,k) = j_x(x_o(i),y(j),z(k),t_H(n+1)),\ j_y(i,j,k) = j_y(x(i),y_o(j),z(k),t_H(n+1)),$$
$$j_z(i,j,k) = j_z(x(i),y(j),z_o(k),t_H(n+1))$$

where i_{can}, j_{can}, k_{can} define the outer boundaries of the problem space.

Equations (B.11) allow the utilization of a nonuniform grid.

The above outlined procedure requires boundary conditions to restrict the problem to a realistic volume of three dimensional space. An absorbing boundary condition is used which simulates the rest of free space. These boundary conditions consist of externally supplied tangential electric or magnetic fields on the outer surface

of the problem space. For the test object lightning study, externally supplied tangential H-fields were used. Therefore the H-fields which must be supplied externally are:

$$
\begin{array}{llll}
H_x(i,j,1) & , \quad H_x(i,j,k_{can}+1) & , \quad \text{all } i \in [1,i_{can}] & , \; j \in [2,j_{can}] \\
H_y(i,j,1) & , \quad H_y(i,j,k_{can}+1) & , \quad \text{all } i \in [2,i_{can}] & , \; j \in [1,j_{can}] \\
H_x(i,1,k) & , \quad H_x(i,j_{can}+1,k) & , \quad \text{all } i \in [1,i_{can}] & , \; k \in [2,k_{can}] \\
H_z(i,1,k) & , \quad H_z(i,j_{can}+1,k) & , \quad \text{all } i \in [2,i_{can}] & , \; k \in [1,k_{can}] \\
H_y(1,i,k) & , \quad H_y(i_{can}+1,j,k) & , \quad \text{all } j \in [1,j_{can}] & , \; k \in [2,k_{can}] \\
H_z(1,j,k) & , \quad H_z(i_{can}+1,j,k) & , \quad \text{all } j \in [2,j_{can}] & , \; k \in [1,k_{can}]
\end{array}
$$

The above procedure requires the selection of Δx, Δy, Δz, and Δt. Such a selection is based on grid sizes that would best fit the object of interest without exceeding computer capabilities.

Reviewing Equations (B.11) reveals a wave propagation velocity in the computation. This computation cannot follow a wave where the physical velocity of propagation exceeds the computational velocity. To obtain stability, the time increment must be made small enough. This condition is satisfied if:

$$
\Delta t < \frac{1}{C\sqrt{\left(\frac{1}{\Delta x}\right)^2 + \left(\frac{1}{\Delta y}\right)^2 + \left(\frac{1}{\Delta z}\right)^2}} \quad , \tag{B.12}
$$

where C is the speed of light. This is known as the Courant criterion.

APPENDIX C

TEST RESULTS TO FLIGHT SCALING ANALYSIS

The objective of this appendix is to present the analysis used to scale the test results discussed in chapter 3 to the flight systems tunnel configuration. The scaling factors used to scale the measured USBI cable open circuit voltages and short circuit currents to the flight threat levels are dependent upon the average surface current density on the systems tunnel, the number of seam apertures in the tunnel, and the length of the systems tunnel. The analysis is based upon the conclusion that the seam apertures in the systems tunnel are the dominant points of entry for lightning electromagnetic energy to couple to the cables within the tunnel. The following documents a comparison between the test article and flight configurations.

	TEST ARTICLE	FLIGHT
Forward Tunnel		
No. of apertures	7	21
Tunnel length (meters)	8.3	26
Apertures per unit-length	0.84	0.81
Aft Tunnel		
No. of apertures	13	16
Tunnel length (meters)	8.3	8.5
Apertures per unit-length	1.56	1.88

The surface current density on the flight configuration of the systems tunnel is determined from the results of a previous report [4] which analyzed the effects of a lightning strike to the flight configuration of the SRB and the systems tunnel. The surface current density on the test article systems tunnel is calculated in Section 4.2 of this report.

The average surface current density (J_{ave}) on the tunnel is calculated by using

$$J_{ave} = \frac{1}{N_g} \sum_{i=1}^{N_g} J_i$$

where N_g is the number of grid cells used to model the systems tunnel, and J_i is the peak value of the surface current density of the i'th grid cell.

The open-circuit voltage (OCVSF) and the short-circuit current (SSCSF) scaling factors are defined as

$$OCVSF = \frac{J_{ave} \times A\ (flight)}{J_{ave} \times A\ (test)}$$

$$SSCSF = \frac{J_{ave} \times N\ (flight)}{J_{ave} \times N\ (test)}$$

where A is the number of seam apertures per-unit-length, and N is the number of seam apertures. The average current densities and scaling factors are tabulated below.

	Test Article J_{ave} (kA/m)	**Flight J_{ave} (kA/m)**	**OSVSF**	**SCCSF**
Forward Tunnel	20.5	21	3.1	1.0
Aft Tunnel	8.4	14	2.0	2.0

The scaled USBI cable open-circuit voltages and short-circuit currents are listed in Tables 3.2.2 and 3.2.4 in Chapter 3.

APPENDIX D

CAPACITANCE AND INDUCTANCE MATRICES

The capacitance and inductance matrices given below electrically describe the mutual coupling between cables within the systems tunnel, and were calculated and applied in the multiconductor cable analysis presented in Section 4.3.2. Each set of matrices represents a 7 cable configuration as illustrated in Figures 4.3.2 and 4.3.3 where the matrix cable numbering in comparison to the cable definitions given in Table 4.3.1 is as follows: For cross-sections 1, 2, and 3 (forward tunnel),

Matrix Cable Number	Table 4.3.1 Cable Number
1	6
2	7
3	8
4	9
5	1, 2, 5
6	4
7	3, 13, 14, 15

For cross-sections 4, 5, and 6 (aft tunnel),

Matrix Cable Number	Table 4.3.1 Cable Number
1	9
2	1, 2, 5
3	4
4	3, 13, 14, 15
5	12
6	11
7	10

0.852E-10	-0.342E-10	-0.391E-10	-0.735E-12	-0.342E-15	-0.119E-12	-0.646E-13
-0.342E-10	0.140E-09	-0.124E-10	-0.168E-10	-0.366E-14	-0.171E-11	-0.740E-12
-0.391E-10	-0.124E-10	0.131E-09	-0.389E-10	-0.854E-16	-0.202E-13	-0.111E-13
-0.735E-12	-0.168E10	-0.389E-10	0.122E-09	-0.108E-16	-0.579E-16	-0.301E-16
-0.342E-15	-0.366E-14	-0.854E-16	-0.108E-16	0.157E-09	-0.335E-10	-0.450E-10
-0.119E-12	-0.171E-11	-0.202E-13	-0.579E-16	-0.335E-10	0.164E-09	-0.490E-10
-0.646E-13	-0.740E-12	-0.111E-13	-0.301E-16	-0.450E-10	-0.490E-10	0.126E-09

CAPACITANCE MATRIX FOR CROSS-SECTION NUMBER 1

0.370E-06	0.111E-06	0.140E-06	0.619E-07	0.111E-08	0.231E-08	0.215E-08
0.111E-06	0.198E-06	0.666E-07	0.491E-07	0.164E-08	0.343E-08	0.315E-08
0.140E-06	0.666E-07	0.245E-06	0.878E-07	0.637E-09	0.132E-08	0.123E-08
0.619E-07	0.491E-07	0.878E-07	0.217E-06	0.435E-09	0.906E-09	0.836E-09
0.111E-08	0.164E-08	0.637E-09	0.435E-09	0.182E-06	0.639E-07	0.897E-07
0.231E-08	0.343E-08	0.132E-08	0.906E-09	0.639E-07	0.176E-06	0.914E-07
0.215E-08	0.315E-08	0.123E-08	0.836E-09	0.897E-07	0.914E-07	0.244E-06

INDUCTANCE MATRIX FOR CROSS-SECTION NUMBER 1

0.852E-10	-0.342E-10	-0.391E-10	-0.735E-12	-0.252E-15	-0.126E-12	-0.510E-13
-0.342E-10	0.140E-09	-0.124E-10	-0.168E-10	-0.273E-14	-0.179E-11	-0.582E-12
-0.391E-10	-0.124E-10	0.131E-09	-0.389E-10	-0.644E-16	-0.214E-13	-0.878E-14
-0.735E-12	-0.168E-10	-0.389E-10	0.122E-09	-0.855E-17	-0.613E-16	-0.245E-16
-0.252E-15	-0.273E-14	-0.644E-16	-0.855E-17	0.139E-09	-0.227E-10	-0.586E-10
-0.126E-12	-0.179E-11	-0.214E-13	-0.613E-16	-0.227E-10	0.156E-09	-0.490E-10
-0.510E-13	-0.582E-12	-0.878E-14	-0.245E-16	-0.586E-10	-0.490E-10	0.140E-09

CAPACITANCE MATRIX FOR CROSS-SECTION NUMBER 2

0.370E-06	0.111E-06	0.140E-06	0.619E-07	0.121E-08	0.237E-08	0.194E-08
0.111E-06	0.198E-06	0.666E-07	0.491E-07	0.178E-08	0.353E-08	0.286E-08
0.140E-06	0.666E-07	0.245E-06	0.878E-07	0.690E-09	0.136E-08	0.111E-08
0.619E-07	0.491E-07	0.878E-07	0.217E-06	0.472E-09	0.931E-09	0.758E-09
0.121E-08	0.178E-08	0.690E-09	0.472E-09	0.220E-06	0.685E-07	0.116E-06
0.237E-08	0.353E-08	0.136E-08	0.931E-09	0.685E-07	0.182E-06	0.925E-07
0.194E-08	0.286E-08	0.111E-08	0.758E-09	0.116E-06	0.925E-07	0.241E-06

INDUCTANCE MATRIX FOR CROSS-SECTION NUMBER 2

0.852E-10	-0.342E-10	-0.391E-10	-0.735E-12	-0.223E-15	-0.126E-12	-0.510E-13
-0.342E-10	0.140E-09	-0.124E-10	-0.168E-10	-0.242E-14	-0.179E-11	-0.583E-12
-0.391E-10	-0.124E-10	0.131E-09	-0.389E-10	-0.573E-16	-0.214E-13	-0.878E-14
-0.735E-12	-0.168E-10	-0.389E-10	0.122E-09	-0.766E-17	-0.613E-16	-0.248E-16
-0.223E-15	-0.242E-14	-0.573E-16	-0.766E-17	0.119E-09	-0.195E-10	-0.487E-10
-0.126E-12	-0.179E-11	-0.214E-13	-0.613E-16	-0.195E-10	0.154E-09	-0.499E-10
-0.510E-13	-0.583E-12	-0.878E-14	-0.248E-16	-0.487E-10	-0.499E-10	0.131E-09

CAPACITANCE MATRIX FOR CROSS-SECTION NUMBER 3

0.370E-06	0.111E-06	0.140E-06	0.619E-07	0.122E-08	0.240E-08	0.201E-08
0.111E-06	0.198E-06	0.666E-07	0.491E-07	0.180E-08	0.358E-08	0.295E-08
0.140E-06	0.666E-07	0.245E-06	0.878E-07	0.697E-09	0.138E-08	0.115E-08
0.619E-07	0.491E-07	0.878E-07	0.217E-06	0.476E-09	0.944E-09	0.783E-09
0.122E-08	0.180E-08	0.697E-09	0.476E-09	0.246E-06	0.691E-07	0.118E-06
0.240E-08	0.358E-08	0.138E-08	0.944E-09	0.691E-07	0.184E-06	0.954E-07
0.201E-08	0.295E-08	0.115E-08	0.783E-09	0.118E-06	0.954E-07	0.249E-06

INDUCTANCE MATRIX FOR CROSS-SECTION NUMBER 3

0.146E-09	-0.243E-16	-0.842E-15	-0.625E-15	-0.158E-15	-0.308E-10	-0.524E-10
-0.243E-16	0.200E-09	-0.560E-10	-0.187E-13	-0.661E-10	-0.450E-13	-0.792E-14
-0.842E-15	-0.560E-10	0.174E-09	-0.158E-11	-0.334E-10	-0.248E-11	-0.320E-12
-0.625E-15	-0.187E-13	-0.158E-11	0.642E-10	-0.152E-12	-0.187E-10	-0.252E-12
-0.158E-15	-0.661E-10	-0.334E-10	-0.152E-12	0.112E-09	-0.346E-12	-0.586E-13
-0.308E-10	-0.450E-13	-0.248E-11	-0.187E-10	-0.346E-12	0.200E-09	-0.538E-10
-0.524E-10	-0.792E-14	-0.320E-12	-0.252E-12	-0.586E-13	-0.538E-10	0.140E-09

CAPACITANCE MATRIX FOR CROSS-SECTION NUMBER 4

0.200E-06	0.935E-09	0.173E-08	0.174E-07	0.132E-08	0.585E-07	0.972E-07
0.935E-09	0.176E-06	0.813E-07	0.295E-08	0.128E-06	0.206E-08	0.139E-08
0.173E-08	0.813E-07	0.174E-06	0.563E-08	0.993E-07	0.382E-08	0.256E-08
0.174E-07	0.295E-08	0.563E-08	0.359E-06	0.408E-08	0.426E-07	0.235E-07
0.132E-08	0.128E-06	0.993E-07	0.408E-08	0.302E-06	0.288E-08	0.197E-08
0.585E-07	0.206E-08	0.382E-08	0.426E-07	0.288E-08	0.145E-06	0.775E-07
0.972E-07	0.139E-08	0.256E-08	0.235E-07	0.197E-08	0.775E-07	0.225E-06

INDUCTANCE MATRIX FOR CROSS-SECTION NUMBER 4

0.146E-09	-0.243E-16	-0.838E-15	-0.697E-15	-0.158E-15	-0.308E-10	-0.524E-10
-0.243E-16	0.200E-09	-0.560E-10	-0.208E-13	-0.661E-10	-0.442E-13	-0.791E-14
-0.838E-15	-0.560E-10	0.174E-09	-0.176E-11	-0.334E-10	-0.241E-11	-0.319E-12
-0.697E-15	-0.208E-13	-0.176E-11	0.729E-10	-0.169E-12	-0.210E-10	-0.281E-12
-0.158E-15	-0.661E-10	-0.334E-10	-0.169E-12	0.112E-09	-0.339E-12	-0.585E-13
-0.308E-10	-0.442E-13	-0.241E-11	-0.210E-10	-0.339E-12	0.201E-09	-0.537E-10
-0.524E-10	-0.791E-14	-0.319E-12	-0.281E-12	-0.585E-13	-0.537E-10	0.140E-09

CAPACITANCE MATRIX FOR CROSS-SECTION NUMBER 5

0.200E-06	0.928E-09	0.171E-08	0.172E-07	0.131E-08	0.583E-07	0.971E-07
0.928E-09	0.176E-06	0.813E-07	0.289E-08	0.128E-06	0.204E-08	0.138E-08
0.171E-08	0.813E-07	0.174E-06	0.553E-08	0.993E-07	0.378E-08	0.254E-08
0.172E-07	0.289E-08	0.553E-08	0.318E-06	0.400E-08	0.420E-07	0.232E-07
0.131E-08	0.128E-06	0.993E-07	0.400E-08	0.302E-06	0.286E-08	0.195E-08
0.583E-07	0.204E-08	0.378E-08	0.420E-07	0.286E-08	0.145E-06	0.773E-07
0.971E-07	0.138E-08	0.254E-08	0.232E-07	0.195E-08	0.773E-07	0.225E-06

INDUCTANCE MATRIX FOR CROSS-SECTION NUMBER 5

0.146E-09	-0.238E-16	-0.801E-15	-0.136E-14	-0.154E-15	-0.308E-10	-0.524E-10
-0.238E-16	0.200E-09	-0.560E-10	-0.388E-13	-0.661E-10	-0.372E-13	-0.772E-14
-0.801E-15	-0.560E-10	0.174E-09	-0.329E-11	-0.333E-10	-0.187E-11	-0.303E-12
-0.136E-14	-0.388E-13	-0.329E-11	0.213E-09	-0.313E-12	-0.453E-10	-0.521E-12
-0.154E-15	-0.661E-10	-0.333E-10	-0.313E-12	0.112E-09	-0.283E-12	-0.569E-13
-0.308E-10	-0.372E-13	-0.187E-11	-0.453E-10	-0.283E-12	0.218E-09	-0.536E-10
-0.524E-10	-0.772E-14	-0.303E-12	-0.521E-12	-0.569E-13	-0.536E-10	0.140E-09

CAPACITANCE MATRIX FOR CROSS-SECTION NUMBER 6

0.198E-06	0.777E-09	0.143E-08	0.118E-07	0.110E-08	0.539E-07	0.947E-07
0.777E-09	0.176E-06	0.812E-07	0.184E-08	0.127E-06	0.168E-08	0.117E-08
0.143E-08	0.812E-07	0.173E-06	0.351E-08	0.992E-07	0.310E-08	0.215E-08
0.118E-07	0.184E-08	0.351E-08	0.111E-06	0.252E-08	0.286E-07	0.157E-07
0.110E-08	0.127E-06	0.992E-07	0.252E-08	0.302E-06	0.235E-08	0.166E-08
0.539E-07	0.168E-08	0.310E-08	0.286E-07	0.235E-08	0.134E-06	0.713E-07
0.947E-07	0.117E-08	0.215E-08	0.157E-07	0.166E-08	0.713E-07	0.221E-06

INDUCTANCE MATRIX FOR CROSS-SECTION NUMBER 6

DISTRIBUTION

Recipient	No. of Copies	Mail Stop
M. Cook	4	L71
N. Black	1	L71
R. Lavery	1	L71
B. Jurewicz	1	L70
J. Griffin	1	L62
B. Whidden	1	L62
T. Olsen	1	L71
R. Rasmussen	1	E06
J. Godfrey	1	E06
G. Stephens	1	E12
B. Crosbie	1	E15
J. Oostyen	1	L72
D. Smith	1	L72
R. Hyer	1	L62
J. Seiler	1	L72
M. Williams	1	L62
P. St. Jean	1	L62
J. Miller	1	L62
K. Sanofsky	1	851
R. Larsen	1	851
F. Duersch	1	851
M. Fisher	1	K68
R. Papasian	45	E05
Print Crib	5	K23B1
Data Management	5	L724